UNCLASSIFIED

AD 430606

DEFENSE DOCUMENTATION CENTER

FOR

SCIENTIFIC AND TECHNICAL INFORMATION

CAMERON STATION, ALEXANDRIA, VIRGINIA

UNCLASSIFIED

NOTICE: When government or other drawings, specifications or other data are used for any purpose other than in connection with a definitely related government procurement operation, the U. S. Government thereby incurs no responsibility, nor any obligation whatsoever; and the fact that the Government may have formulated, furnished, or in any way supplied the said drawings, specifications, or other data is not to be regarded by implication or otherwise as in any manner licensing the holder or any other person or corporation, or conveying any rights or permission to manufacture, use or sell any patented invention that may in any way be related thereto.

64-9

TECHNICAL INFORMATION SERIES

CATALOGED BY DDC
AS AD No. 430606

R64SD13

# THEORETICAL HYPERVELOCITY IMPACT CALCULATIONS USING THE PICWICK CODE

DDC
MAR 9 1964
TISIA A

T.D. RINEY

SPACE SCIENCES LABORATORY
GENERAL ELECTRIC
MISSILE AND SPACE DIVISION

430606

# SPACE SCIENCES LABORATORY

MECHANICS SECTION

THEORETICAL HYPERVELOCITY IMPACT CALCULATIONS*

By

T. D. Riney

*Work supported by the Air Proving Ground Center
Eglin Air Force Base, under Contract No. AF 04(635)-3781

R64SD13
February 1964

MISSILE AND SPACE DIVISION

GENERAL ELECTRIC

ACKNOWLEDGEMENT

This first interim report was prepared by the Space Structures Operation of the Space Sciences Laboratory of the General Electric Missile and Space Division, under Air Force Contract AF 08(635)-3781 "Theoretical Terminal Ballistic Study; Energy Dissipation During Impact". The work was administered under the direction of the Terminal Effects Division, Air Proving Ground Center, Eglin Air Force Base with Mr. A.G. Bilek and Lt. M.S. Harris as Project Engineers.

The author wishes to acknowledge the contributions of Mr. A.B. Sinopoli to the continual improvement of the computer code. He is indebted to Mr. O.A. Winter for assistance in reducing the numerical data. He is grateful to Dr. J.F. Heyda for the values quoted in Table IV and for helpful technical discussions. He wishes to express his appreciation to Mr. Carson Sasser of the Mathematical Services Laboratory, Eglin AFB, for his interest and efficiency in running the computer program. Finally, the author wishes to thank Dr. F.W. Wendt for his encouragement and support throughout the investigation.

## SUMMARY

The principle uncertainty in the visco-plastic model of hypervelocity impact is the lack of data on strain-rate effects under the severe conditions of interest. Estimates of $\mu$ for iron and aluminum are first determined that are compatible both with observed strain-rate effects in plastic waves and the very abrupt shock profiles known to exist at pressures greater than about .2 megabar.

In the second part of the report detailed calculations are presented describing the cratering process for a cylindrical projectile impacting a thick target of like metal. It is shown that momentum scaling cannot be justified; energy scaling for geometrically similar impact situations is accurately predicted upon taking into account the different rates of shock propagation during the early stages of the cratering process. The depth of penetration is therefore related to impact velocity $v_o$ according to $P_c = K_e v_o^{2/3}$ for $v_o \geqq v_o^*$. Strength effects of the target do not vanish with increasing impact velocity.

In the third part of the report the cratering and the penetration process for thin plates is studied. PICWICK calculations are presented and the results discussed in terms of the interactions of shock waves, rarefaction waves, and configuration geometry.

TABLE OF CONTENTS


| | | Page |
|---|---|---|
| INTRODUCTION | | 1 |
| PART I: | STRAIN-RATE EFFECTS | 3 |
| | One Dimensional Flow | 3 |
| | Rankine-Hugoniot Data | 5 |
| | Shock Transition Equations | 8 |
| | Calculated Strain—Rate Effects | 11 |
| PART II: | IMPACT INTO A THICK TARGET | 13 |
| | Flow Fields for Thick Targets | 13 |
| | Energy vs. Momentum Scaling | 14 |
| | Threshold of Energy Scaling | 17 |
| PART III: | IMPACT INTO PLATES | 19 |
| | Flow Fields for Plate Targets | 19 |
| | Release of Pressure Pulse | 20 |
| CONCLUSIONS | | 22 |
| BIBLIOGRAPHY | | 24 |
| APPENDIX | | 26 |
| TABLES | | 27 |
| FIGURES | | 32 |

## LIST OF ILLUSTRATIONS


| Figure | | Page |
|---|---|---|
| 1 | Illustration of the cratering and penetration of a structural member by a hypervelocity projectile: (a) axial section of configuration at impact, (b) generation of pressure pulse between shock fronts in projectile and target, (c) material ejected from target surface and the pressure pulse propagates into the target, (d) spallation at opposite free surface resulting from reflection of pressure pulse ..... | 30 |
| 2 | Illustration of the features of the front of a steady one-dimensional shock wave in which the strain-rate effect is included: (a) the shock profile depicted in laboratory coordinates, (b) definition of the thickness of the shock front, $\Delta P$ ..... | 31 |
| 3 | Calculated shock profiles in mild steel for a final compression ratio $X_f = 0.9$ when $\mu$ is assumed to follow (a) linear law, (b) power law, (c) logarithmic law ..... | 32 |
| 4 | The distribution of the mass point representation of the axisymmetric projectile-target configuration at the instant of impact..... | 33 |
| 5a | The mass point plot .209 $\mu$sec after impact of an aluminum projectile into a thick aluminum target at .76 cm/$\mu$sec ..... | 34 |
| 5b | The mass point plot 1.080 $\mu$sec after impact of an aluminum projectile into a thick aluminum target at .76 cm/$\mu$sec ..... | 35 |
| 6a | The mass point plot .249 $\mu$sec after impact of an aluminum projectile into a thick aluminum target at 2.0 cm/$\mu$sec ..... | 36 |
| 6b | The mass point plot .550 $\mu$sec after impact of an aluminum projectile into a thick aluminum target at 2.0 cm/$\mu$sec ..... | 37 |
| 7a | The mass point plot at t = .249 $\mu$sec after impact of a cylindrical lead projectile into a lead target at $v_0$ = 2.0 cm/$\mu$sec .. | 38 |
| 7b | The mass point plot at t = .525 $\mu$sec after impact of a cylindrical projectile into a thick lead target at $v_0$ = 2.0 cm/$\mu$sec.. | 39 |
| 7c | The mass point plot at t = 1.297 $\mu$sec after impact of a cylindrical lead projectile into a thick lead target at $v_0$ = cm/$\mu$sec ..... | 40 |

LIST OF ILLUSTRATIONS (Continued)


| Figure | | Page |
|---|---|---|
| 7d | The mass point plot at t = 3.086 μsec after impact of a cylindrical lead projectile into a thick lead target at $v_0$ = 2.0 cm/μsec | 41 |
| 7e | The mass point plot at t = 4.975 μsec after impact of a cylindrical lead projectile into a thick lead target at $v_0$ = 2.0 cm/μsec | 42 |
| 8 | Total forward momentum in the target as a function of the time since impact of an aluminum projectile and a thick aluminum target | 43 |
| 9 | Total positive radial momentum in a thick aluminum target at indicated time since impact by an aluminum projectile | 44 |
| 10 | Total forward momentum in a thick target as a function of the time since impact of a lead projectile and target | 45 |
| 11 | Total positive radial momentum in a thick target at indicated time since lead-lead impact | 46 |
| 12 | The position of the peak axial pressure as a function of time for aluminum-aluminum impact | 47 |
| 13 | The position of the peak axial pressure as a function of time for lead-lead impact | 48 |
| 14 | Peak axial pressure in aluminum shown as a function of distance below original surface of a thick target | 49 |
| 15 | Peak axial pressure in lead shown or function of distance below the original surface of a thick target | 50 |
| 16a | Projectile-target material distribution .225 μsec after impact of an aluminum projectile into an aluminum plate at .76 cm/μsec | 51 |
| 16b | Projectile-target material distribution .423 μsec after impact of an aluminum projectile into an aluminum plate at .76 cm/μsec | 52 |
| 16c | Projectile-target material distribution .550 μsec after impact of an aluminum projectile into an aluminum plate at .76 cm/μsec | 53 |

LIST OF ILLUSTRATIONS (Continued)


| Figure | | Page |
|---|---|---|
| 16d | Projectile-target material distribution .676 μsec after impact of an aluminum projectile into an aluminum plate at .76 cm/μsec | 54 |
| 17a | Projectile-target material distribution at .247 μsec after impact of an aluminum projectile into an aluminum plate at 2.0 cm/μsec | 55 |
| 17b | Projectile-target material distribution at .410 μsec after impact of an aluminum projectile into an aluminum plate at 2.0 cm/μsec | 56 |
| 18a | Projectile-target material distribution .255 μsec after impact of an iron projectile into an iron plate at .76 cm/μsec | 57 |
| 18b | Projectile-target material distribution .423 μsec after impact of an iron projectile into an iron plate at .76 cm/μsec | 58 |
| 18c | Projectile-target material distribution .549 μsec after impact of an iron projectile into an iron plate at .76 cm/μsec | 59 |
| 18d | Projectile-target material distribution .676 μsec after impact of an iron projectile into an iron plate at .76 cm/μsec | 60 |
| 19a | Pressure and velocity fields at .136 μsec after impact of an aluminum projectile into an aluminum plate at .76 cm/μsec | 61 |
| 19b | Pressure and velocity fields at .203 μsec after impact of an aluminum projectile into an aluminum plate at .76 cm/μsec | 62 |
| 19c | Pressure and velocity fields at .421 μsec after impact of an aluminum projectile into an aluminum plate at .76 cm/μsec | 63 |
| 19d | Pressure and velocity fields at .539 μsec after impact of an aluminum projectile into an aluminum plate at .76 cm/μsec | 64 |

LIST OF ILLUSTRATIONS (Continued)


| Figure | | Page |
|---|---|---|
| 19e | Pressure and velocity fields at .674 μsec after impact of an aluminum projectile into an aluminum plate at .76 cm/μsec ... | 65 |
| 20a | Pressure and velocity fields at .136 μsec after impact of an iron projectile into an iron plate at .76 cm/μsec ..... | 66 |
| 20b | Pressure and velocity fields at .203 μsec after impact of an iron projectile into an iron plate at .76 cm/μsec ..... | 67 |
| 20c | Pressure and velocity fields at .421 μsec after impact of an iron projectile into an iron plate at .76 cm/μsec ..... | 68 |
| 20d | Pressure and velocity fields at .539 μsec after impact of an iron projectile into an iron plate at .76 cm/μsec ..... | 69 |
| 20e | Pressure and velocity fields at .674 μsec after impact of an iron projectile into an iron plate at .76 cm/μsec ..... | 70 |
| 21 | Comparison of flow field characteristics for aluminum-aluminum impact in thick targets and in plate targets at .76 cm/μsec: (a) Energy partition, (b) Total forward axial momentum, and (c) Total outward radial momentum ..... | 71 |
| 22 | Comparison of flow field characteristics for aluminum-aluminum impact in thick targets and in plate targets at 2.0 cm/μsec: (a) Energy partition, (b) Total forward axial momentum, and (c) Total outward radial momentum ..... | 72 |
| 23 | Comparison of flow field characteristics for iron-iron impact into thick target and in plate targets at .76 cm/μsec: (a) Energy partition, (b) Total forward axial momentum, and (c) Total outward radial momentum ..... | 73 |

## LIST OF SYMBOLS

| | |
|---|---|
| $\tau_{ij}$ | stress tensor |
| $\delta_{ij}$ | unity when i = j, zero otherwise |
| $D_{ij}$ | strain-rate tensor |
| $D^2$ | second invariant of strain-rate deviator tensor |
| $\tau^2$ | second invariant of stress deviator tensor |
| $\mu$ | strain-rate coefficient |
| $S_o$ | yield value of shear stress |
| $\eta_o$ | viscosity factor in strain-rate coefficient |
| $\rho$ | density of medium |
| $\rho_o$ | density of undisturbed medium |
| I | specific internal energy of medium |
| (r, $\theta$, z) | cylindrical coordinates |
| (u, 0, v) | velocity components in cylindrical coordinates |
| w | longitudinal velocity in one-dimensional case |
| $\tau_{zz}$ | longitudinal stress in one-dimensional case |
| q | longitudinal velocity in moving coordinates |
| $U_f$ | velocity of the shock front in laboratory coordinates |
| X | compression ratio across a shock ($= \rho_o/\rho$) |
| U | velocity of the shock front for final compression X |
| $v_o$ | impact velocity |
| $v_o'$ | impact velocity with geometry scaled to compare with $v_o$ |
| $v_o^*$ | threshold value for energy scaling |
| L | radius of cylindrical projectile |
| $\ell$ | length of cylindrical projectile |
| h | thickness of plate target |
| $P_c$ | penetration depth of crater |
| $Z_+$ | total forward axial momentum |
| $R_+$ | total outward radial momentum |
| $\Delta t$ | time lag between cratering processes |

## INTRODUCTION

Previous reports have described the visco-plastic model that has evolved to describe the hypervelocity impact cratering and penetration process [1, 2]*. The model neglects elastic and strain hardening effects and assumes that the stress tensor $\tau_{ij}$, and the strain-rate tensor, $D_{ij}$, are related by a constitutive relation of the form

$$\tau_{ij} = -p\delta_{ij} + \mu \left(D_{ij} - \frac{2}{3} \operatorname{div} \vec{u}\ \delta_{ij}\right), \tag{1}$$

where p is the thermodynamic pressure, $\mu$ the flow resistance coefficient, and $\vec{u}$ is the velocity vector. Given the required relations for p and $\mu$, (1) may be incorporated into the partial differential equations expressing conservation of mass, momentum, and energy to obtain the system of equations governing the model. (See Appendix).

A computer code (PICWICK) for solving the complex system of equations has been developed and has been described in detail elsewhere [3, 4]. The program is capable of using various choices for the equation of state $p = g(\rho, I)$, and the flow-resistance coefficients, $\mu$.

The principle uncertainty in the visco-plastic model is the lack of data on strain-rate effects under the extreme conditions operative during hypervelocity impact. It is necessary to extrapolate data obtained under much less severe conditions to estimate $\mu$. Part I of this report describes the effect that these extrapolated estimates for $\mu$ has on the structure of one-dimensional stress pulses. Estimates for $\mu$ for iron and aluminum are presented which are compatible both with observed strain-rate effects in plastic waves and the very abrupt shock profiles known to exist at pressures greater than about 0.2 mb**. These choices of $\mu$ have been incorporated into PICWICK and some calculations made for axisymmetric impact of a right circular cylinder into a thick target of like material. It is found that flow field is essentially undisturbed by the inclusion of $\mu > 0$ in the early stages of the cratering process for which calculations with the full visco-plastic model have been completed.

Simultaneous with the investigations of the strain-rate effects, the PICWICK code was also used for the special case $\mu = 0$ in order to resolve the outstanding controversy of the hypervelocity impact field today. Both experimental and theoretical investigators are divided as to the manner in which the depth of penetration

---

* Numbers in square brackets refer to the references listed in the Bibliography.

** The gram-centimeter-microsecond system of units is used throughout this report. The unit of pressure becomes the megabar (mb).

of a projectile varies with impact velocity [5]. In Part II the results of PICWICK calculations for the impact of a cylindrical projectile into a thick target of like material are presented for lead and aluminum. The calculations are for impact velocities of $v_0 = .76$ and $2.0$ cm/$\mu$sec and are carried to the point that strain-rate and strength effects become important (tenths of megabars). It is found that momentum scaling cannot be justified. On the contrary, it is shown that energy scaling is accurately predicted if account is taken of the different time origins when comparing geometrically similar impact situations of equal kinetic energy.

In Part III the cratering and penetration process for thin plate targets is studied. PICWICK calculations are presented for iron and aluminum projectiles striking targets of like material $v_0 = .76$ and $2.0$ cm/$\mu$sec. The resulting flow field characteristics are discussed in terms of the interaction of the pressure pulse with the free surfaces of the projectile-target system and with the rarefaction waves originating at these free surfaces. The total forward momentum of the projectile-target debris after penetration is greater than the original projectile momentum.

## PART I: STRAIN-RATE EFFECTS

In order that (1) provides a constitutive relation for the entire penetration process both p and $\mu$ must be specified. Analytical expressions for the thermodynamic pressure as a function of the density, $\rho$, and specific internal energy, I,

$$p = g(\rho, I), \tag{2}$$

have been constructed. These functions are available for most metals and cover the range of interest in blast-loading and hypervelocity impact applications (if $p > o$).

The bulk of the studies with attention to strain-rate effects, however, have been made in which longitudinal plastic stress waves of relatively low amplitude are propagated along bars. The maximum strain-rates obtained are of order $10^{-3}$ to $10^{-2}$ $1/\mu$sec and the resulting data have been fitted into a polytropic framework. Several empirical relations between stress and strain-rate have been proposed which have proved adequate under conditions similar to those in which the data were generated. These rate-dependent, rigid-plastic relations may, in the absence of more realistic information, reasonably be applied in the later stages of flow in the applications of interest here.

This part of the report is concerned with the effect that the inclusion of these estimates for $\mu$ may have at various stages of the flow process. The important phases of the cratering and penetration process are illustrated in Figure 1.

### ONE DIMENSIONAL FLOW

In a recent paper [2] some of the available experimental data were brought together within a framework general enough to permit the extrapolation of these one-dimensional empirical formulas in a natural manner to the tri-axial case. Three of the expressions considered are as follows:

(Linear Law)
$$\mu = \frac{S_o}{|D|}\left[1 + \frac{\eta_o}{S_o}|D|\right] \tag{3a}$$

(Power Law)
$$\mu = \frac{S_o}{|D|}\left[1 + \left\{\frac{\eta_o}{S_o}|D|\right\}^{1/\delta}\right] \tag{3b}$$

$$\text{(Logarithmic Law)} \quad \mu = \frac{S_o}{|D|}\left[1 + \ln\left\{1 + \frac{\eta_o}{S_o}|D|\right\}\right], \tag{3c}$$

provided $|\tau| \geqq S_o$. $\mu = \infty$ in each case when $|\tau| < S_o$. Here, $D^2$ and $\tau^2$ are the second invariants of, respectively, the strain-rate deviator tensor and the stress deviator tensor. In (A-5) of the Appendix the expressions for $D^2$ and $\tau^2$ in terms of the velocity components are listed for the axially symmetric case. $S_o$, $\eta_o$, and $\delta$ are material constants.

In the case of a plane shock propagating in the z direction, the relations (A-5) are simplified by equating to zero u and all derivatives with respect to u. In this part of the report in which only plane waves are considered the z component of velocity is denoted by w rather than v. Then, $D^2 = 4/3\,(\partial w/\partial z)^2$ and the viscosity coefficients in (3) reduce to

$$\mu = \frac{S_o}{\sqrt{\frac{4}{3}}\left|\frac{\partial w}{\partial z}\right|}\left[1 + \frac{\eta_o}{S_o}\sqrt{\frac{4}{3}}\left|\frac{\partial w}{\partial z}\right|\right] \tag{4a}$$

$$\mu = \frac{S_o}{\sqrt{\frac{4}{3}}\left|\frac{\partial w}{\partial z}\right|}\left[1 + \left\{\frac{\eta_o}{S_o}\sqrt{\frac{4}{3}}\left|\frac{\partial w}{\partial z}\right|\right\}^{1/\delta}\right] \tag{4b}$$

$$\mu = \frac{S_o}{\sqrt{\frac{4}{3}}\left|\frac{\partial w}{\partial z}\right|}\left[1 + \ln\left\{1 + \frac{\eta_o}{S_o}\sqrt{\frac{4}{3}}\left|\frac{\partial w}{\partial z}\right|\right\}\right]. \tag{4c}$$

Approximate values of the material parameters, $S_o$, $\eta_o$, and $\delta$ for the case of mild steel have been estimated by Perzyna [6] and are listed in Table I. Symonds and Ting [7] have suggested ranges of values of $S_o$, $\eta_o$, and $\delta$ for the power law for both mild steel and aluminum alloys. Their estimates are listed in Table II.

Consider the plane shock wave propagating in the positive direction through material of infinite extent, Figure 2a. Let the velocity of the steady shock profile in laboratory coordinates be denoted by $U_f$, and let w be the velocity of the compressed material at any point in the profile. Then the longitudinal normal stress at a point on the profile is denoted by $\tau_{zz}$ (< 0) and the transverse normal stresses are $\tau_{rr} = \tau_{\theta\theta}$:

$$\tau_{rr} = \tau_{\theta\theta} = -p + \frac{S_o}{\sqrt{3}} \left[ 1 + \sqrt{\frac{4}{3}} \frac{\eta_o}{S_o} \left| \frac{\partial w}{\partial z} \right| \right]$$

$$\tau_{zz} = -p - \sqrt{\frac{4}{3}}\, S_o \left[ 1 + \sqrt{\frac{4}{3}} \frac{\eta_o}{S_o} \left| \frac{\partial w}{\partial z} \right| \right] \tag{5a}$$

$$\tau_{rr} = \tau_{\theta\theta} = -p + \frac{S_o}{\sqrt{3}} \left[ 1 + \left\{ \sqrt{\frac{4}{3}} \frac{\eta_o}{S_o} \left| \frac{\partial w}{\partial z} \right| \right\}^{1/\delta} \right]$$

$$\tau_{zz} = -p - \sqrt{\frac{4}{3}}\, S_o \left[ 1 + \left\{ \sqrt{\frac{4}{3}} \frac{\eta_o}{S_o} \left| \frac{\partial w}{\partial z} \right| \right\}^{1/\delta} \right] \tag{5b}$$

$$\tau_{rr} = \tau_{\theta\theta} = -p + \frac{S_o}{\sqrt{3}} \left[ 1 + \ln \left\{ 1 + \sqrt{\frac{4}{3}} \frac{\eta_o}{S_o} \left| \frac{\partial w}{\partial z} \right| \right\} \right]$$

$$\tau_{zz} = -p - \sqrt{\frac{4}{3}}\, S_o \left[ 1 + \ln \left\{ 1 + \sqrt{\frac{4}{3}} \frac{\eta_o}{S_o} \left| \frac{\partial w}{\partial z} \right| \right\} \right] \tag{5c}$$

## RANKINE-HUGONIOT DATA

In a coordinate system fixed in the moving profile the point A, in the undisturbed material ahead of the shock is fixed relative to any given point, B, in the shock transition region (see Figure 2a). The states of the material at points A and B may, therefore, be related by applying the three conservation conditions:

(mass) $$(U_f - w)\rho = U_f \rho_o \tag{6}$$

(momentum) $$\rho_o U_f^2 - \rho_o (U_f - w)^2 = -\tau_{zz} \tag{7}$$

$$\text{(energy)} \quad \frac{1}{2}\rho_o U_f^3 = \frac{1}{2}\rho(U_f - w)^3 + \rho I (U_f - w) - \tau_{zz}(U_f - w). \tag{8}$$

Here the specific internal energy, I, is taken to be zero ahead of the shock.

From (6) and (7) one can deduce that

$$-\tau_{zz} = \rho_o w U_f \tag{9}$$

$$1 - X = w/U_f \qquad (X \equiv \rho_o/\rho) \tag{10}$$

$$\rho_o U_f^2 = -\tau_{zz}/(1-X) \tag{11}$$

and then combine with (8) to write

$$\rho_o I = -\frac{1}{2}\tau_{zz}(1-X) \tag{12}$$

$$I = \frac{1}{2} U_f^2 (1-X)^2. \tag{13}$$

Equations (9), (10), and (12) are the familiar Rankine-Hugonoit relations when applied to the particular case where the point B is taken at the crest of the shock, so that w, I, $\tau_{zz}$ and $\rho$ then refer to peak values.

The Rankine-Hugonoit relations are basic to the experimental studies of one dimensional stress pulses induced by metal-metal impact of two plates, the one propelled by a high explosive [8] . In these experiments the peak values of particle velocity w, and the shock propagation speed are measured. The corresponding peak values of longitudinal stress, $\tau_{zz}$, density ratio, X, and specific internal energy I are then calculated from the three equations. This experimentally determined Hugonoit equation of state data is used to derive information concerning the thermodynamic behavior of the material under adiabatic conditions:

$$-\tau_{zz} = f(\rho, I). \tag{14}$$

At the peak of the stress profile $\partial w/\partial z = 0$ and hence, by (5),

$$p + \sqrt{\frac{4}{3}}\ S_o = f(\rho, I). \tag{15}$$

Usually the metal is treated as an inviscid compressible material and the term $\sqrt{4/3}\ S_o$ does not appear: $g(\rho, I) = f(\rho, I) - \sqrt{4/3}\ S_o$.

A function $f(\rho, I)$, defined by (15), that has been fitted to the experimental data is of the form [9].

$$f(\rho, I) = \frac{1}{\phi + \phi_o}\left[\zeta(a_1 + a_2\zeta) + \phi\left\{b_o + \zeta(b_1 + b_2\zeta) + \phi(c_o + c_1\zeta)\right\}\right], \tag{16}$$

where

$$\zeta = \frac{\rho}{\rho_o} - 1 \qquad \phi = \rho_o I.$$

The specific internal energy in the undisturbed material is taken to be zero. Values for the material parameters $a_1$, $a_2$, $b_o$, $b_1$, $b_2$, $c_o$, $c_1$, $\phi_o$ are listed in Table III for aluminum, iron, and lead.

In the following it will be convenient to have a relationship between the velocity of propagation of a wave U and its peak density ratio X. To recover this from the equation of state substitute (11) and (13) into (16) to obtain

$$\rho_o U^2 (1 - X) = f(\rho, I)\Big|_{\phi = \frac{1}{2}\rho_o U^2 (1 - X)^2}$$

When (16) is substituted and the resulting expression is solved for U one obtains

$$U = \sqrt{\frac{-B - \sqrt{B^2 - 4AC}}{2A}}, \tag{17}$$

where

$$A = \frac{1}{4}\rho_o^{\,2}(1-X)^2\left[c_1 X(1-X)^2 + c_o X^2(1-X) - 2X^2\right]$$

$$B = \frac{1}{2}\rho_o\left[b_2(1-X)^3 + b_1 X(1-X)^2 + b_o X^2(1-X) - 2\phi_o X^2\right]$$

$$C = a_1 X + a_2(1-X)\cdot$$

For X = 1 relation (17) is indeterminate and must be replaced by

$$U_o = \sqrt{\frac{a_1}{\phi_o\,\rho_o}}\,. \tag{18}$$

## SHOCK TRANSITION EQUATIONS

In this section the method of Band [10] is extended to obtain the shape of the profile in the shock transition region II. It is convenient to consider a coordinate system moving with the velocity of the permanent profile. The particle velocity in this system is denoted by

$$q = U_f - w\cdot \tag{19}$$

The conservation equations for mass and for momentum for the one-dimensional case are (from the Appendix)

$$\frac{\partial\rho}{\partial t} + q\frac{\partial\rho}{\partial z} + \rho\frac{\partial q}{\partial z} = 0 \tag{20}$$

$$\frac{\partial}{\partial z}\tau_{zz} = \rho\frac{\partial q}{\partial t} + \rho q\frac{\partial q}{\partial z}\,. \tag{21}$$

Since the profile is invariant in this coordinate system the partial derivatives with respect to time vanish. Upon multiplying (20) by q and adding to (21) one obtains

$$\frac{\partial}{\partial z}\tau_{zz} = \frac{\partial}{\partial z}(\rho q^2)\cdot \tag{22}$$

Substitute (19) into (6) to obtain

$$q = X U_f \quad . \tag{23}$$

Equation (22) becomes

$$\frac{\partial}{\partial z}\left[-\tau_{zz} + \rho_o X U_f^2\right] = 0 \quad .$$

Integration and use of the boundary condition

$$\tau_{zz}\Big|_{X=1} = -\sqrt{3}\, S_o$$

yields

$$\tau_{zz} + \sqrt{3}\, S_o + \rho_o U_f^2 (1 - X) = 0 \quad . \tag{24}$$

Substitution of the three relations (5), with q replacing w, into (24) and solving for $\partial q/\partial z$ yields the following corresponding results:

$$\frac{\partial q}{\partial z} = -\frac{S_o}{\sqrt{\frac{4}{3}}\,\eta_o}\left[\frac{\rho_o U_f^2 (1 - X) + \sqrt{3}\, S_o - (p + \sqrt{\frac{4}{3}}\, S_o)}{\sqrt{\frac{4}{3}}\, S_o}\right] \tag{25a}$$

$$\frac{\partial q}{\partial z} = -\frac{S_o}{\sqrt{\frac{4}{3}}\,\eta_o}\left[\frac{\rho_o U_f^2 (1 - X) + \sqrt{3}\, S_o - (p + \sqrt{\frac{4}{3}}\, S_o)}{\sqrt{\frac{4}{3}}\, S_o}\right]^{\delta} \tag{25b}$$

$$\frac{\partial q}{\partial z} = -\frac{S_o}{\sqrt{\frac{4}{3}}\,\eta_o}\left\{\exp\left[\frac{\rho_o U_f^2 (1 - X) + \sqrt{3}\, S_o - (p + \sqrt{\frac{4}{3}}\, S_o)}{\sqrt{\frac{4}{3}}\, S_o}\right] - 1\right\} \tag{25c}$$

At the crest of the wave, located in Figure 2a by the interface between regions II and III, $\partial w/\partial z = 0$ and from (5) and (24) it follows that

$$-\tau_{zz}\Big|_{X_f} = p_f + \sqrt{\frac{4}{3}}\, S_o = \sqrt{3}\, S_o + \rho_o U_f^2 (1 - X_f). \tag{26}$$

Similarly, at the crest of a wave in which the density ratio from foot to crest is X and which propagates at velocity U,

$$-\tau_{zz}\Big|_{X} = p + \sqrt{\frac{4}{3}}\, S_o = \sqrt{3}\, S_o + \rho_o U^2 (1 - X). \tag{27}$$

Substitution of (26) and (27) into (25) yields

$$\frac{\partial q}{\partial z} = -\frac{S_o}{\sqrt{\frac{4}{3}}\,\eta_o}\left[\frac{\rho_o (U_f^2 - U^2)(1 - X)}{\sqrt{\frac{4}{3}}\, S_o}\right] \tag{28a}$$

$$\frac{\partial q}{\partial z} = -\frac{S_o}{\sqrt{\frac{4}{3}}\,\eta_o}\left[\frac{\rho_o (U_f^2 - U^2)(1 - X)}{\sqrt{\frac{4}{3}}\, S_o}\right]^{\delta} \tag{28b}$$

$$\frac{\partial q}{\partial z} = -\frac{S_o}{\sqrt{\frac{4}{3}}\,\eta_o}\left\{\exp\left[\frac{\rho_o (U_f^2 - U^2)(1 - X)}{\sqrt{\frac{4}{3}}\, S_o}\right] - 1\right\} \tag{28c}$$

where U and X are related according to (17).

A simple numerical scheme has been used to calculate the field variables in the shock transition region, II. X is treated as the independent variable, the range being broken into equal J equal intervals $\Delta X = (1 - X_f)/J$, $X_j = 1 - j\Delta X$ ($j = 0, 1, \ldots, J$). From (17), (11), (13), (27)

$$X_f = X_J \quad X_{J-1} \quad \ldots\ldots \quad X_1 \quad X_o = 1$$

and (28) the corresponding values of $U_j$, $(\tau_{zz})_j$, $I_j$, $p_j$, $(\partial q/\partial z)_j$ may be computed in that order.

From (23) it follows that $\partial q/\partial z = U_f\, \partial X/\partial z$, whence ($j = 1, \ldots, J$):

$$z_j \doteq z_{j-1} - \frac{2\, U_J\, \Delta X}{(\partial q/\partial z)_{j-1} + (\partial q/\partial z)_j} \tag{29}$$

By choosing J large enough (29) provides the spatial distribution of the shock variables sufficiently accurate. The calculations are started at $z_0 = 0$ and $(\partial q/\partial z)_0 \doteq 0$.

The thickness of the shock profile, $\Delta P$, is defined by the sketch in Figure 2b. It is easy to see that

$$\frac{1 - X_J}{\Delta P} = \left(\frac{\partial q}{\partial z}\right)_{i.p.} = \frac{1}{U_J}\left(\frac{\partial w}{\partial z}\right)_{i.p.},$$

where the subscript i.p. denotes that derivative is evaluated at the inflection point of the shock profile. Hence

$$\Delta P = U_J\, \frac{1 - X_J}{(\partial w/\partial z)_{i.p.}} \tag{30}$$

## CALCULATED STRAIN-RATE EFFECTS

In Figure 3, the calculated stress profiles are depicted for mild steel in the case that the final compression ratio is $X_f = 0.9$. The results are shown for three choices of the parameters for each of the three forms of $\mu$. The nine choices of parameters are those listed in Table I. It is clear from Figure 3a that the linear law spreads the shock too far to be realistic in the megabar range. The same is true for the power law if $\delta = 3$. The profile determined by the power law depends mainly on the choice of $\delta$, being relatively insensitive to changes in $\eta_0$. While the logarithmic law provides a steep front near the inflection point it is extremely slow in reaching the asymptotic value of 0.15 mb.

Calculations were also made for some parameter choices in the case $X_f = 0.9$. Then $(-\tau_{zz})_f = p_f = 0.51$ mb and a steady plane wave should have an extremely sharp front. The thickness of the profiles, computed by (30), are listed in Table I. The logarithmic law and the power law with $\delta = 5$ are compatible with this requirement.

On the basis of these calculations it is concluded that of the three choices for $\mu$ the power law with $\delta = 5$ provides a reasonable choice for the flow resistance coefficient in the absence of more accurate information. The choices that are being used are:

| | | | | |
|---|---|---|---|---|
| Aluminum: | $S_0 = 0.00162$ | $\eta_0 = 0.003$ | $\delta = 8$ | (31a) |
| Steel: | $S_0 = 0.00125$ | $\eta_0 = 2.7$ | $\delta = 6$ | (31b) |

These values lie within the range of values listed in Table II.

The choices (31) have been incorporated into PICWICK and some calculations made to investigate:

a) The strain-rate effect in the cavitation region behind the shock front where both the pressure and the strain-rate are less than is the front itself, and

b) The strain-rate effect on the pulse itself after it has decreased to the order of tenths of megabars and below.

At the time this report is being assembled, the calculations are not complete but some conclusions may be drawn.

Aluminum-aluminum PICWICK calculations with the choice (31a) for $\mu$ have been carried out for impact velocity $v_0 = 0.76$ cm/$\mu$sec. The calculations are available to $t = 1.081$ $\mu$sec. At this stage the peak pressure has dropped below 0.3 mb and only slight changes in either (a) or (b) are discernible when compared to an identical calculation with $\mu = 0$. Plots of the mass distribution at $t = 0.209$ and 1.081 $\mu$sec for the case $\mu > 0$, are shown in Figures 5a and 5b, respectively. (This type of mass point plot is described more fully in Part II.)

The fact that the inclusion of $\mu$ does not alter the flow process significantly until the pressures are well below 1 mb are used in the next part of this report as justification for continuing the hydrodynamic calculations to relatively low pressures. The limit of the validity of the hydrodynamic model probably lies between 0.04 and 0.3 mb since Jones, Neilson and Benedick [11] have observed stress profiles in explosively generated plane waves in aluminum and iron up to 0.04 mb. They have not, however, determined the effect of varying the load level.

## PART II: IMPACT INTO A THICK TARGET

Immediately upon impact of a metal projectile and metal target at a hypervelocity, pressures of the order of megabars are produced near the contact interface. Shock fronts originating at the contact surface then propagate upward into the projectile and downward into the target (Figure 1). From the initial instant a rarefaction wave, originating at the periphery of the contact surface, propagates into the high pressure region at a velocity greater than the shock velocity. The rarefaction wave thus catches up with and degrades the shock fronts in the projectile and target. The edge rarefaction wave separates the unrelaxed pressure pulse into two regions upon propagating inward to the axis of symmetry. Rarefaction waves also occur when the shock fronts in projectile and target reflect at free surfaces of the projectile target configuration.

The shock dynamics during the early stages after impact of a right circular cylinder have been studied in detail [12]. It suffices here to use the results of the study in interpreting the flow fields computed using the PICWICK code. Calculated points in space and time at which the pressure pulse, the rarefaction waves, and the geometry interact are listed in Table IV. The definitions of the notations used in the following discussion are also given there.

After describing the salient features of the flow field, the total forward momentum, the total outward momentum, and peak pressure at various stages of the flow process are studied. It will be shown that upon taking into account the different time origins of equivalent pressure pulses, energy scaling is accurately predicted.

### FLOW FIELDS FOR THICK TARGETS

In the basic numerical scheme used for the PICWICK calculations the projectile and target materials are represented by discrete mass points. The distribution of the points at any stage of the calculations represents the projectile target configuration at that instant. The area density of the points illustrates the relative mass density of the material and is indicative of the pressure existing at that point in space and time. In Figure 4 the distribution of the mass point representation of the projectile-target configuration at the instant of impact is presented. The PICWICK code provides for automatic plots at the desired time cycles during a computational run. A sequence of mass point distributions at various stages of a given impact calculation illustrates the flow process in a vivid manner.

In Figures 5, 6, and 7, representative sequences of mass particle plots are reproduced. An outline of the original projectile-target configuration is superimposed on the plots for reference purposes. All these calculations were carried out for a cylindrical projectile of radius equal to length and a thick target ($L = \ell = .26192$ cm and $h = \infty$ in Figure 1). The volume of the projectile is the same as that of a 3/32" diameter sphere.

The characteristic mechanisms familiar from experimental studies are clearly illustrated by these plots. These include the formation of the backsplash at the periphery of the forming cavity and the propagation of a nearly hemispherical shock wave into the target. Some of the basic but more subtle effects that have not been observed experimentally may also be detected.

Figure 5a depicts the situation .209 $\mu$sec after aluminum-aluminum impact at .76 cm/$\mu$sec. The rear surface of the projectile remains undisturbed since it has not yet been reached by the shock wave in the projectile, $\tau_1 > .209$ according to Table IV. The shock fronts in projectile and target remain planar near their axis since there they have not yet been caught by the edge rarefaction wave, $t_1 = t_2 > .209$.

Figure 5b illustrates the same calculation only at 1.080 $\mu$sec after impact. The mesh used in the computational scheme has been repartitioned to permit a greater volume of the target to be examined by the same number of computational cells [3]. At this stage the shock in the target has been relaxed at the axis, $1.080 > t_1$, and propagates on a nearly hemispherical front. The amplitude of the pressure pulse, however, decreases from a maximum value at the axis to zero at the surface of the target where it is reflected, causing material to be spalled and ejected backward from the target face.

The sequence of plots in Figure 6 again depicts aluminum-aluminum impact but at $v_0 = 2.0$ cm/$\mu$sec. Figure 6b depicts a phenomenon that always occurs in these thick target calculations. A high density region is formed in the target about one projectile radius beneath the center of impact. From Table IV it may be seen that for all cases considered $R_1/L \doteq 1$ and the high density region is located at the center of convergence of the edge rarefaction wave.

Figures 7a through 7e show five stages of the flow process resulting from a lead projectile impacting a thick lead target at 2.0 cm/$\mu$sec. Two repartitions of the mesh were necessary in this run.

## ENERGY VERSUS MOMENTUM SCALING

Calculations for like metal impact of aluminum and lead are available (for $v_0 = .76$ and $v_0 = 2.0$ cm/$\mu$sec) from the instant of impact until the pressure has decreased to about .2 mb. Strain-rate and strength effects may begin to become

important at these final pressures, the hydrodynamic model has been a valid approximation to this point. The hydrodynamic equations may be put into a dimensionless form, but not the equation of state since it is an empirical fit. Except for this it would clearly be possible to apply the results, with the proper scaling factors, to any geometrically similar impact situation at the same velocity and the same material.

To determine if the equation of state form prevents direct scaling the lead-lead impact at 2.0 cm/μsec was re-run with the configuration scaled up in dimension by a factor of three. The results were practically identical to the scaled version. Since the form of the equation of state is identical for all the metals considered, it was concluded that scaling is justified in the hydrodynamic regime for similar geometries of a given metal and impact velocity.

The calculations at hand are sufficient to resolve a fundamental problem of hypervelocity impact research. Both experimental and theoretical investigators are divided as to the manner in which the depth of penetration of a projectile varies with impact velocity [5]. Some have concluded that the cratering process is determined by the momentum of the impacting projectile; others have concluded that the projectile energy is the governing factor.

These hypotheses will be tested by comparing the impact calculations at $v_0 = 2.0$ cm/μsec with the impact calculations at $v_0 = .76$ cm/μsec, where the latter are scaled to give either equal energy or equal momentum:

(Equal Energy)

$$L = \ell = .26192 \text{ cm} \qquad v_0 = 2.0 \text{ cm/}\mu\text{sec}$$

$$L'/L = (v_0/v_0')^{2/3} = 1.906 \qquad v_0' = .76 \text{ cm/}\mu\text{sec} \tag{32a}$$

$$\text{Mass}'/\text{Mass} = (L'/L)^3 = (v_0/v_0')^2 = 6.9252$$

(Equal Momentum)

$$L = \ell = .26192 \text{ cm} \qquad v_0 = 2.0 \text{ cm/}\mu\text{sec}$$

$$L'/L = (v_0/v_0')^{1/3} = 1.38 \qquad v_0' = .76 \text{ cm/}\mu\text{sec} \tag{32b}$$

$$\text{Mass}'/\text{Mass} = (L'/L)^3 = v_0/v_0' = 2.632$$

The corresponding formulas for the depth of penetration are

(Equal Energy)

$$\frac{P_c}{L} = K_e v_o^{2/3} \tag{33a}$$

(Equal Momentum)

$$\frac{P_c}{L} = K_m v_o^{1/3} \tag{33b}$$

Two important characteristics of the flow field are the total forward momentum and the total outward radial momentum present within the target at any instant of time:

$$Z_+ = \sum_{i,\,j} M_i^j (v_+)_i^j \qquad R_+ = \sum_{i,\,j} M_i^j (u_+)_i^j . \tag{34}$$

The plus indicates that the sums are extended only over positive values of u and v. The results at $v_o$ = .76 cm/μsec under the hypothesis of equal energy are scaled by multiplying R+ and Z+ by 6.9252 and length and time by 1.906. Momentum scaling requires that R+ and Z+ be multiplied by 2.632 and that length and time be multiplied by 1.38.

In Figure 8 the calculated total forward axial momentum is plotted as a function of time for aluminum impact at $v_o$ = 2.0 cm/μsec. Also shown for comparison are the total forward axial momentum when the $v_o$ = .76 cm/μsec results are energy scaled and when they are momentum scaled. In Figure 9 the calculated total outward radial momentum is shown for the same three impact situations.

In Figures 10 and 11, respectively, the calculated Z+ and R+ values are shown as a function of time for lead-lead impact at $v_o$ = 2.0 cm/μsec. The energy scaled and momentum scaled versions of the $v_o$ = .76 cm/μsec calculations are again shown for comparison.

It is clear from these results that momentum scaling cannot be justified, but that energy scaling of the results of the $v_o'$ = .76 calculations gives values of Z+ and R+ that become closer to the $v_o$ = 2.0 cm/μsec values as time is increased. If one only considers these total momentum curves, it appears that energy scaling slightly overestimates the velocity dependence of the hypervelocity damage mechanism and that the exponent in the penetration formula, (33), should be slightly

smaller than 2/3. This was the conclusion of Walsh and Tillotson [13] in their recent and important paper. They found that an exponent between .58 and .72 brought their energy equivalent Z+ and R+ curves into close agreement. Different values of the exponent were required for different velocity ranges and for different metals.

The results discussed in the next section show that this apparent variation in the exponent for different materials and velocity ranges may be explained by the failure to account for a time differential when comparing equivalent energy impacts.

## THRESHOLD OF ENERGY SCALING

When comparing the deformation waves associated with two impact velocities of equivalent energy, $v_0 > v$, the characteristics during the initial stages are of course quite distinct. The higher velocity projectile will produce larger pressures upon impact and the pressure pulse will propagate at a faster velocity into the target. The pressure pulse associated with the lower velocity will require more time to reach a specified distance below the target surface.

To determine the time lag, $\Delta t$, between pressure pulses of equal energy the peak axial pressure has been studied. In Figure 12 the distance of the peak axial pressure below the original target surface is plotted as a function of the time for aluminum-aluminum impact at $v_0 = 2.0$ cm/$\mu$ sec and for the energy equivalent situation for impact at $v_0' = .76$ cm/$\mu$ sec. In Figure 13 the corresponding peak axial pressure versus time curves are shown for lead-lead impact. The time lag for the aluminum and the lead are $\Delta t = .35$ and $\Delta t = .75$ $\mu$sec, respectively.

Since the pressure pulse is the basic cause of the cratering process two impact situations should be compared at times when the pulses are equal distance below the target surface. Accordingly, the energy scaled versions of Z+ and R+ in Figures 8 and 9 should be shifted to the right a distance corresponding to $\Delta t = .35$ $\mu$sec.* The corresponding curves in Figures 10 and 11 are to be shifted $\Delta t = .75$ $\mu$sec to the right. In each figure the dashed curve represents the energy scaled version with the appropriate time correction. For both aluminum and lead this correction leads to excellent agreement between the energy equivalent impact situations.

In Figures 14 and 15 the magnitude of the peak axial pressure pulse as a function of the distance below the target surface is shown for $v_0 = 2.0$ cm/$\mu$ sec and for the momentum and energy equivalent versions of the $v_0' = .76$ cm/$\mu$ sec calculations. Figure 14 illustrates the aluminum calculations and Figure 15 shows the lead calculations. For aluminum impact energy scaling results in overlapping values for the pressures when $\rho < .2$ mb. The results are especially convincing for the lead calculations where the energy scaling gives values that coalesce for $\rho < 1.0$ mb.

---

*The same shifting is required for the momentum scaled version but would only increase the disparity between the momentum equivalent situations.

One megabar is far above the threshold of strength and strain-rate effects in lead and hence, penetrations must certainly follow the two-thirds power law, (32a). On the other hand it is uncertain that 0.2 mb is greater than the threshold pressure for strength and strain-ratio effects for aluminum or aluminum alloys. However, if experimental data shows that the penetration of geometrically similar projectiles into their targets of a given alloy varies according to $v_0^{2/3}$ at the upper end of the experimental range, it is safe to extrapolate at least to $v_0 = 2.0$ cm/$\mu$ sec.

A corollary to this is that if the 2/3 law is attained for two aluminum alloys but with different values of $K_e$, this difference will persist. Strength and strain-rate effects will not disappear with increasing impact velocity. They will continue to become predominant during the latter stages of the cratering process.

## PART III: IMPACT INTO PLATES

Since practical structures are not of unlimited thickness, impacts into plate targets have also been investigated. The presence of the opposite free surface of the target allows the relief of the pressure pulse by a reflected rarefaction wave resulting in the formation of the familiar spallation bubble, Figure 1. Relatively thin plates (thickness less than half the ballistic limit) are completely penetrated before the pressure pulse has attenuated sufficiently for strength and strain-rate effects to become important. These will determine the final diameter of the hole in the target, but a description of the debris in the spallation bubble may be obtained from the hydrodynamic model.

The calculations were all made for a projectile-target configuration with $L = \ell = h = .26192$ cm, but as discussed earlier the results may be scaled to any geometrically similar impact of the same materials at the same velocity.

### FLOW FIELDS FOR PLATE TARGETS

The sequence of Figures 16a through 16d depict the pressure pulse propagation, the cratering process and the creation of a spallation bubble for aluminum-aluminum impact at $v_0 = .76$ cm/$\mu$sec. Figures 17a and 17b depict aluminum-aluminum impact at 2.0 cm/$\mu$sec and Figures 18a through 18d show the results of the calculations for iron-iron impact at .76 cm/$\mu$sec. An outline of the projectile-target configuration at the instant of impact is superposed on each plot to provide a frame of reference.

The pressure and velocity fields are also depicted for the $v_0 = .76$ cm/$\mu$sec calculations for both the aluminum-aluminum impact (Figures 19a through 19e) and the iron-iron impact (Figures 20a through 20e.)

When a shock wave reaches a free surface it must be reflected in such a manner that the stress normal to the surface is zero. For normal incidence this is accomplished by the generation of a reflected wave of amplitude equal to the incident wave, but of opposite sign; and by accelerating the reflected surface to twice the particle velocity of the incident wave. By symmetry the shock waves in the projectile and target must reach, respectively, the rear of the projectile and the opposite surface of the target at normal incidence along the axis. Moreover, from Table IV, it may be seen that for the aluminum-aluminum impacts both at $v_0 = .76$ and 2.0 cm/$\mu$sec, $\ell < \ell_0$ and $h < h_0$; consequently there will be an axial region in which the shock fronts have not been relaxed by the edge rarefaction wave. For

the iron-iron impact the shocks at the axis will be caught by the edge rarefaction just prior to the time the shocks reach the free surface.

At the opposite surface of the target, initially at rest, the particle velocity behind the shock is $v_0/2$ so that after the pressure pulse reaches the surface the particle velocity becomes $v_0$. This sudden increase in particle velocity is illustrated by comparing Figure 19b with Figure 19c and Figure 20b with Figure 20c. For points away from the axial region the shock will have been attenuated by the edge rarefaction prior to reaching the free surface. The particle velocity will be $v_0/2 - v(r)$ where the velocity lag, $v(r) > 0$, increases with radial distance r. After the reflection of the pulse at r, the particle velocity is $v_0 - 2v(r)$ so that the velocity lag is doubled.

At the rear surface of the projectile the particle velocity in the central region is $-v_0/2$ in a coordinate system fixed in the rear surface. After reflection the particle velocity in this system is $-v_0$. In the laboratory system, however, the new particle velocity is zero. This sudden decrease in the particle velocity is illustrated by comparing Figure 19b with Figure 19c and Figure 20b with Figure 20c. It is also demonstrated by comparing Figure 16b with Figure 16c and Figure 18b with Figure 18c. The latter plots show that the rear mass particles in the projectile have remained nearly stationary. At points away from the axial region the particle velocity after the reflection becomes $2v(r)$, i.e., increases with r.

The axial portion of the spallation bubble is increasing in length at the rate $v_0$ while the outer portion is increasing in length at the rate $v_0 - 4v(r)$. This produces the elongated geometry of the bubble that is observed experimentally.

## RELEASE OF PRESSURE PULSE

One inference of the calculations is that for the plate thickness and projectile velocities studied, the penetration is completed before much of the energy carried by the pressure pulse can be transmitted radially into the target. This is demonstrated by the pressure profiles shown in Figures 19a through 20e. The pressure in the central region of the projectile-target configuration decreases to zero soon after the pressure pulse is relieved by the presence of the opposite free surface of the target. Once the pressure in the central region decreases to zero the pulse that has propagated radially into the target is no longer supported and attenuates rapidly. For both aluminum and iron impact at $v_0 = .76$ cm/$\mu$ sec the maximum pressure has decreased to approximately .3mb at $r = 2L$. Strength and strain-rate effects will play an important role in the subsequent radial deformation of the target.

The sudden release of the pressure pulse results in a rapid expansion of the material accompanied by a decrease in the internal energy and a corresponding

increase in the kinetic energy. This dramatic change in the partition of the energy is depicted in Figures 21a, 22a, and 23a for, respectively, aluminum impact at .76 and 2.0 cm/$\mu$sec and iron impact at .76 cm/$\mu$sec. Curves are also shown depicting the partition of energy for the corresponding thick target impact situations. Even after the sudden decrease, however, the total internal energy reaches a plateau representing the release temperature resulting from the increase in entropy produced by the shock.

In the special case of two semi-infinite bodies impacting at velocity $v_0$, the kinetic energy and internal energy behind the shock front are equal, I = k.e. = $v_0^2/8$. This equipartition represents an upper limit on the value for internal energy since there are no rarefaction waves present in such an idealized situation.

Figures 21, 22, and 23 also show the total forward momentum and the total outward radial momentum for all three impact situations. Both are seem to increase with time but at a much slower rate than the corresponding thick target impact once the pressure pulse has been relieved.

Since $Z_+$ and $R_+$ are important parameters when considering the effectiveness of plate targets as shields for a protected structure, it may be concluded that the plate should only be as thick as required to break up the projectile. If the spacing is large enough the expanding bubble will then be dispersed over a wide area of the structure.

## CONCLUSIONS

The most important conclusion of this report is that the craters produced by the impact of geometrically similar projectiles of the same metal into a thick target of like metal will be the same if:

(i) The projectiles are of equal kinetic energy

(ii) The impact velocity exceeds a threshold value for energy scaling

This has been concluded from a detailed study of aluminum-aluminum and lead-lead impact at $v_0 = 0.76$ and $2.0$ cm/$\mu$sec. The calculations were carried out for cylindrical projectiles of radius equal to length, $L = \ell$.

The formula for the depth of penetration corresponding to (i) and (ii) is

$$\frac{P_c}{L} = K_e \, v_0^{2/3} \qquad (v_0 \geq v_0^*),$$

where $v_0^*$ is the threshold velocity for the 2/3 law for a particular metal and $K_e$ the corresponding experimental constant. These parameters are known from experiment to vary among alloys of nominally the same metal, reflecting strength and strain-rate effects. The calculations indicate $v_0^* < .76$ for lead and for aluminum except possible aluminum alloys in which strain-rate and strength effects persist for pressures up to .2 mb.

These conclusions are based on a very strict criterion for equivalence of two impact cratering processes. Since the pressure pulse in the target is the basic cause of the cratering mechanism, the two processes are compared at times when the locations of their peak pressures are an equal distance below the target surface. Based on the time since impact, the process associated with the slower impact velocity $v_0'$ lags the other, $v_0$, by $\Delta t$. For equivalence it is required that at these corresponding times the total forward axial momentum $Z_+$, the total outward radial momentum, $R_+$, and the amplitude of the pressure pulse become equal prior to the onset of strength and strain-rate effects.

If one simply compares $Z_+$ and $R_+$ on the basis of time since impact, ignoring the time lag $\Delta t$, an exponent somewhat less than $n=2/3$ would be estimated for the velocity dependence of the penetration law. Since $\Delta t$ increases with increasing $v_0 - v_0'$, the apparent value for the exponent would decrease with increasing impact

velocity. This is believed to explain the discrepancy between the present conclusions and those of Walsh and Tillotson [13] who estimated $n = .65$ $(.5 < v_0 < 1)$, $n = .62$ $(1 < v_0 < 4)$, and $n = .61$ $(10 < v_0 < 25)$.

Calculations were also performed for aluminum and iron plate targets impacted by like metal projectiles at $v_0 = .76$ and 2.0 cm/$\mu$sec (plate thickness h, $h = L = \ell$). The pressure pulse is relieved by the spallation at opposite free surface before much of the energy can be transmitted radially into the target. The pressure in the central part of the configuration rapidly falls to zero and an expanding spallation bubble is formed. The material in the bubble is completely shattered and will remain at a high temperature. The total forward momentum of the configuration after impact exceeds the original axial momentum. If the thickness of the plate is less than the projectile radius $h < L$, the leading central portion of the spallation bubble travels at the velocity of the projectile at impact.

These results indicate that the use of thin plates as shields for structures could result in greater damage to the structure if the spacing between shield and structure is not great enough. The meteor bumper problem will be studied during the next six months of the contract.

## BIBLIOGRAPHY


1. Riney, T. D., "Theory of High Speed Impact", Summary Report, November 3, 1960 - November 2, 1961 (APGC-TDR-62-20).

2. Riney, T. D., "Behavior of Metals During Hypervelocity Impact Cratering", Presented at Eighth Midwestern Mechanics Conference in Cleveland, Ohio, April 3, 1963. To be published in the Conference Proceedings.

3. Riney, T. D., "Solution of Visco-Plastic Equations for Axisymmetric Hypervelocity Impact", Summary Report, November 3, 1961 - November 2, 1962 (APGC-TDR-62-74).

4. Riney, T. D., "Visco-Plastic Solution of Hypervelocity Impact Cratering Phenomenon" Proc. Sixth Symposium on Hypervelocity Impact, Vol. II, Part 1, August, 1963.

5. Eichelberger, R. J., "Theoretical and Experimental Studies of Crater Formation", Proc. Sixth Symposium on Hypervelocity Impact, Vol. II, Part 2, August, 1963.

6. Perzyna, P., "The Study of the Dynamic Behavior of Rate Sensitive Plastic Materials", Brown Univ. Div. Appl. Math., Tech. Rpt. No. 77, Contract No. NONR 562(10), May, 1962.

7. Symond, P. S., and Ting, T. C. T., "Longitudinal Impact on Visco-Plastic Rods - Approximate Methods and Comparisons", Brown Univ. Div. Eng'g., Tech. Rpt. to ARPA, Contract SD-86, August, 1963.

8. Rice, M. H., McQueen, R. G., and Walsh, J. M., "Compression of Solids by Strong Shock Waves", Solid State Physics, Vol. 6, Chap. I, Academic Press, 1958.

9. Osborne, R. K., and his associates in group W-4 at Los Alamos made the equation of state fit.

10. Band, W., "Studies in the Theory of Shock Propagation in Solids", J. Geophys. Research, Vol. 65, February, 1960, p. 695.

11. Jones, O. E., Neilson, F. W., and Benedick, W. B., "Dynamic Yield Behavior of Explosively Loaded Metals Determined by a Quartz Transducer Technique", J. Appl. Phys., Vol. 33, November, 1962, p. 3224.

12. Heyda, J. F., and Riney, T. D., "Penetration of Structures by Hypervelocity Projectiles", (To be published).

13. Walsh, J. M., and Tillotson, J. H., "Hydrodynamics of Hypervelocity Impact", Proc. Sixth Symposium on Hypervelocity Impact, Vol. II, Part 1, August, 1963.

## APPENDIX

Let $\rho$, p, $\vec{u}$ = (u, 0, v), and I denote the density, pressure, velocity, and specific internal energy, respectively. Then the axisymmetric formulation of the visco-plastic equations may be written in the form:

(Mass) $$\frac{\partial\rho}{\partial t} + u\frac{\partial\rho}{\partial r} + v\frac{\partial\rho}{\partial z} + \rho \operatorname{div} \vec{u} = 0 \qquad \text{(A-1)}$$

(Radial Momentum) $$\rho\left(\frac{\partial u}{\partial t} + u\frac{\partial u}{\partial r} + v\frac{\partial u}{\partial z}\right) = \frac{\partial}{\partial r}\left(P+S_{rr}\right) + \frac{S_{rr}-S_{\theta\theta}}{r} + \frac{\partial S_{rz}}{\partial z} \qquad \text{(A-2)}$$

(Axial Momentum) $$\rho\left(\frac{\partial v}{\partial t} + u\frac{\partial v}{\partial r} + v\frac{\partial v}{\partial z}\right) = \frac{\partial}{\partial z}\left(P+S_{zz}\right) + \frac{1}{r}\frac{\partial}{\partial r}\left(rS_{rz}\right) \qquad \text{(A-3)}$$

(Energy) $$\rho\left(\frac{\partial I}{\partial t} + u\frac{\partial I}{\partial r} + v\frac{\partial I}{\partial z}\right) + p \operatorname{div} \vec{u} = \mu D^2. \qquad \text{(A-4)}$$

Here the flow is assumed to be strictly adiabatic and the following notations have been introduced:

$$\left.\begin{aligned}
&P = -p - \frac{2}{3}\mu \operatorname{div}\vec{u} && \operatorname{div}\vec{u} = \frac{1}{r}\frac{\partial(ru)}{\partial r} + \frac{\partial v}{\partial z} \\
&S_{zz} = \mu D_{zz} = 2\mu\frac{\partial v}{\partial z} && S_{rr} = \mu D_{rr} = 2\mu\frac{\partial u}{\partial r} \\
&S_{rz} = \mu D_{rz} = \mu\left(\frac{\partial u}{\partial z} + \frac{\partial v}{\partial r}\right) && S_{\theta\theta} = \mu D_{\theta\theta} = 2\mu\frac{u}{r} \\
&D^2 = D_{rz}^2 + \frac{1}{2}\left(D_{rr}^2 + D_{\theta\theta}^2 + D_{zz}^2\right) - \frac{2}{3}(\operatorname{div}\vec{u})^2 \\
&\tau^2 = \mu^2 D^2 && \tau_{ij} = P\delta_{ij} + S_{ij}
\end{aligned}\right\} \qquad \text{(A-5)}$$

TABLE I

Values for mild steel of the material parameters occurring in relations (3). These values were estimated by Perzyna [6]. Also listed are the corresponding shock thicknesses calculated for the indicated final compression ratios. The units are in the gm-cm-$\mu$sec system.

| Form of $\mu$ | No. | $S_o \times 10^3$ | $\eta_o$ | $\delta$ | $\Delta P$ | |
|---|---|---|---|---|---|---|
| | | | | | $(X_J = .9)$ | $(X_J = .08)$ |
| Linear Law | 1 | 1.62 | 5.2 | -- | 10.3 | -- |
| | 2 | 1.62 | 3.9 | -- | 13.0 | -- |
| | 3 | 1.62 | 3.1 | -- | 17.4 | 7.32 |
| Power Law | 4 | 1.62 | 23.1 | 5 | .01 | $3.0 \times 10^{-6}$ |
| | 5 | 1.62 | 5.2 | 3 | .20 | $2.2 \times 10^{-3}$ |
| | 6 | 1.62 | 3.9 | 3 | .15 | -- |
| Logarithmic Law | 7 | 1.62 | 11.7 | -- | .034 | -- |
| | 8 | 1.62 | 7.8 | -- | .022 | -- |
| | 9 | 1.62 | 3.9 | -- | .011 | $3.6 \times 10^{-21}$ |

TABLE II

Ranges of values estimated by Symonds and Ting [7] for the parameters in the power law for mild steel and structural aluminum. The estimates are based on the results of a number of experimenters.

| Metal | $S_o \times 10^3$ | $\eta_o$ | $\delta$ |
|---|---|---|---|
| Mild Steel | 1.25 | 2.7 - 18 | 4 - 6 |
| Al 6061-T6 | 1.62 | .003 - .154 | 4 - 8 |

TABLE III

Equation of state parameters, occurring in equation (16), expressed in the gm-cm-$\mu$sec system of units.

| Metal | $a_1$ | $a_2$ | $b_o$ | $b_1$ | $b_2$ | $c_o$ | $c_1$ | $\phi_o$ | $\rho_o$ |
|---|---|---|---|---|---|---|---|---|---|
| Al | 1.1867 | .763 | 3.4448 | 1.5451 | .9643 | .43382 | .54873 | 1.5 | 2.702 |
| Fe | 7.78 | 31.18 | 9.591 | 15.676 | 4.634 | .3984 | .5306 | 9.0 | 7.86 |
| Pb | 1.4844 | 1.6765 | 8.7317 | .96473 | 2.6695 | .27732 | .43709 | 3.3 | 11.34 |

TABLE IV

Points in time and space at which the shock fronts, rarefaction waves, and the configuration surfaces interact. The values in this table were supplied by Dr. J. F. Heyda and are valid for like metal impact.

| Point of Interaction | $v_o$ = .76 cm/$\mu$sec | | | $v_o$ = 2.0 cm/$\mu$sec | | |
|---|---|---|---|---|---|---|
| | Al | Fe | Pb | Al | Fe | Pb |
| $t_1/L = t_2/L$ | 1.116 | .963 | 1.208 | .658 | .499 | .737 |
| $R_1/L$ | 1.178 | .963 | .938 | 1.188 | .945 | 1.142 |
| $R_2/L$ | .330 | .231 | .019 | -.127 | -.053 | -.332 |
| $t_i/L$ | .891 | .827 | 1.090 | .581 | .456 | .683 |
| $R_i/L$ | .339 | .314 | .414 | .581 | .456 | .683 |
| $\tau_1/\ell$ | .947 | 1.000 | 1.289 | .553 | .528 | .645 |
| $\ell_o/L = h_o/L$ | 1.178 | .963 | .938 | 1.188 | .945 | 1.142 |

$t_1$ = time for edge rarefaction to catch shock front in target at the axis

$t_2$ = time for edge rarefaction to catch shock front in projectile at the axis

$R_1$ = position of shock front in target at $t_1$

$R_2$ = position of shock front in projectile at $t_2$

$t_i$ = time for edge rarefaction to first reach axis at moving interface

$R_i$ = position of interface at $t_i$

$\tau_1$ = time required for shock in projectile to reach its rear surface

$\ell_o$ = projectile length for which $t_2 = \tau_1$

$h_o$ = plate thickness for which edge rarefaction reaches axis in target simultaneously with the shock

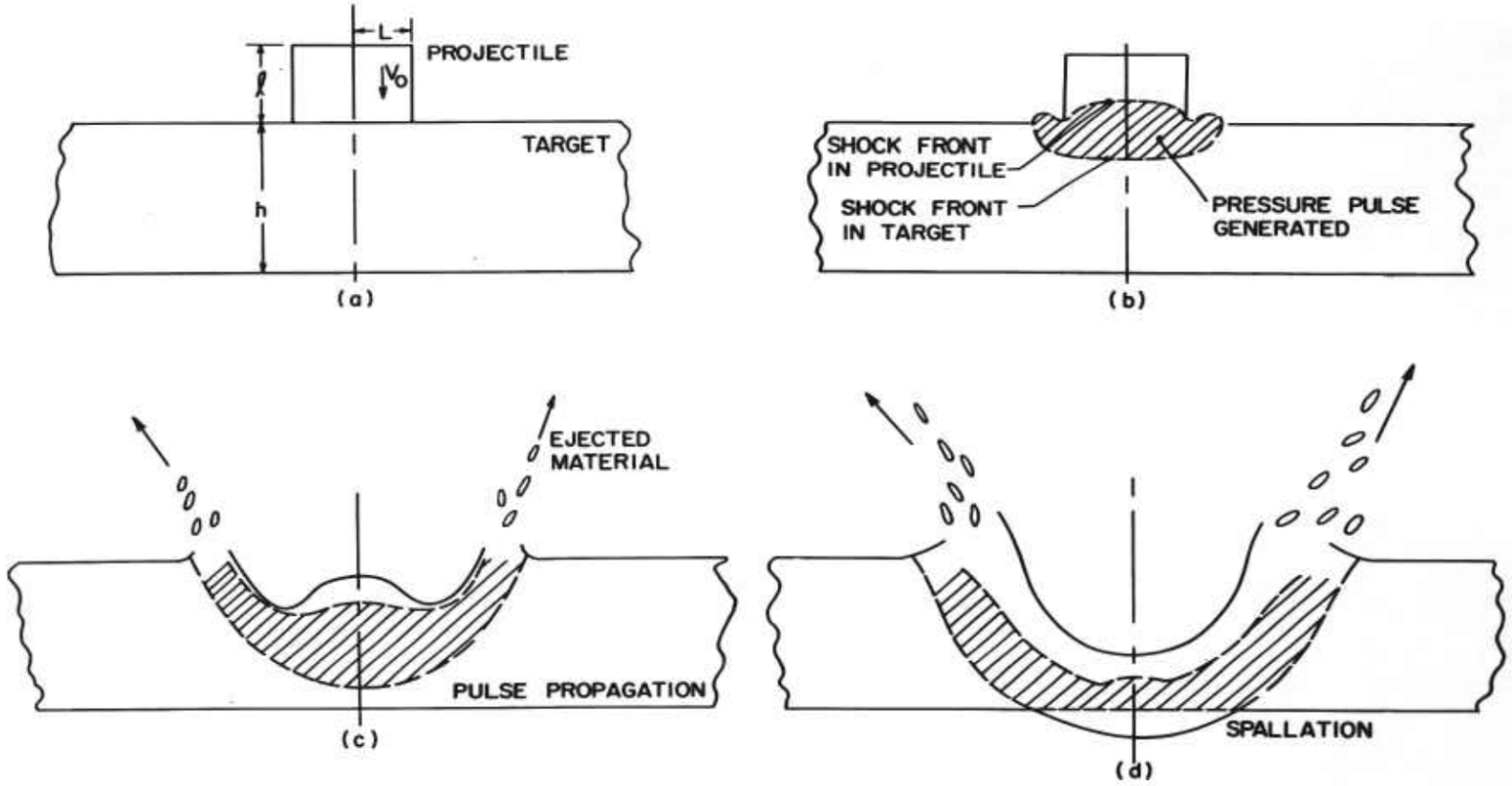


Figure 1. Illustration of the cratering and penetration of a structural member by a hypervelocity projectile: (a) axial section of configuration at impact, (b) generation of pressure pulse between shock fronts in projectile and target, (c) material ejected from target surface and the pressure pulse propagates into the target, (d) spallation at opposite free surface resulting from reflection of pressure pulse.

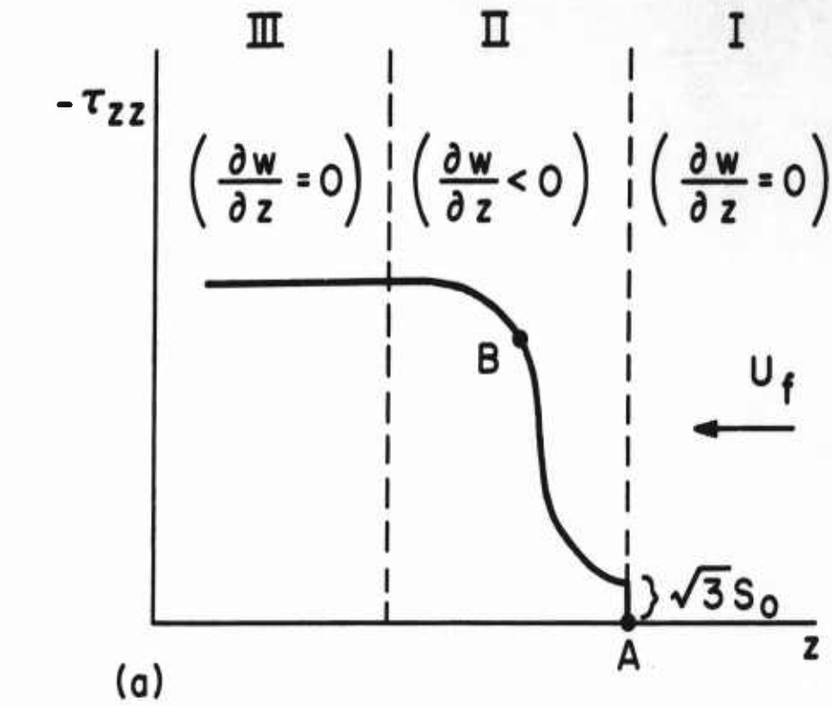


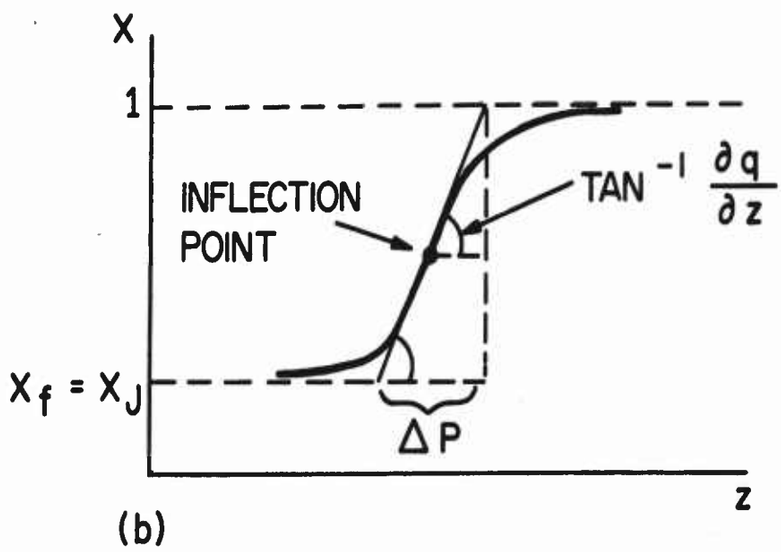


Figure 2. Illustration of the features of the front of a steady one-dimensional shock wave in which the strain-rate effect is included: (a) the shock profile depicted in laboratory coordinates, (b) definition of the thickness of the shock front, $\Delta P$.

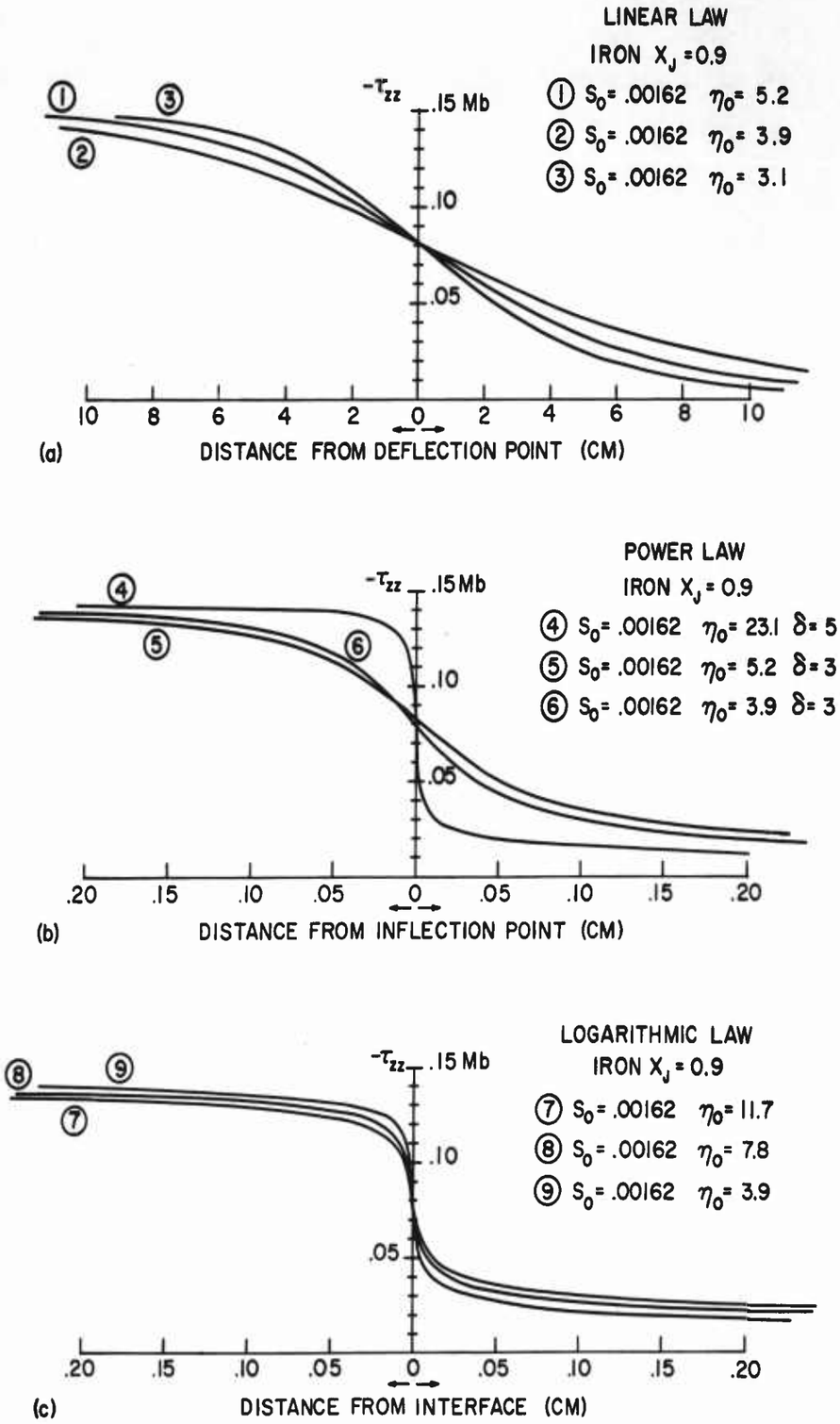


Figure 3. Calculated shock profiles in mild steel for a final compression ratio $X_f = 0.9$ when $\mu$ is assumed to follow (a) linear law, (b) power law, (c) logarithmic law.

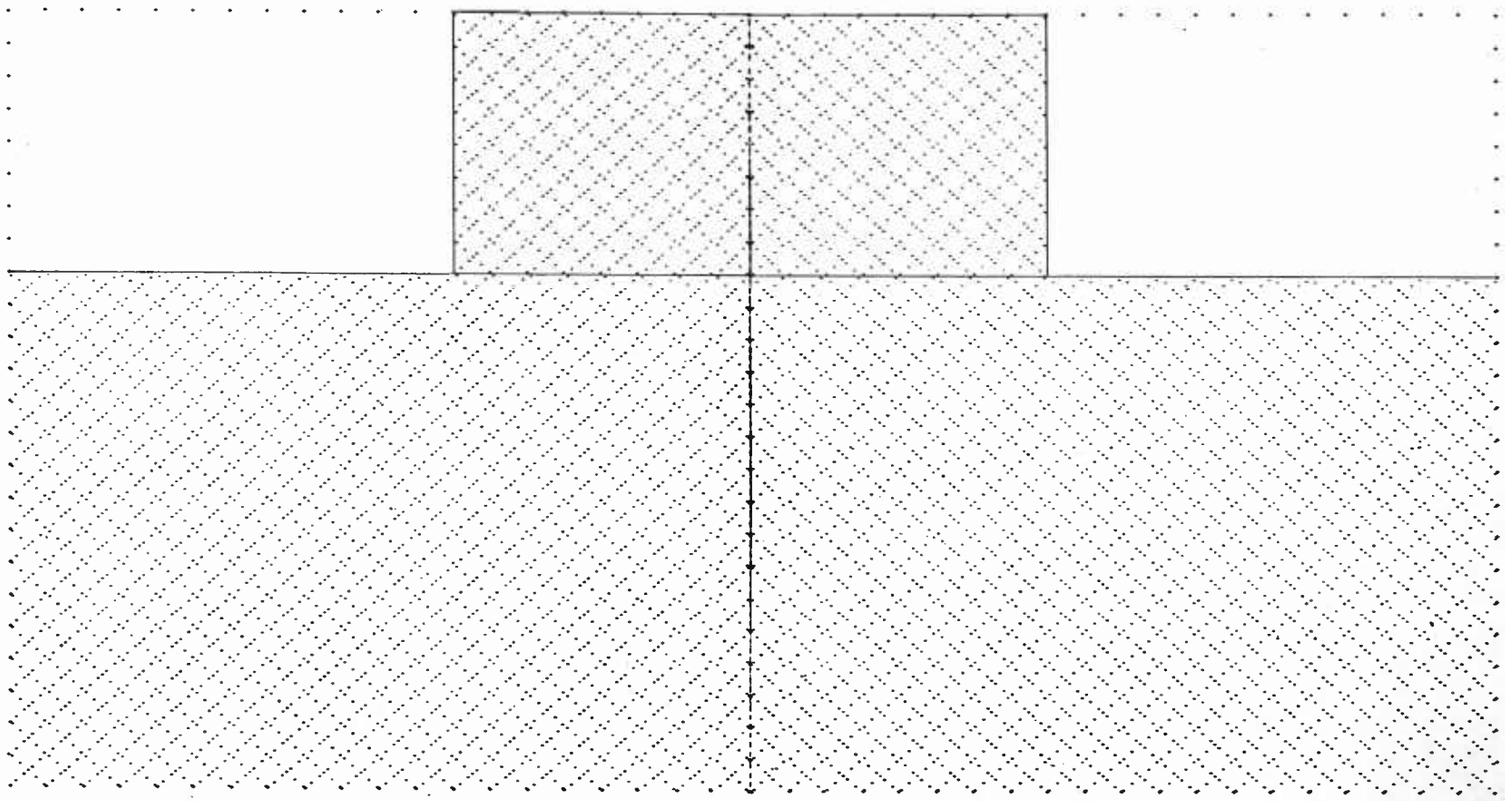

**Figure 4. The distribution of the mass point representation of the axisymmetric projectile-target configuration at the instant of impact.**

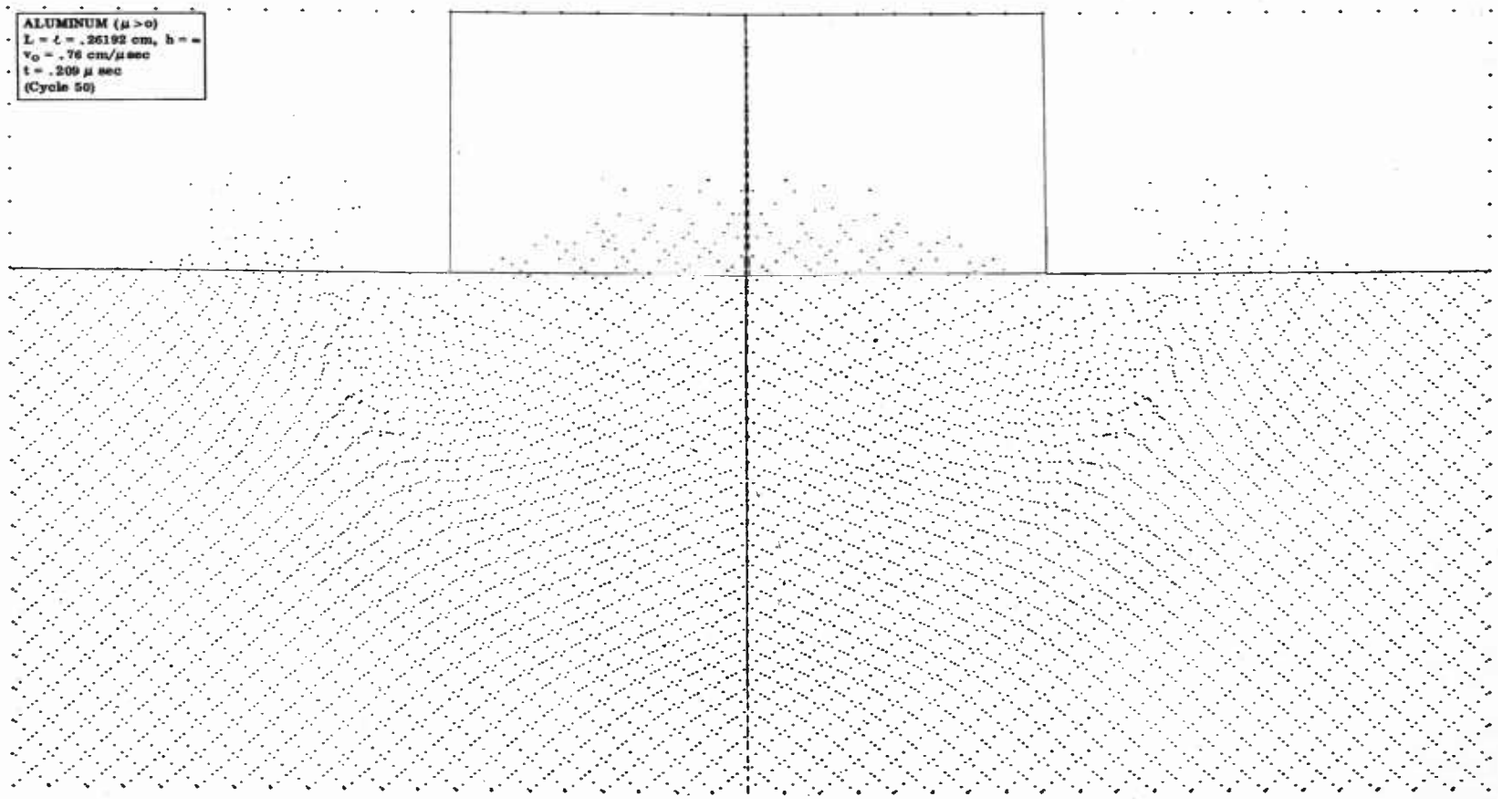


Figure 5a. The mass point plot .209 μsec after impact of an aluminum projectile into a thick aluminum target at .76 cm/μsec.

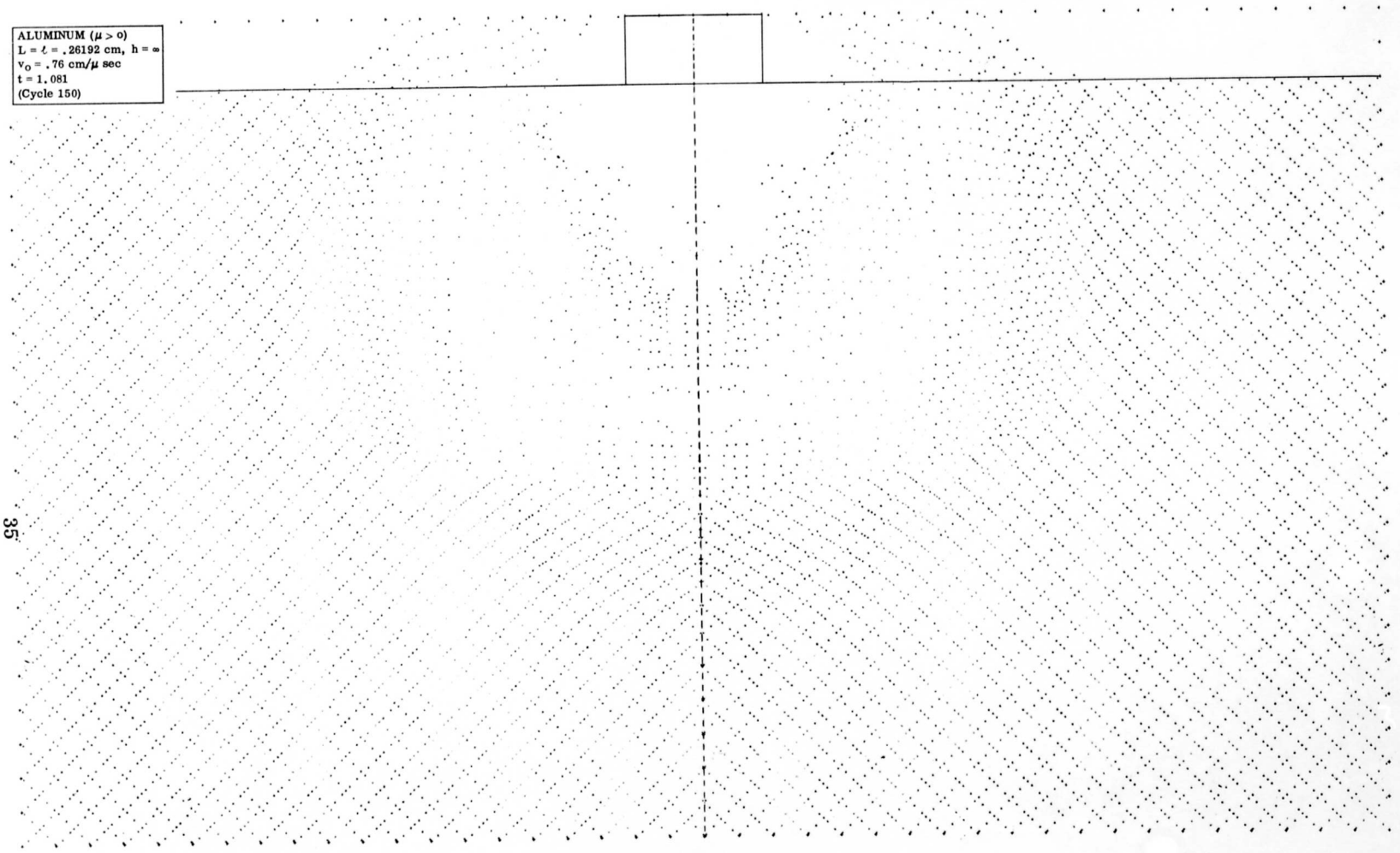


Figure 5b. The mass point plot 1.080 $\mu$sec after impact of an aluminum projectile into aluminum target at .76 cm/$\mu$sec.

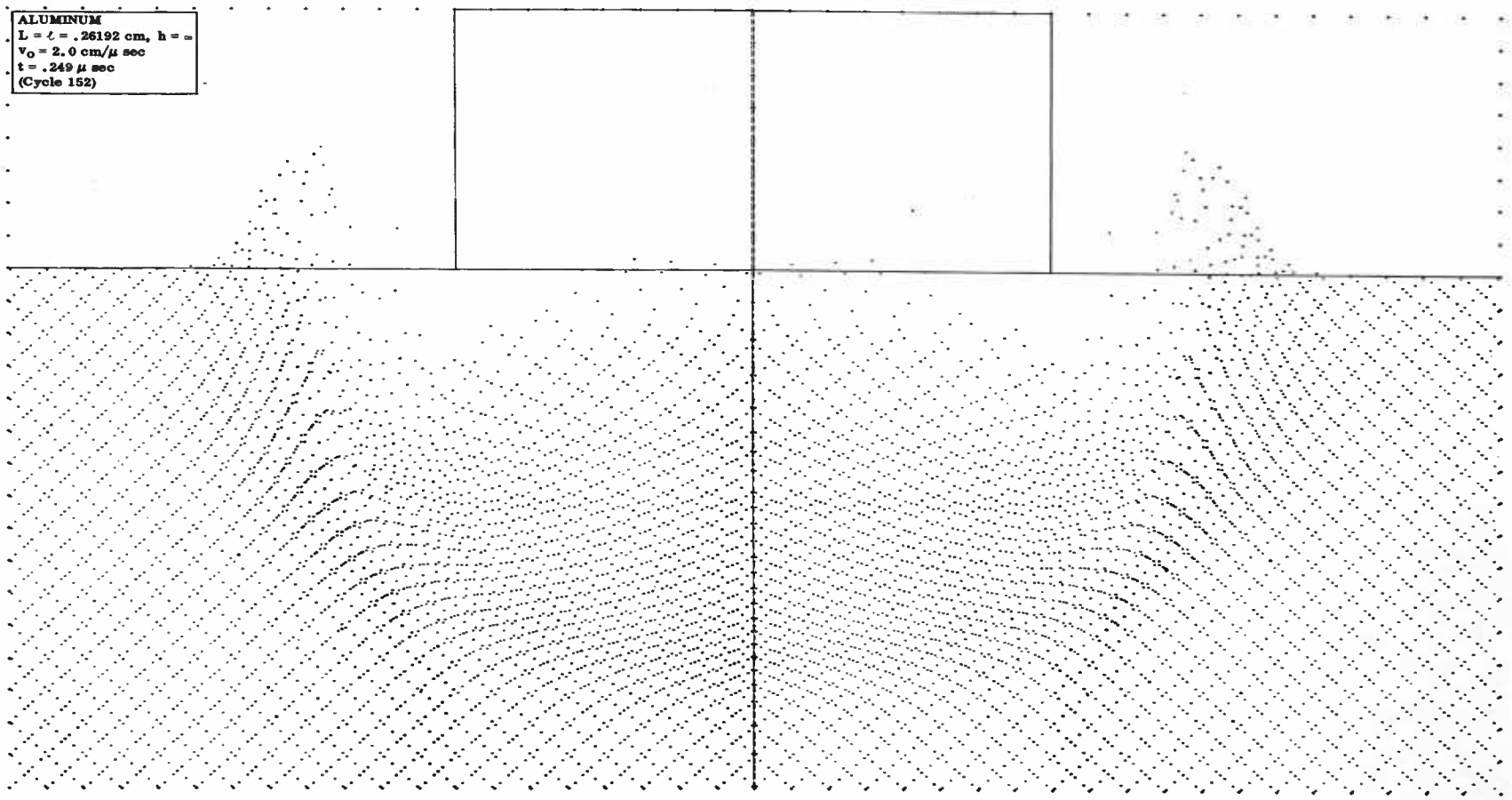


Figure 6a. The mass point plot .249 μ sec after impact of an aluminum projectile into a thick aluminum target at 2.0 cm/μsec.

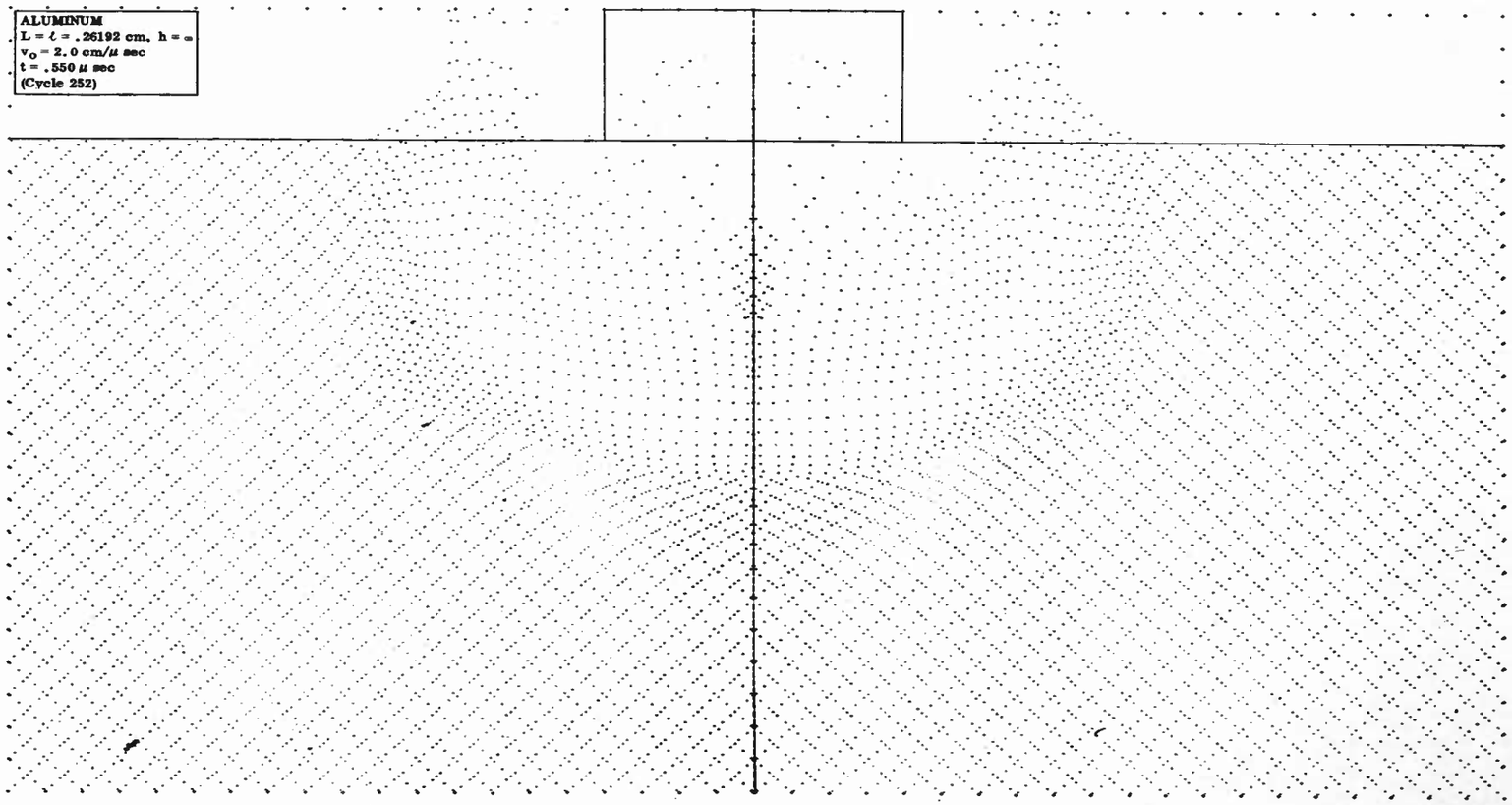


Figure 6b. The mass point plot .550 μ sec after impact of an aluminum projectile into a thick aluminum target at 2.0 cm/μsec.

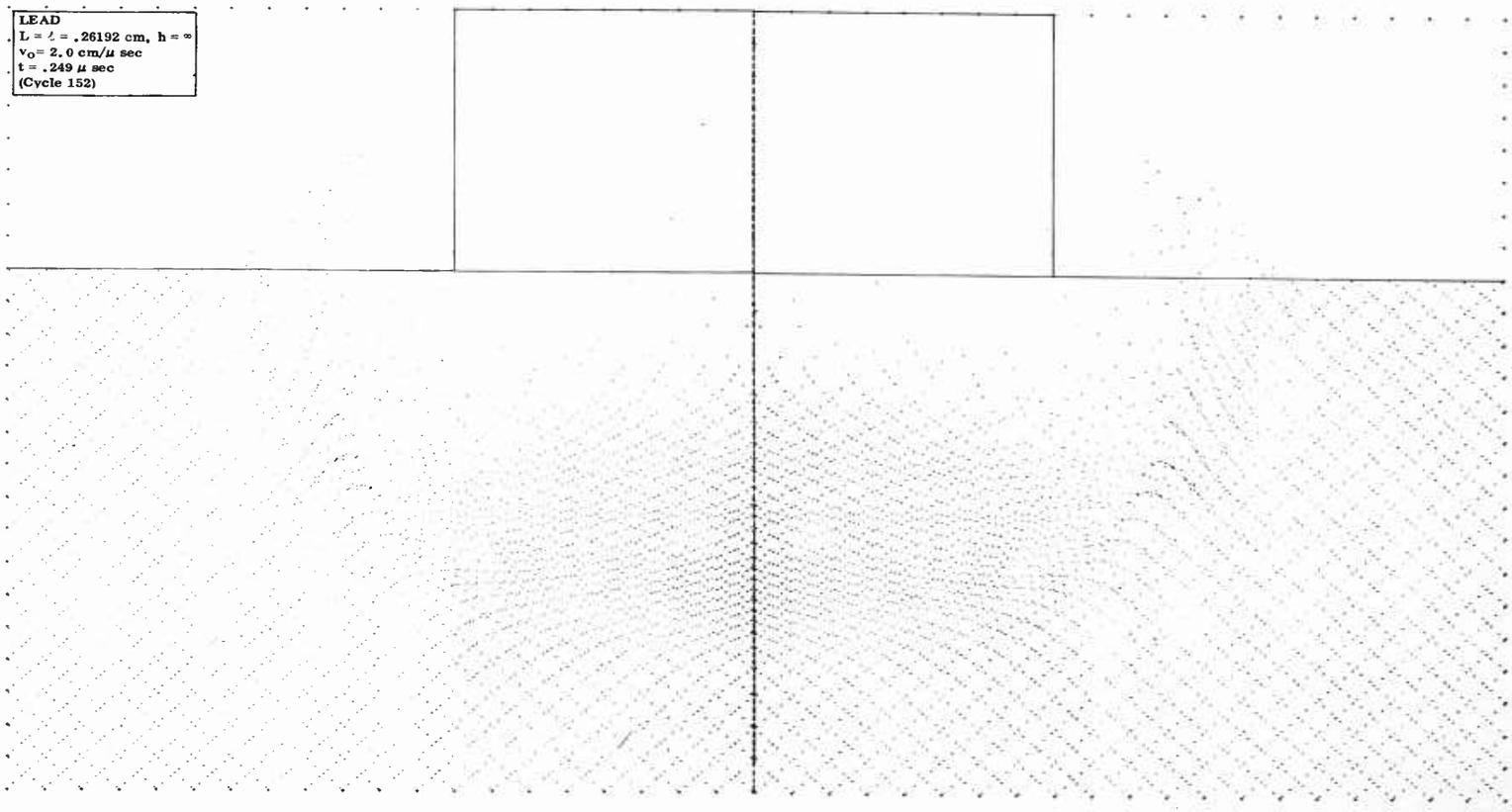


Figure 7a. The mass point plot at t = .249 μsec after impact of a cylindrical lead projectile into a lead target at $v_0$ = 2.0 cm/μsec.

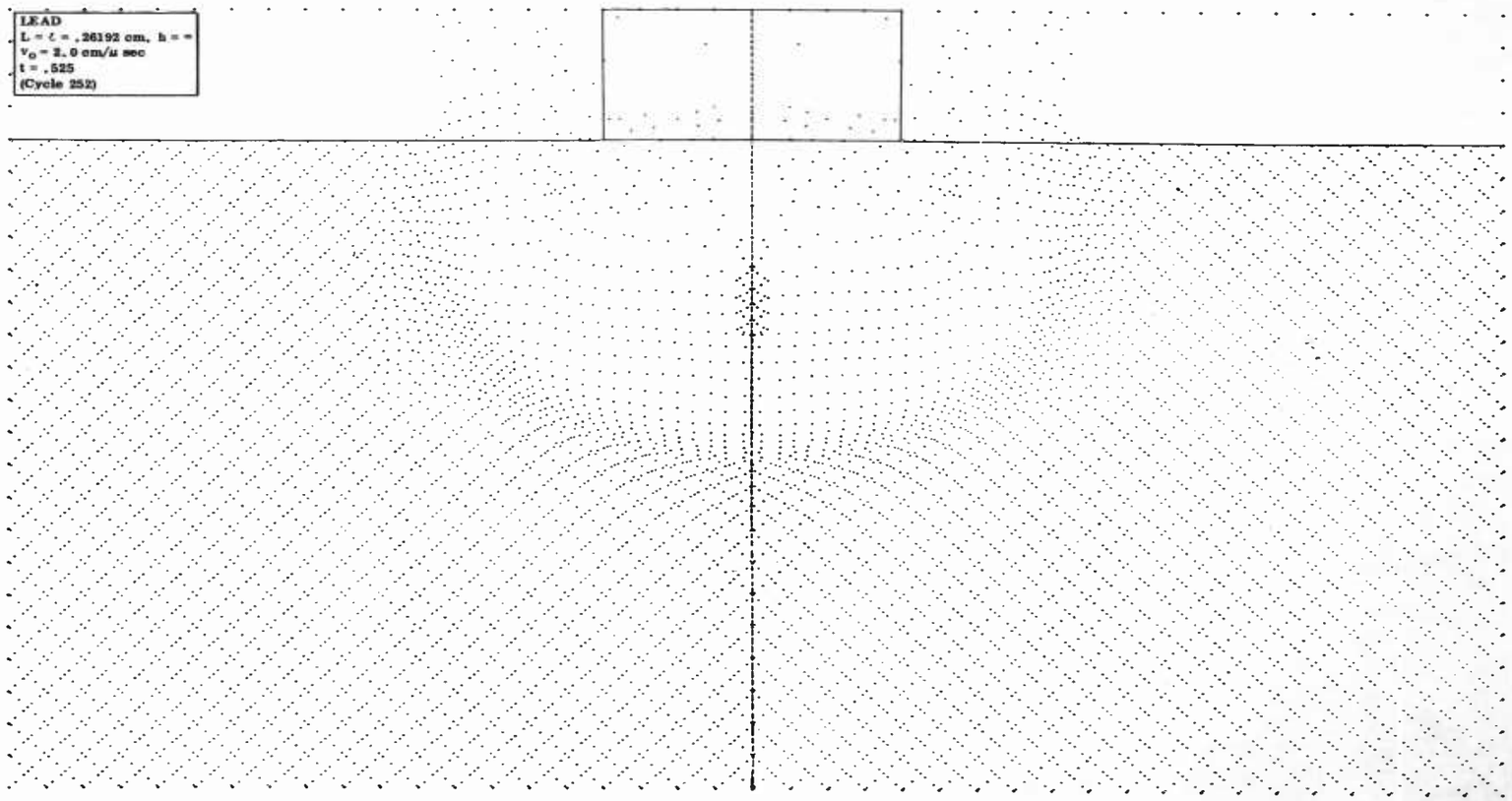


Figure 7b. The mass point plat at t = .525 μsec after impact of a cylindrical lead projectile into a thick lead target at $v_o$ = 2.0 cm/μsec.

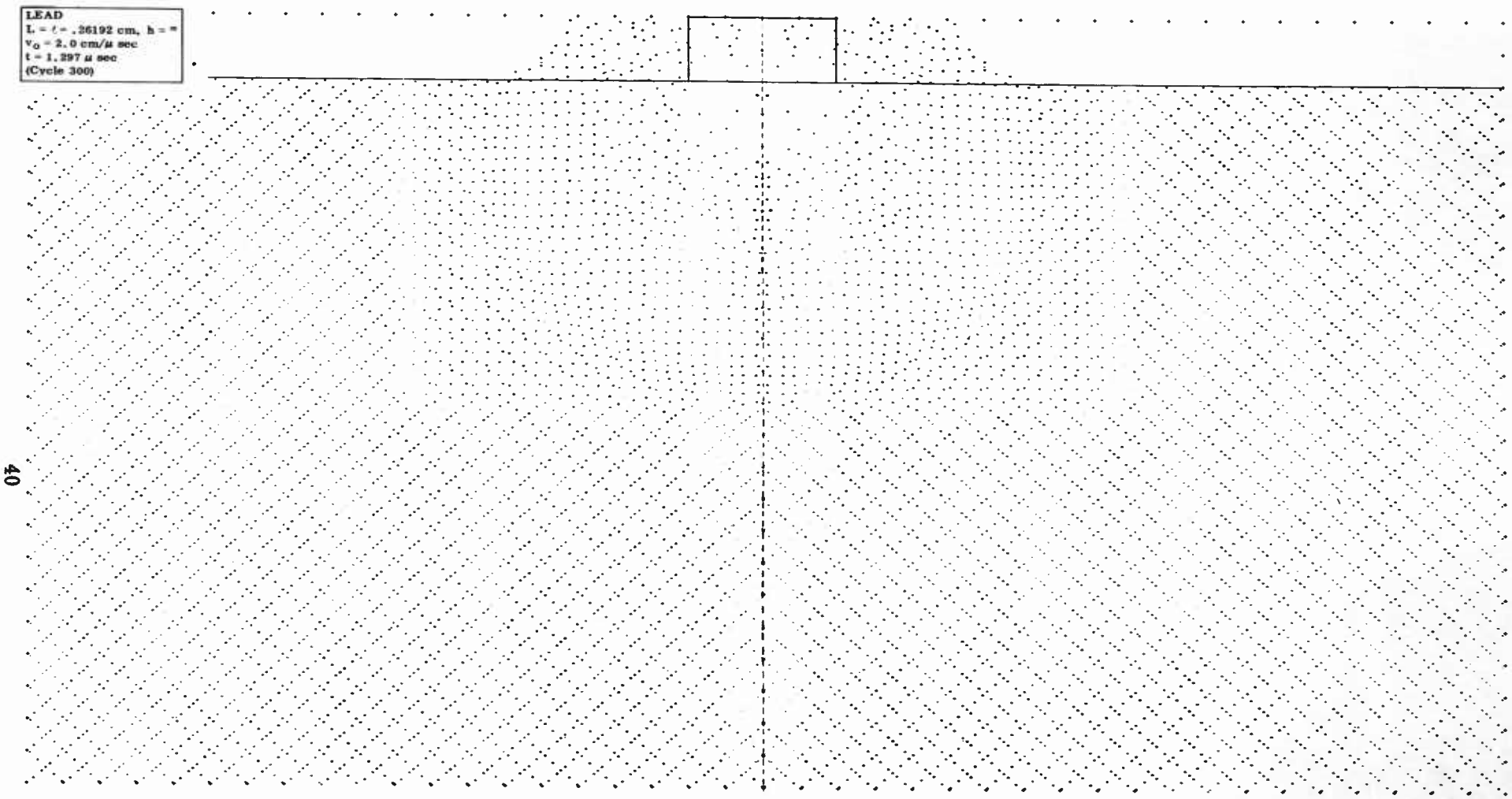


Figure 7c. The mass point plot at t = 1.297 μsec after impact of a cylindrical lead projectile into a thick lead target at $v_0$ = 2.0 cm/μ sec.

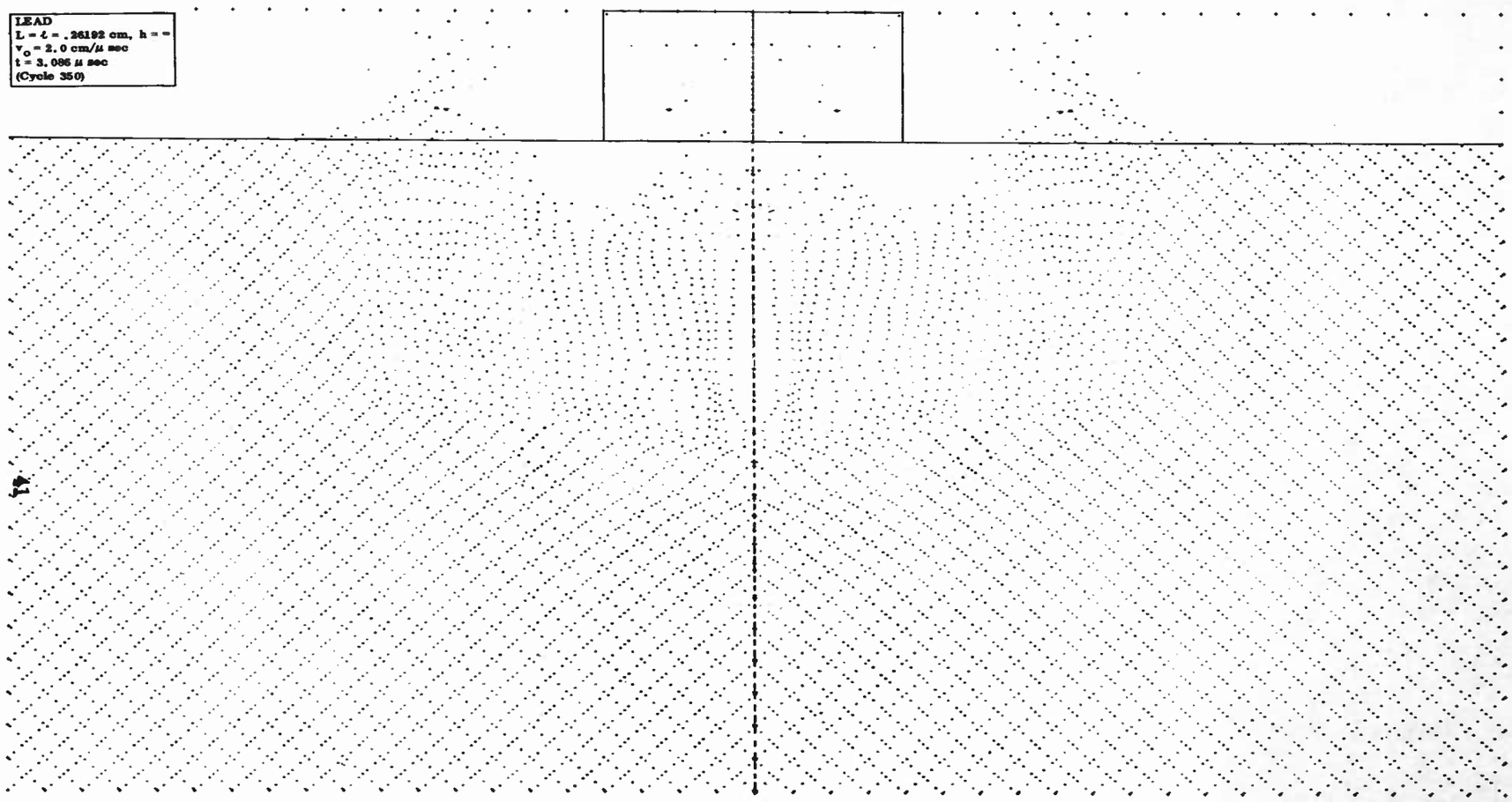


Figure 7d. The mass point plot at t = 3.086 $\mu$ sec after impact of a cylindrical lead projectile into a thick lead target at $v_o$ = 2.0 cm/$\mu$sec.

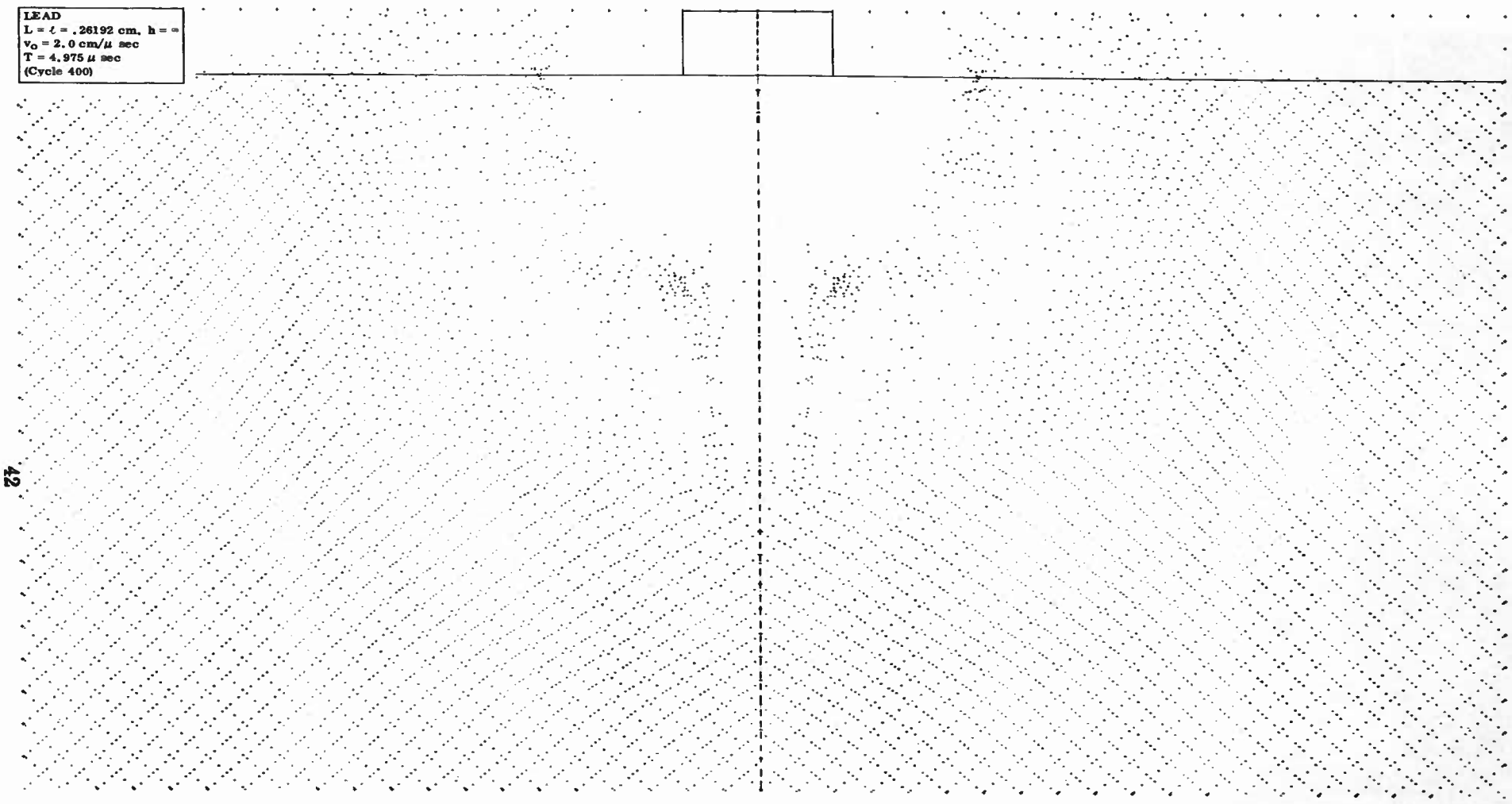


Figure 7e. The mass point plat at t = 4.975 μsec after impact of a cylindrical lead projectile into a thick lead target at $v_o$ = 2.0 cm/μsec.

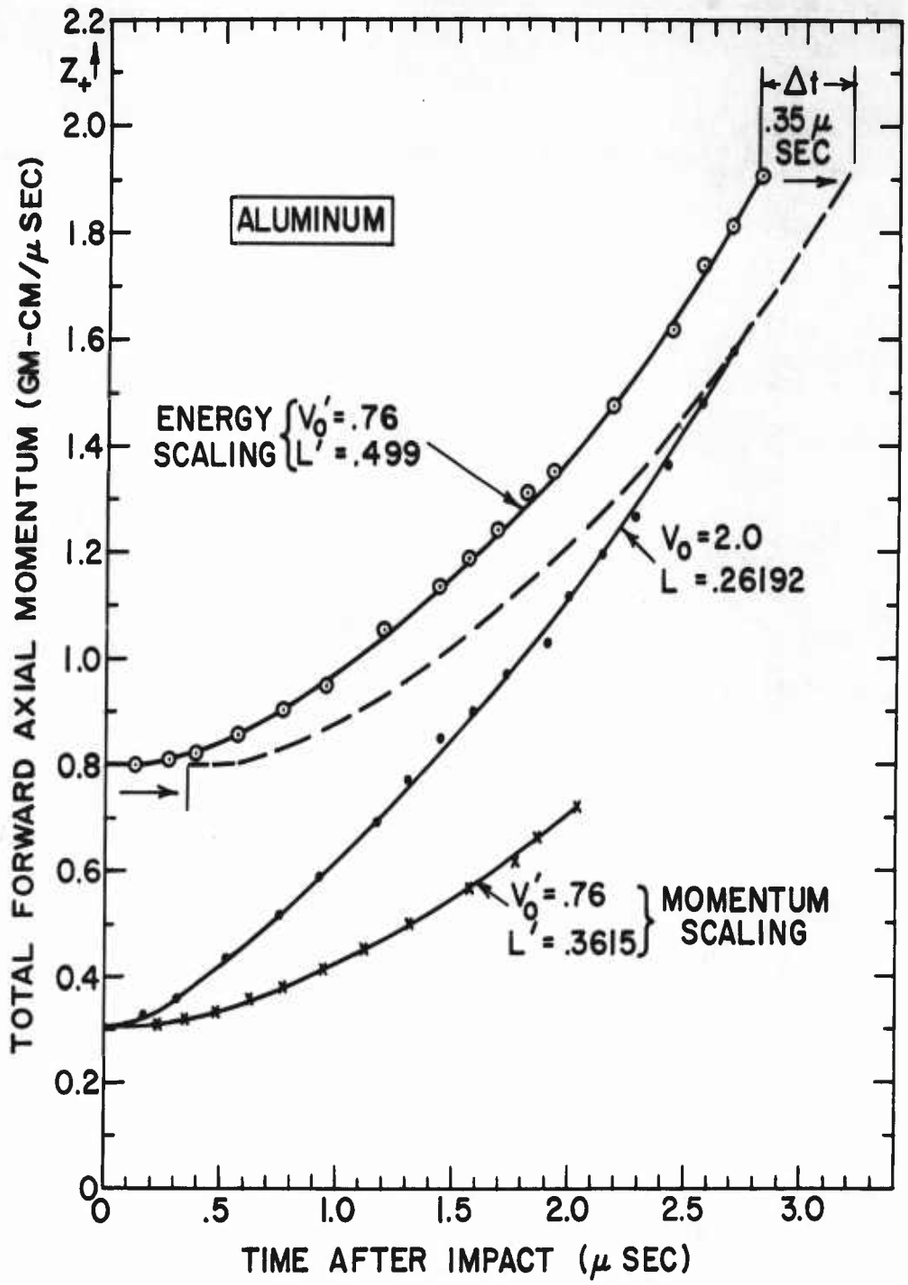


Figure 8. Total forward momentum in the target as a function of the time since impact of an aluminum projectile and a thick aluminum target.

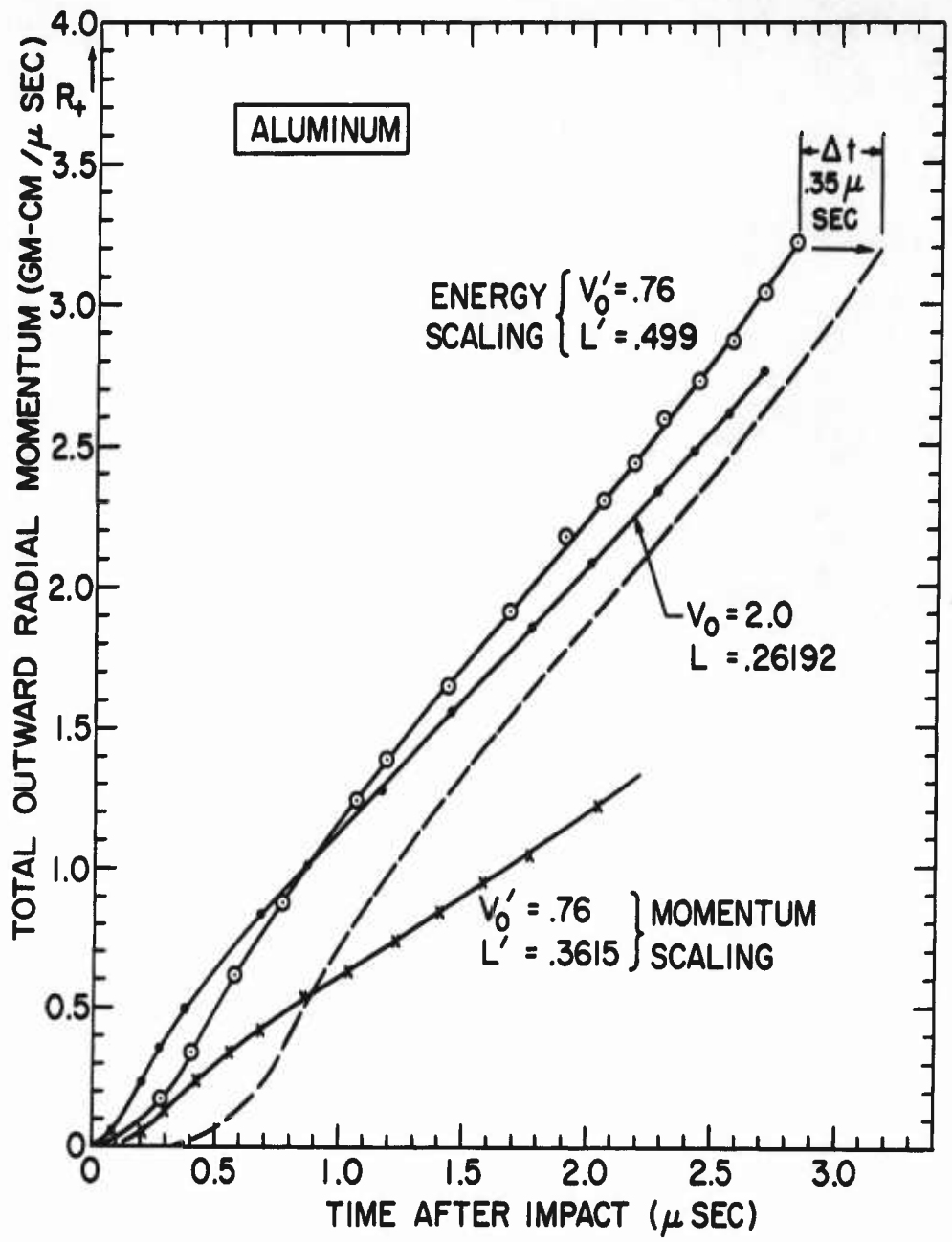


Figure 9. Total positive radial momentum in a thick aluminum target at indicated time since impact by an aluminum projectile.

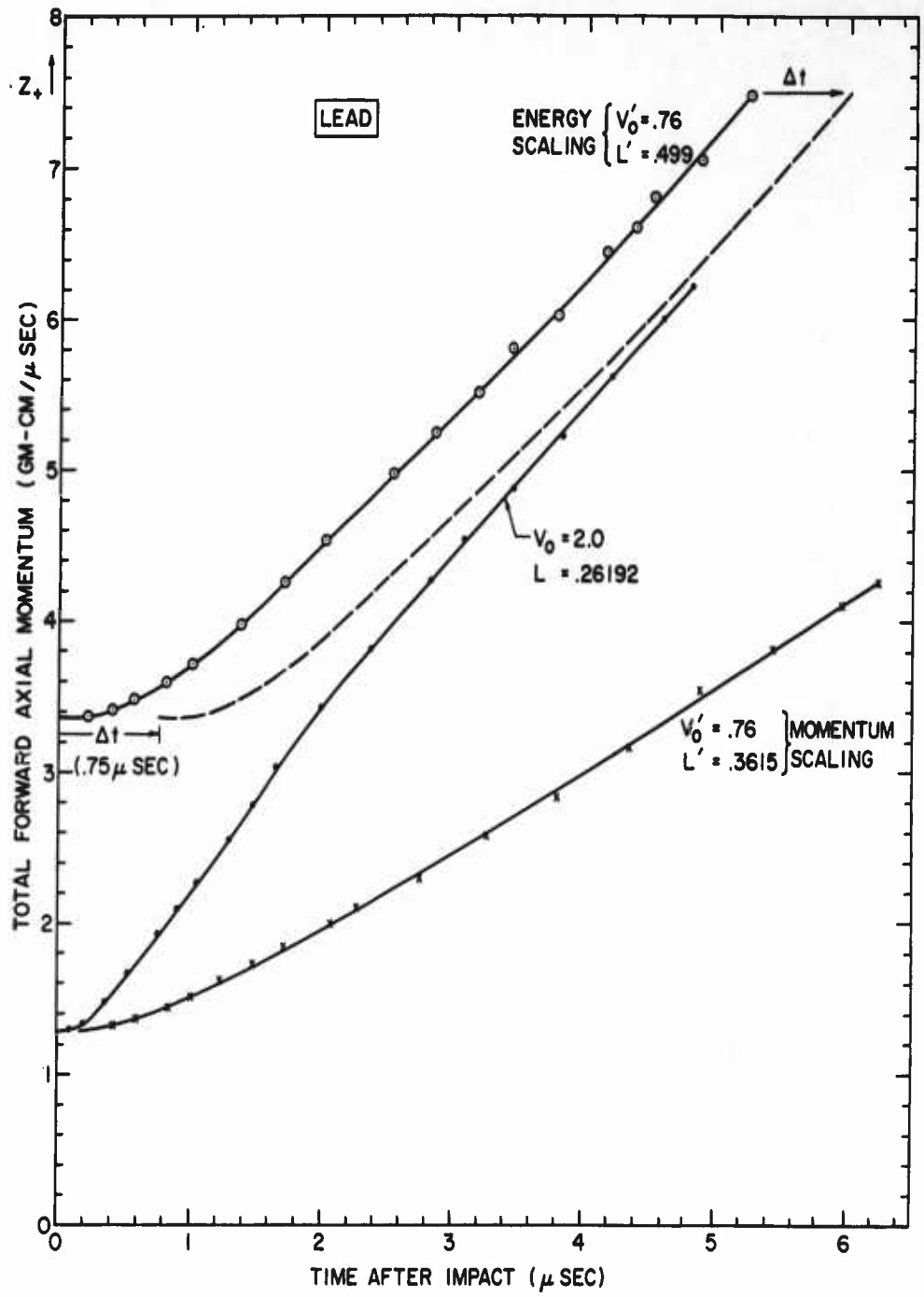


Figure 10. Total forward momentum in a thick target as a function of the time since impact of a lead projectile and target.

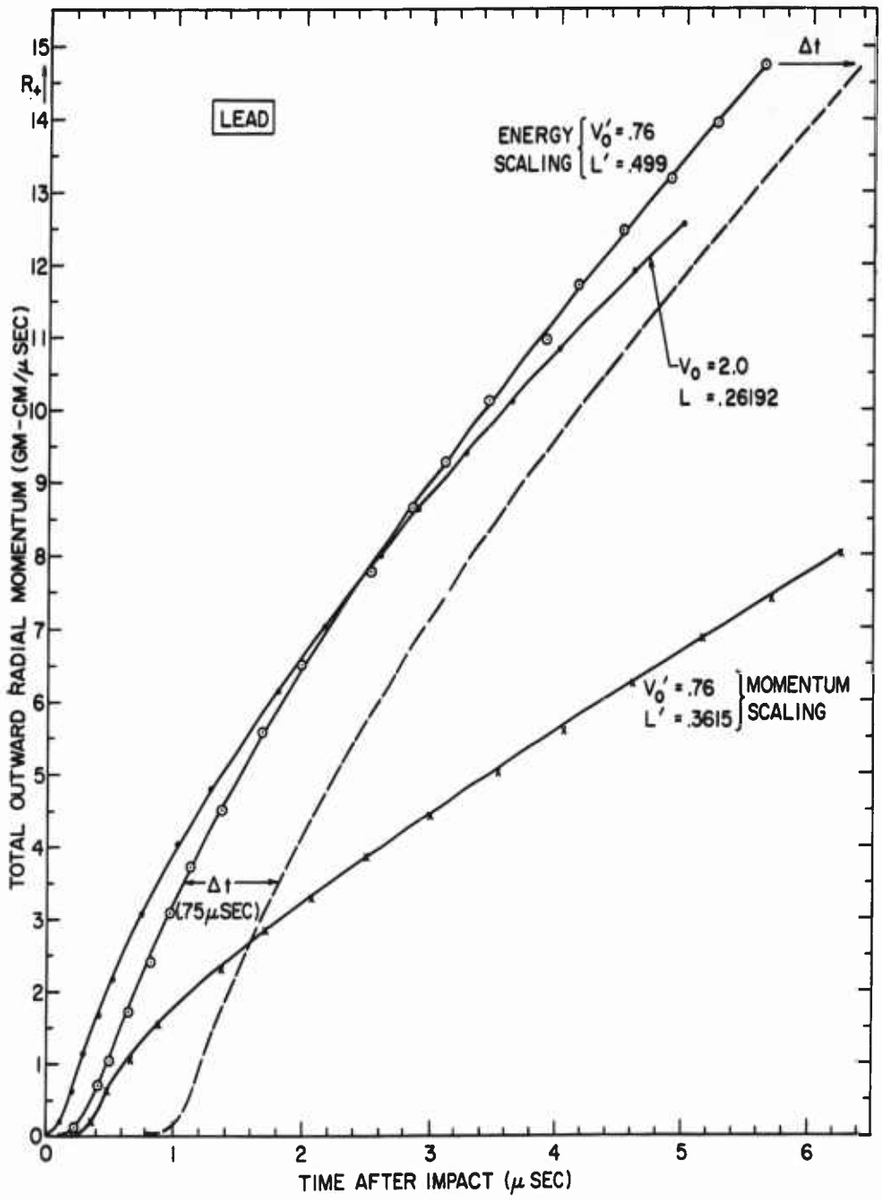


Figure 11. Total positive radial momentum in a thick target at indicated time since lead-lead impact.

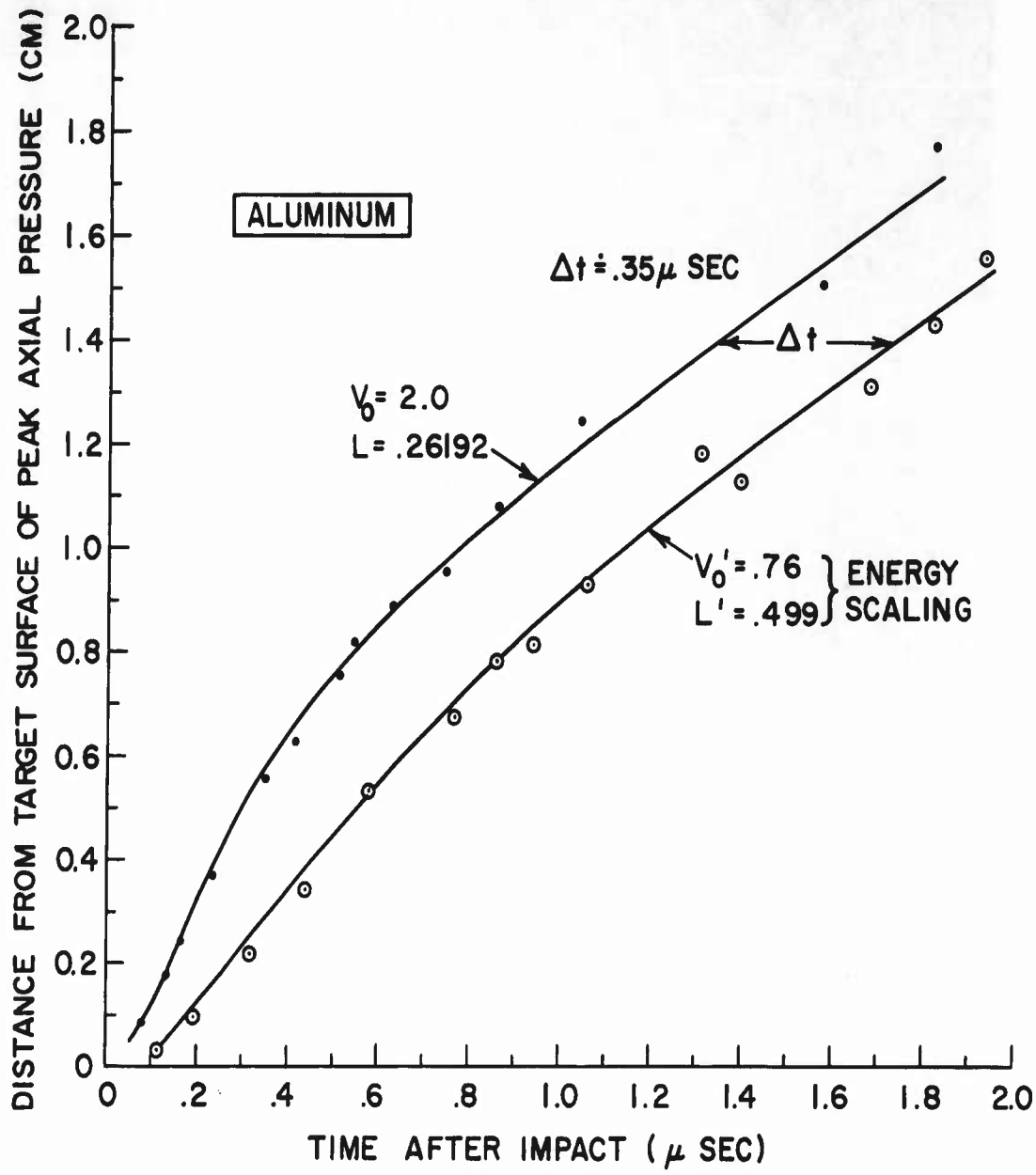


Figure 12. The position of the peak axial pressure as a function of time for aluminum-aluminum impact.

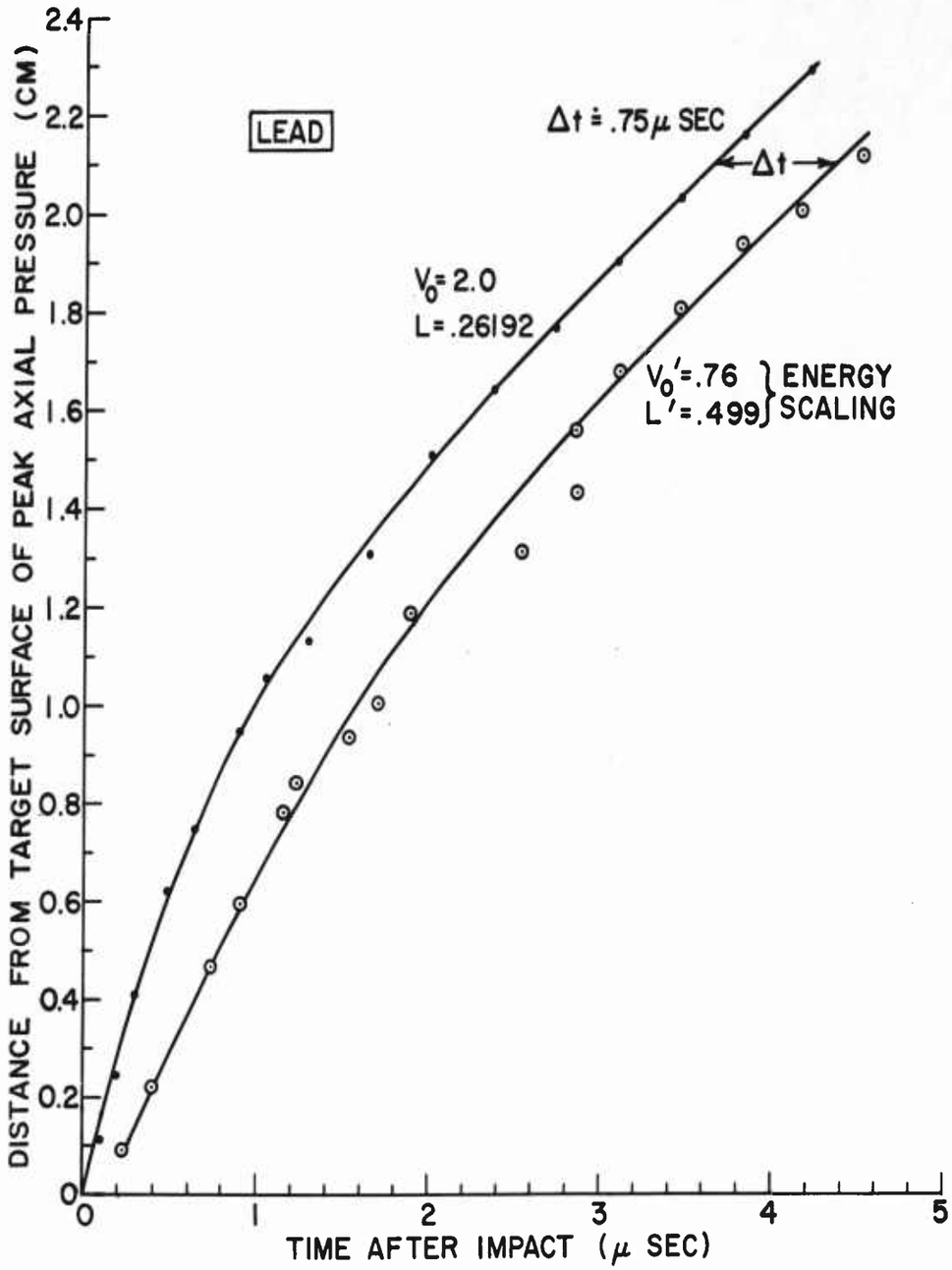


Figure 13. The position of the peak axial pressure as a function of time for lead-lead impact.

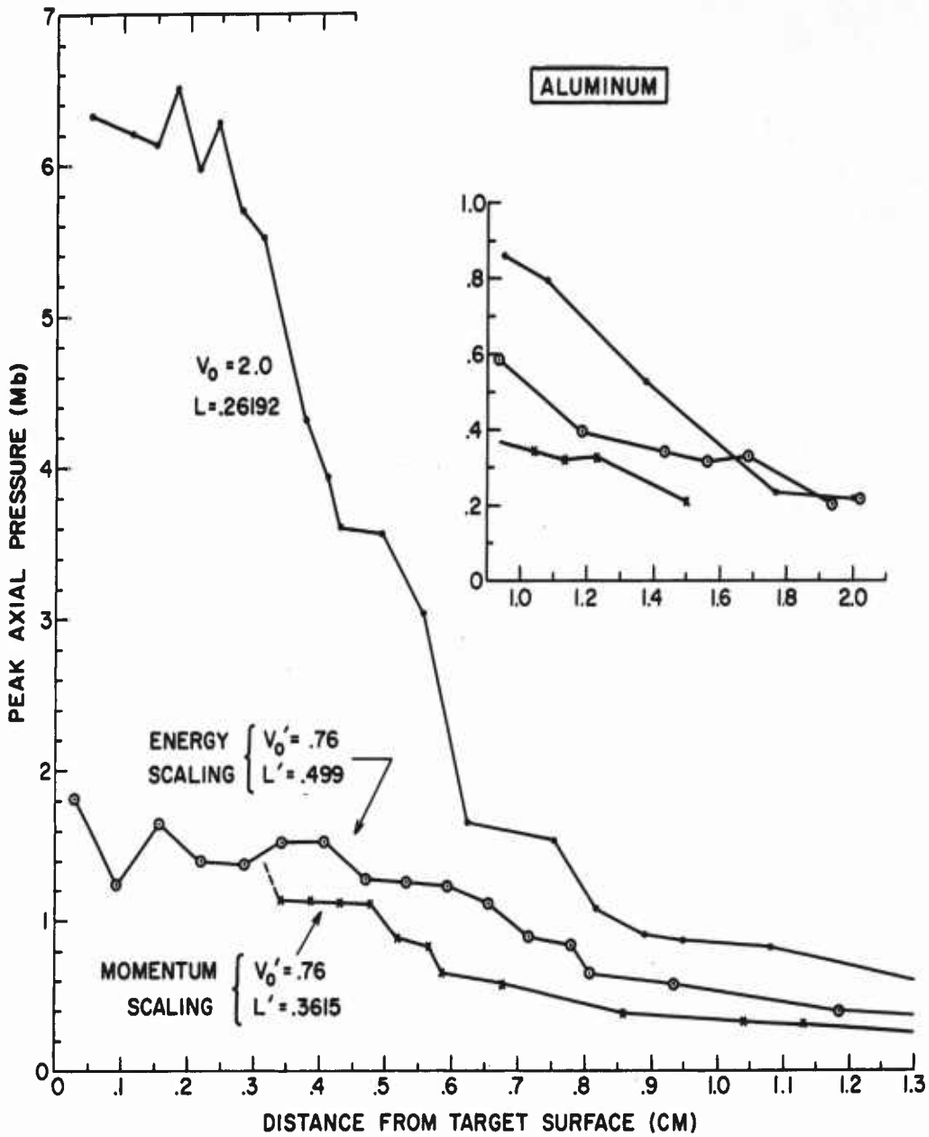


Figure 14. Peak axial pressure in aluminum shown as a function of distance below original surface of a thick target.

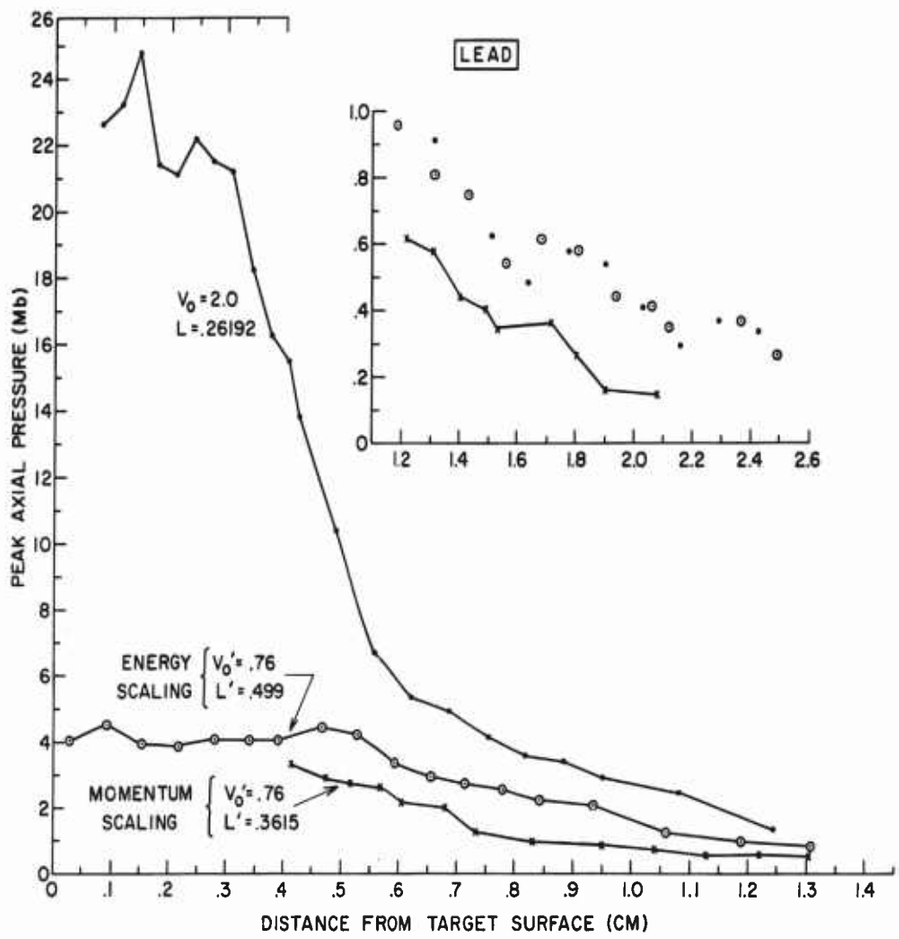


Figure 15. Peak axial pressure in lead shown or function of distance below the original surface of a thick target.

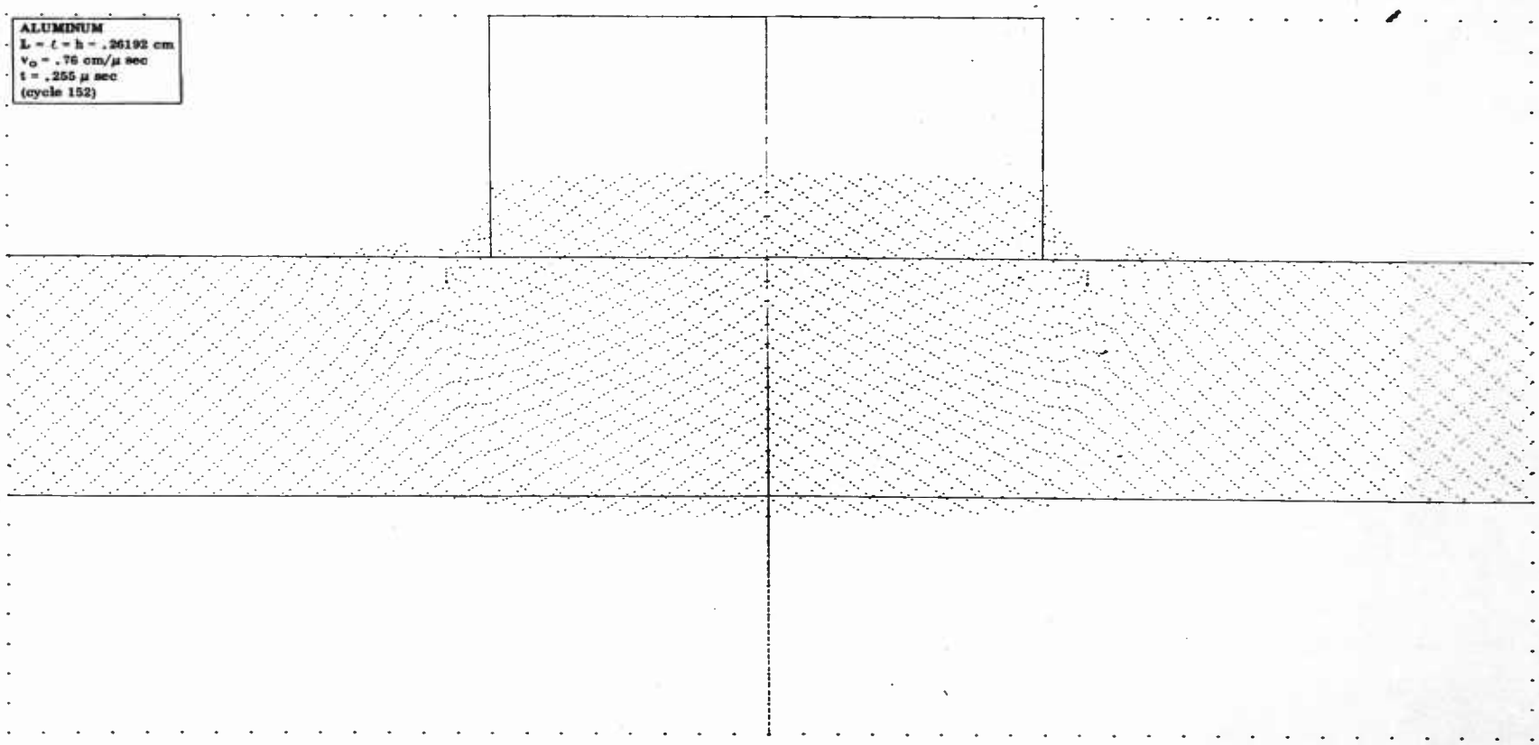


**Figure 16a. Projectile-target material distribution .255 μsec after impact of an aluminum projectile into an aluminum plate at .76 cm/μsec.**

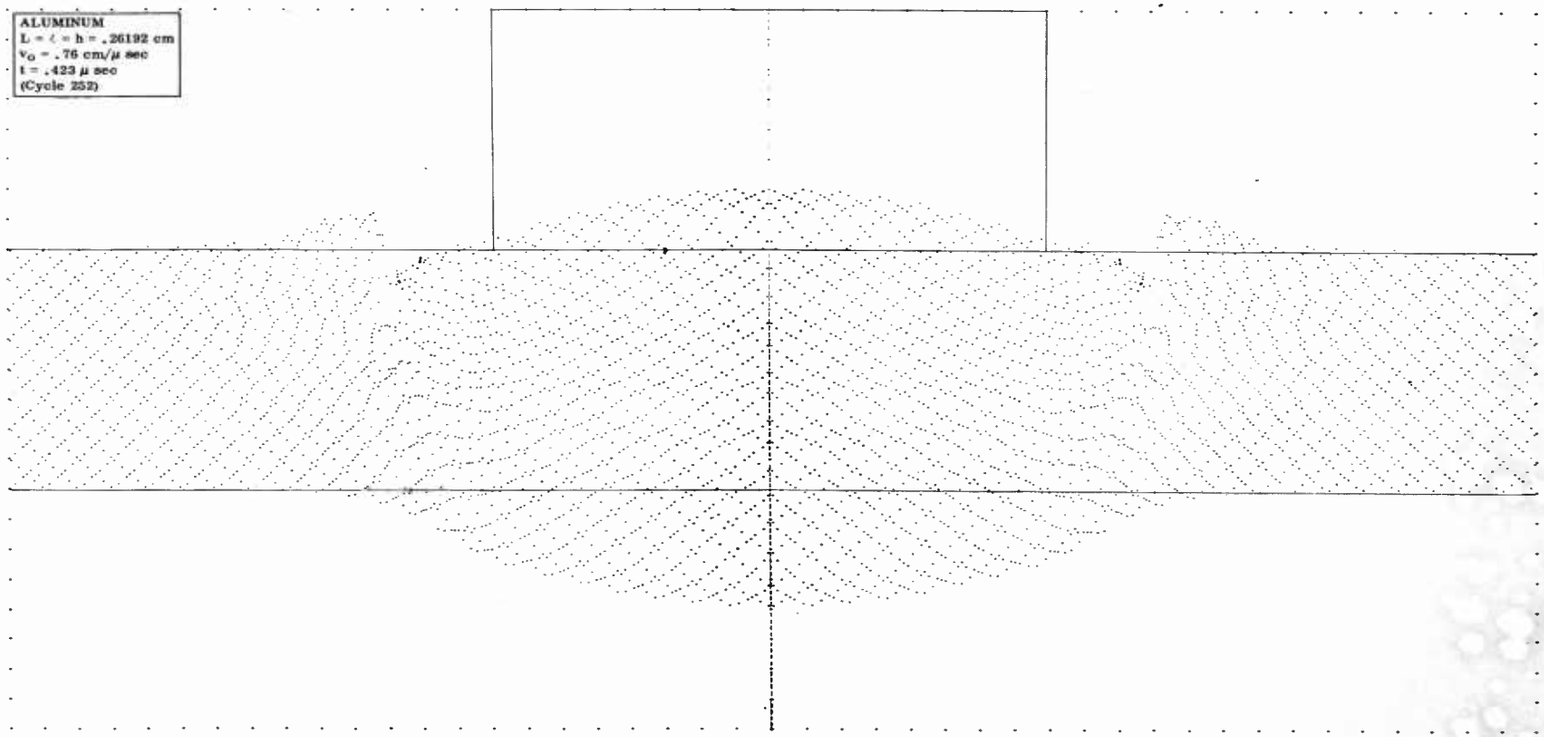


Figure 16b. Projectile-target material distribution .423 μsec after impact of an aluminum projectile into an aluminum plate at .76 cm/μsec.

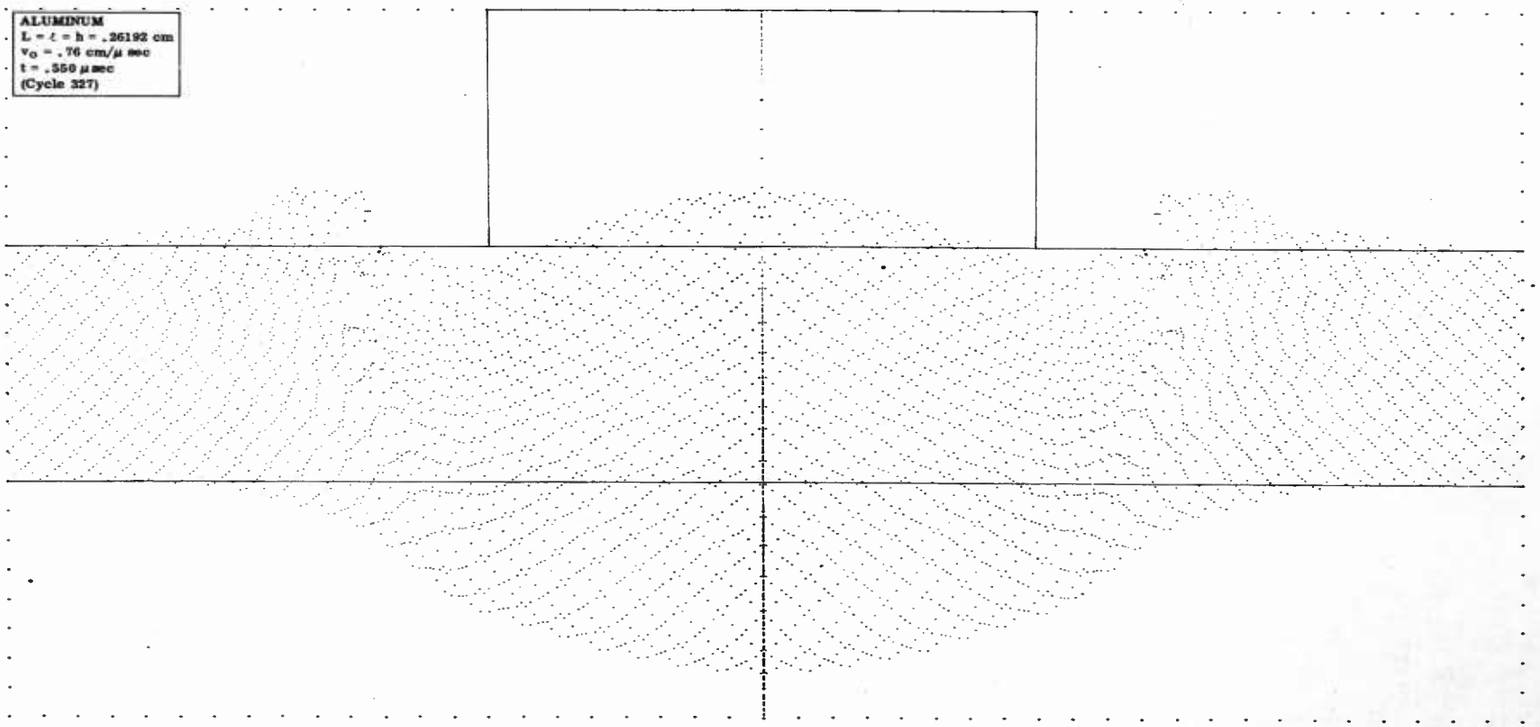


Figure 16c. Projectile-target material distribution .550 μsec after impact of an aluminum projectile into an aluminum plate at .76 cm/μsec.

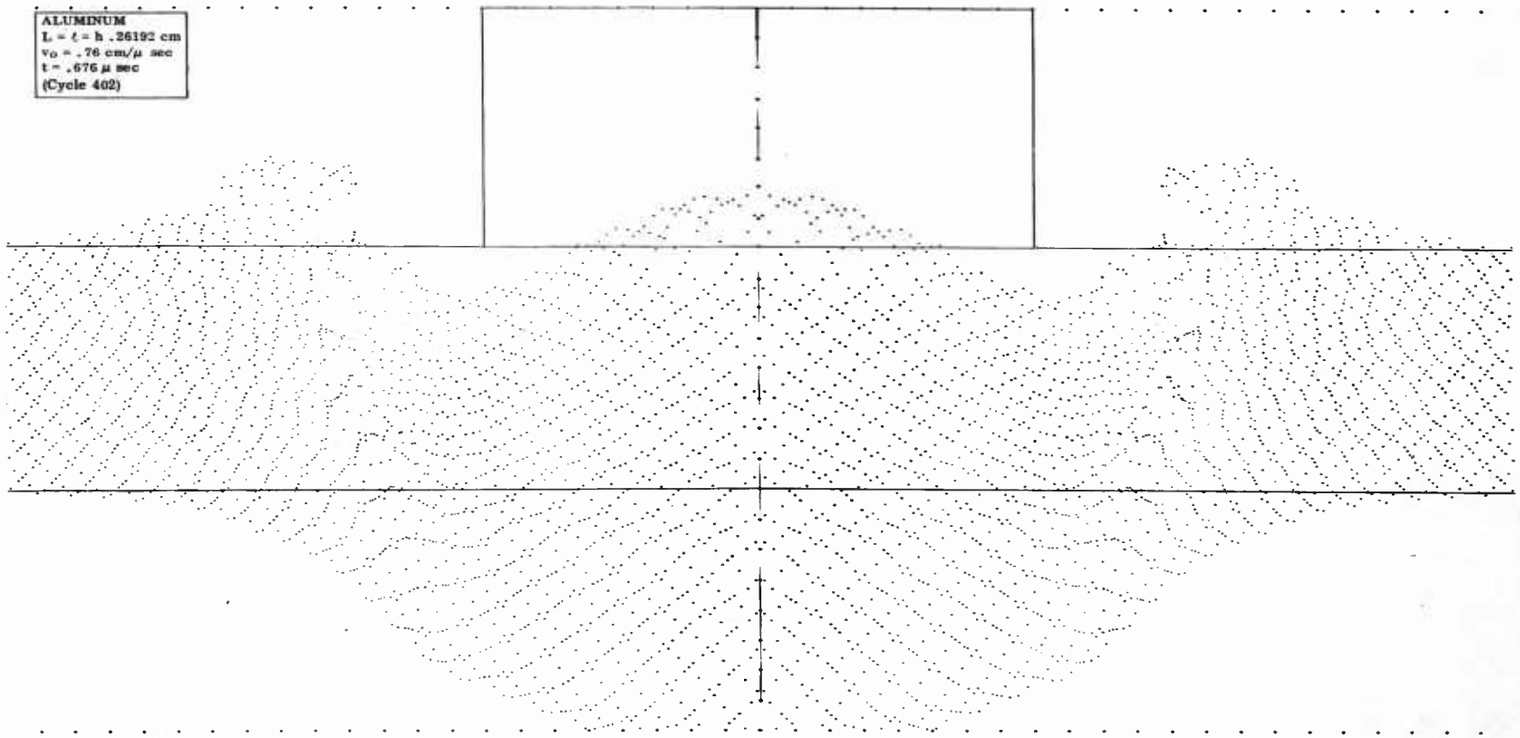


Figure 16d. Projectile-target material distribution .676 μsec after impact of an aluminum projectile into an aluminum plate at .76 cm/μsec.

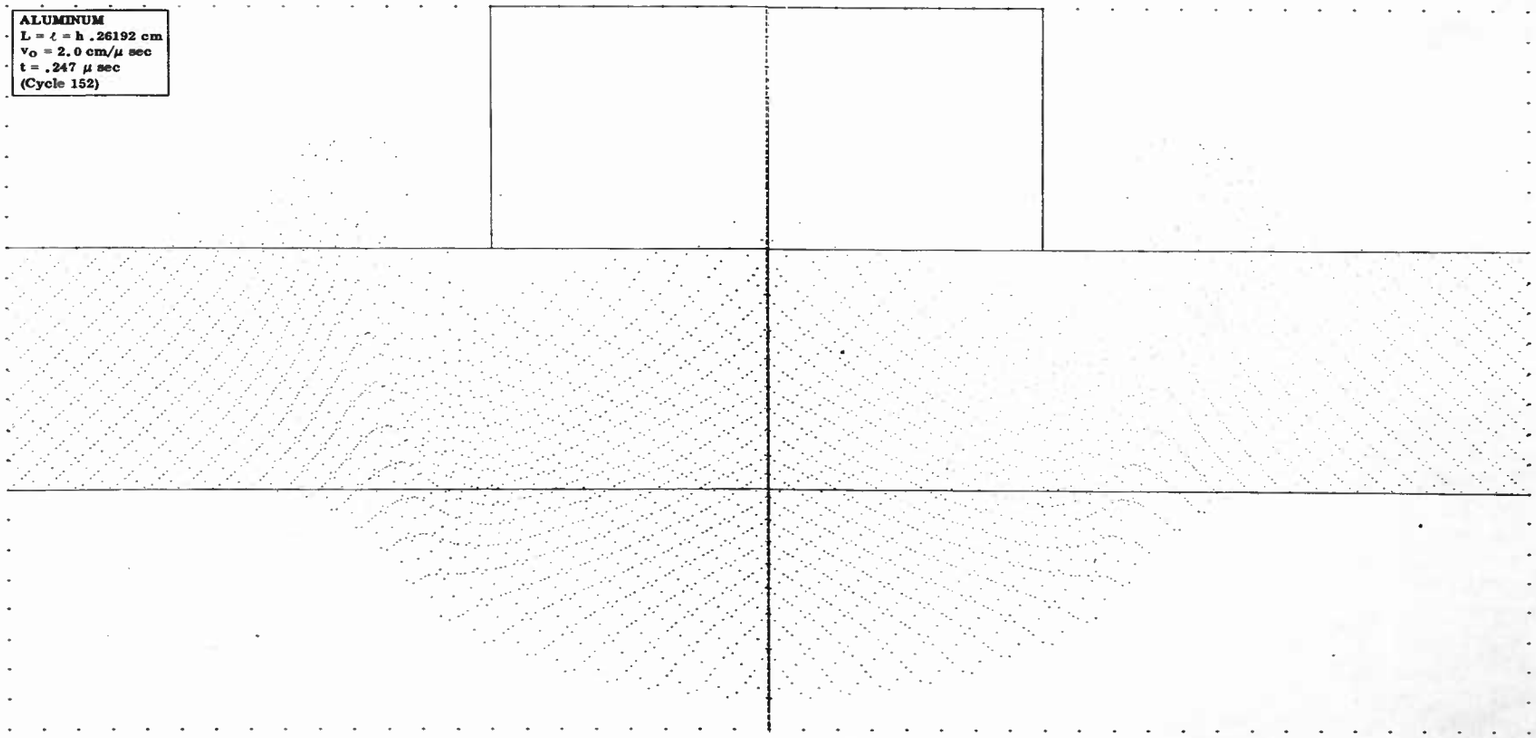


**Figure 17a. Projectile-target material distribution at .247 μsec after impact of an aluminum projectile into an aluminum plate at 2.0 cm/μsec.**

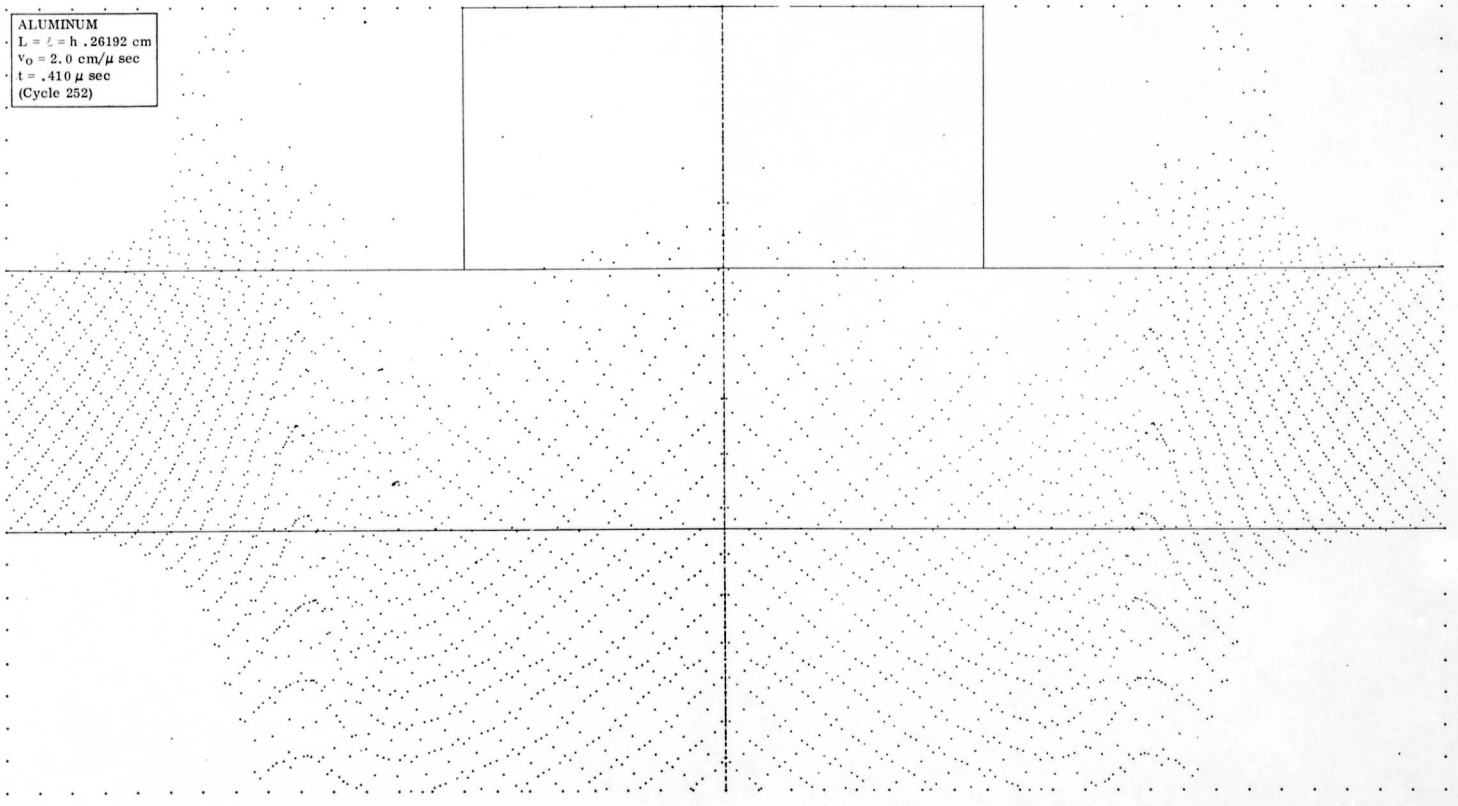


Figure 17b. Projectile-target material distribution at .410 μsec after impact of an aluminum projectile into an aluminum plate at 2.0 cm/μsec.

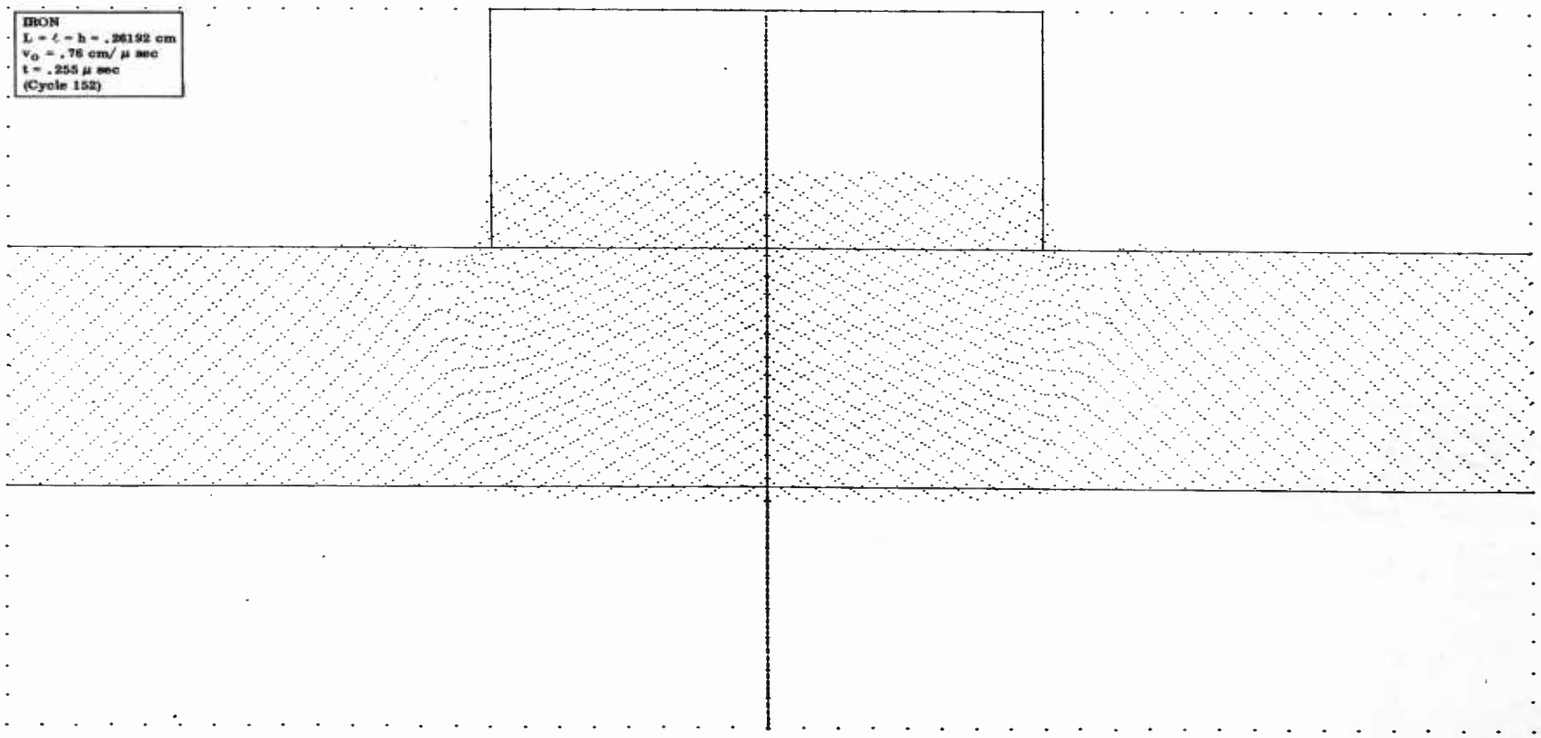


Figure 18a. Projectile-target material distribution .255 μsec after impact of an iron projectile into an iron plate at .76 cm/μsec.

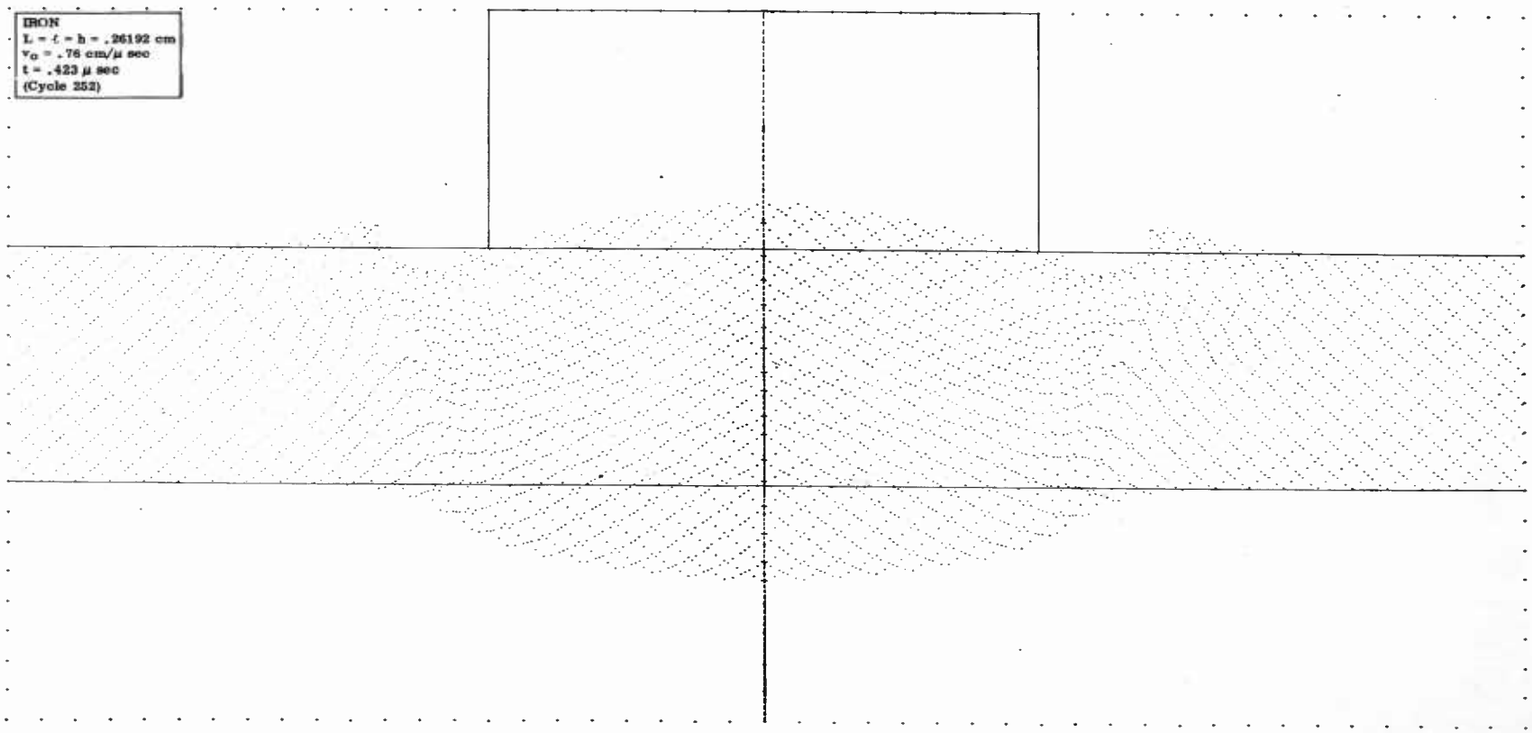


Figure 18b. Projectile-target material distribution .423 μsec after impact of an iron projectile into an iron plate at .76 cm/μsec.

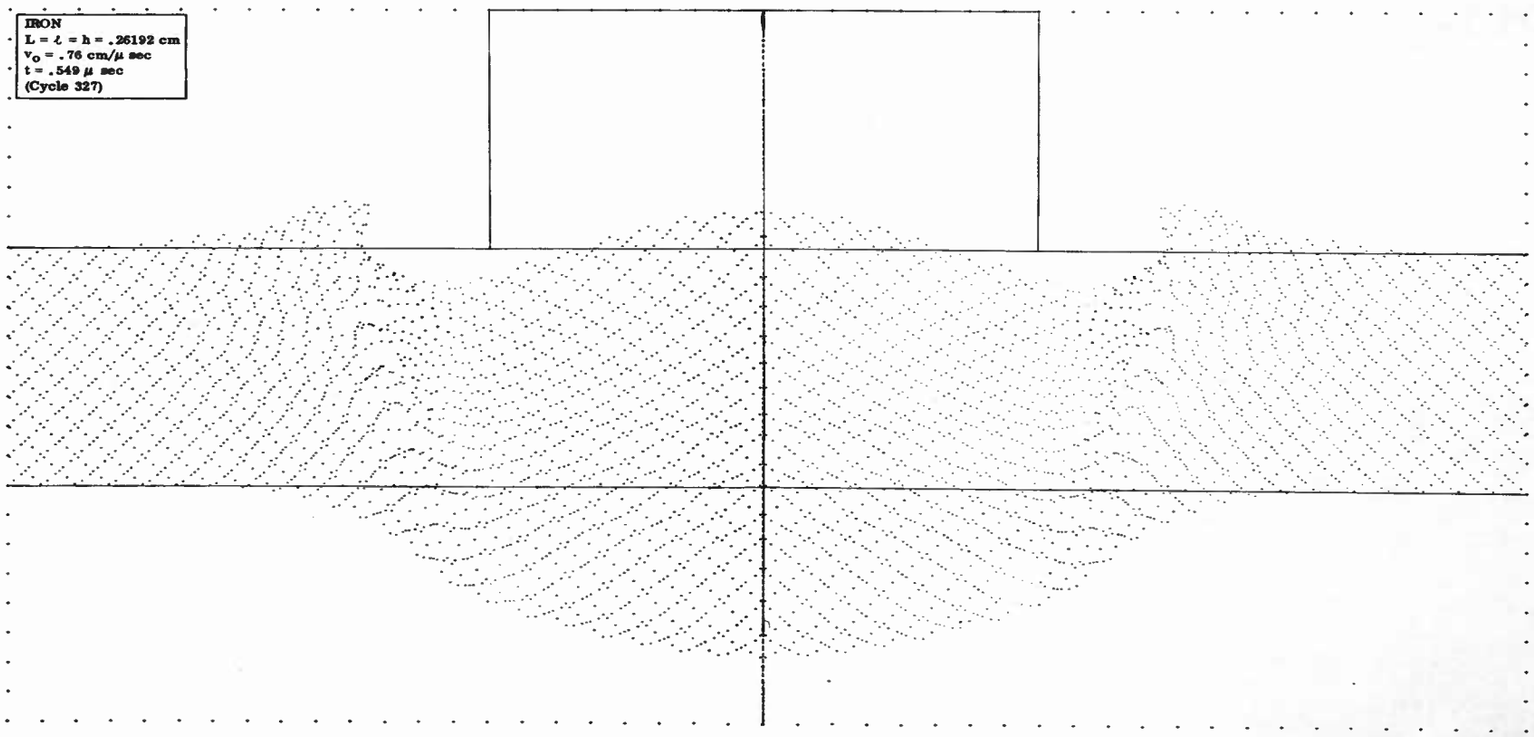


Figure 18c. Projectile-target material distribution .549 μsec after impact of an iron projectile into an iron plate at .76 cm/μsec.

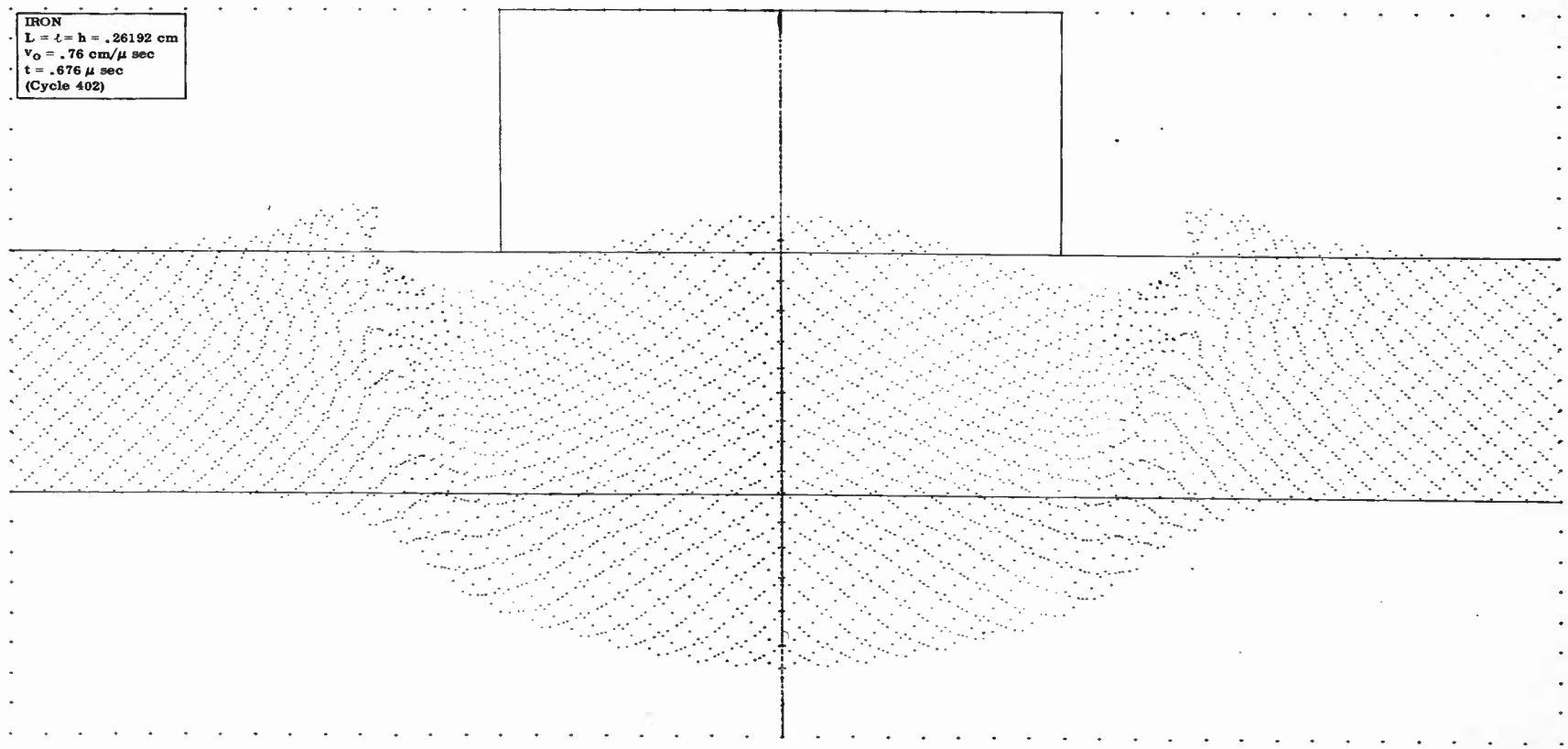


Figure 18d. Projectile-target material distribution .676 μsec after impact of an iron projectile into an iron plate at .76 cm/μsec.

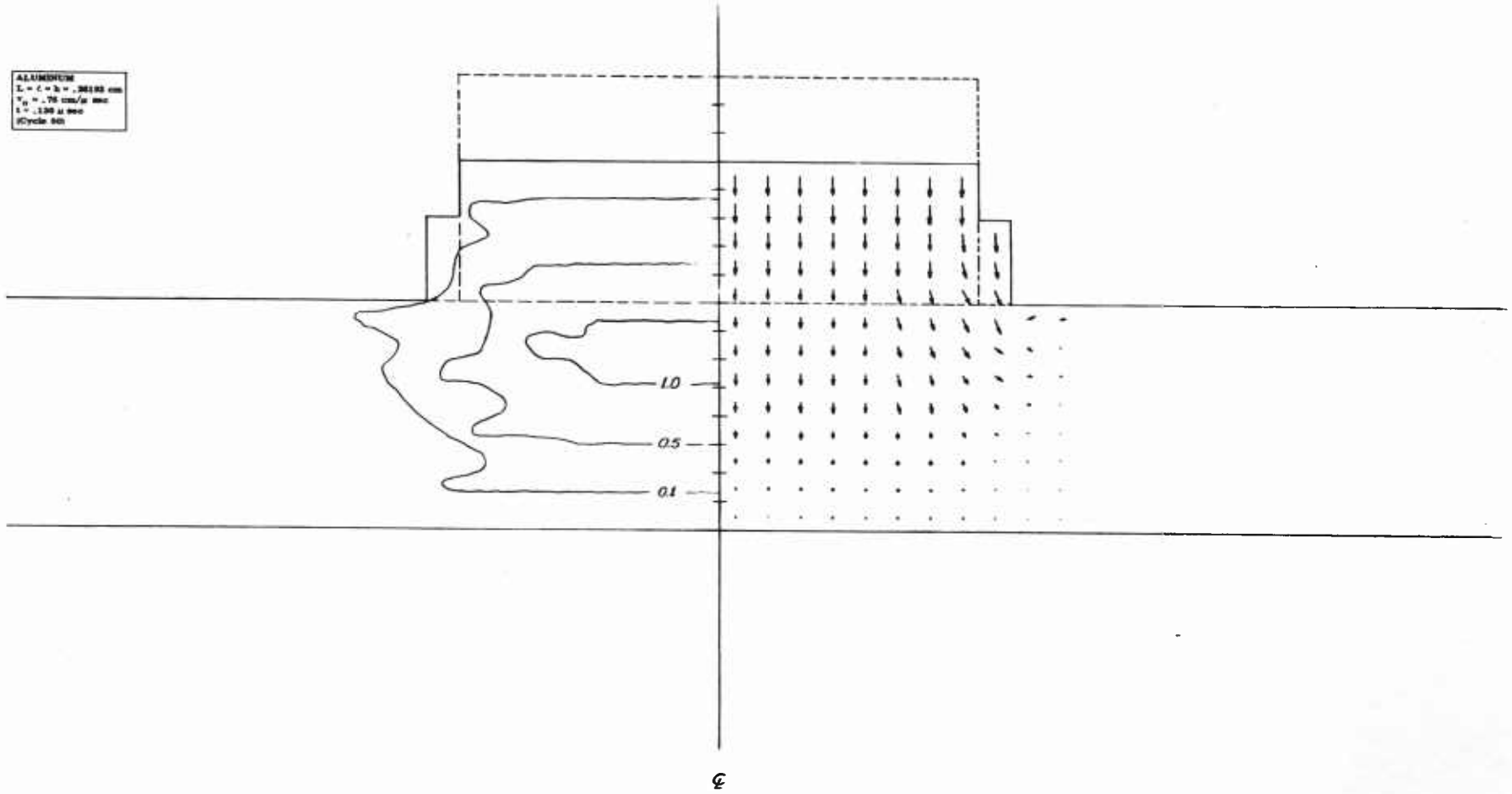


Figure 19a. Pressure and velocity fields at .136 $\mu$sec after impact of an aluminum projectile into an aluminum plate at .76 cm/$\mu$sec.

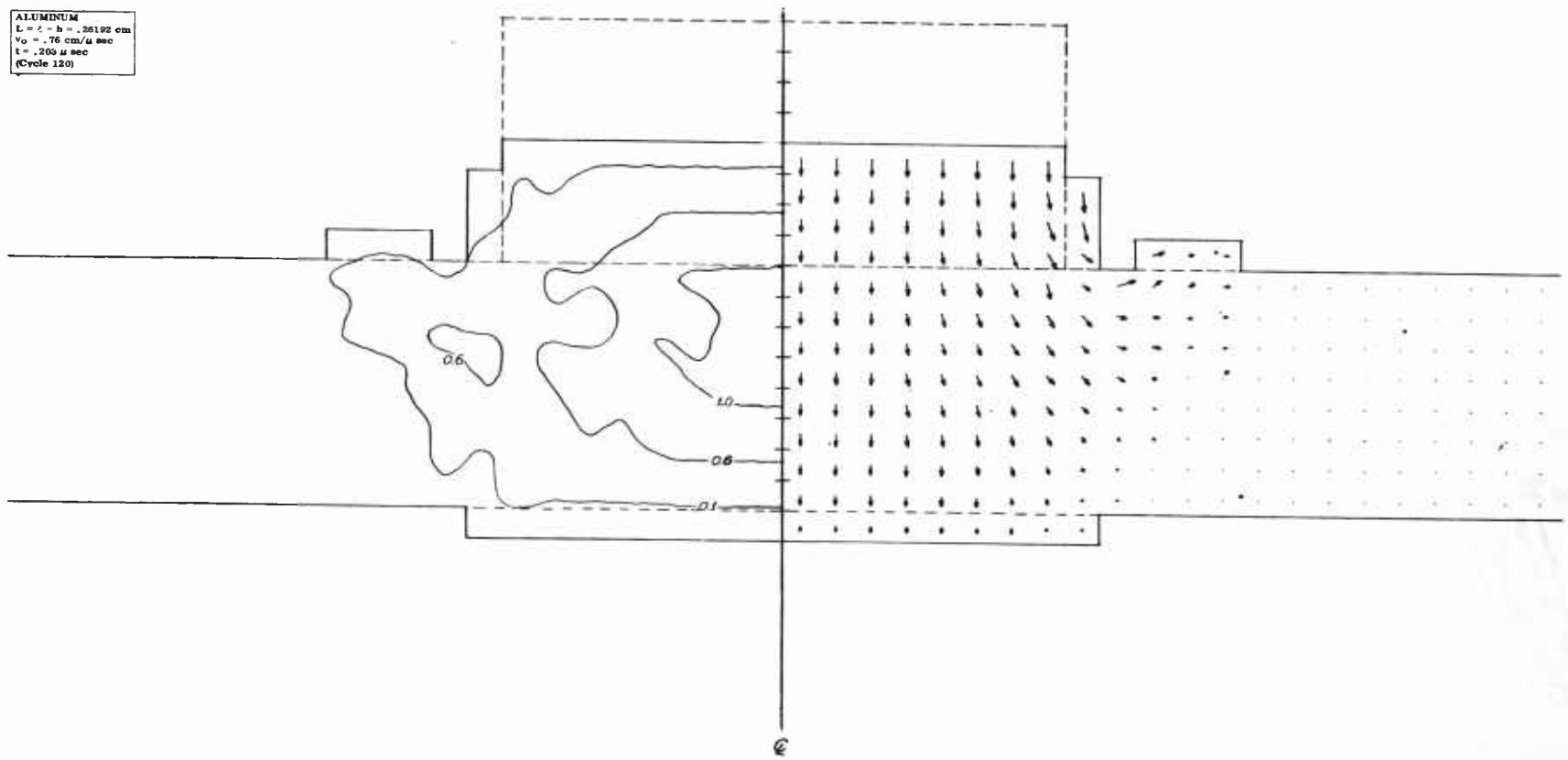


Figure 19b. Pressure and velocity fields at .203 μsec after impact of an aluminum projectile into an aluminum plate at .76 cm/μsec.

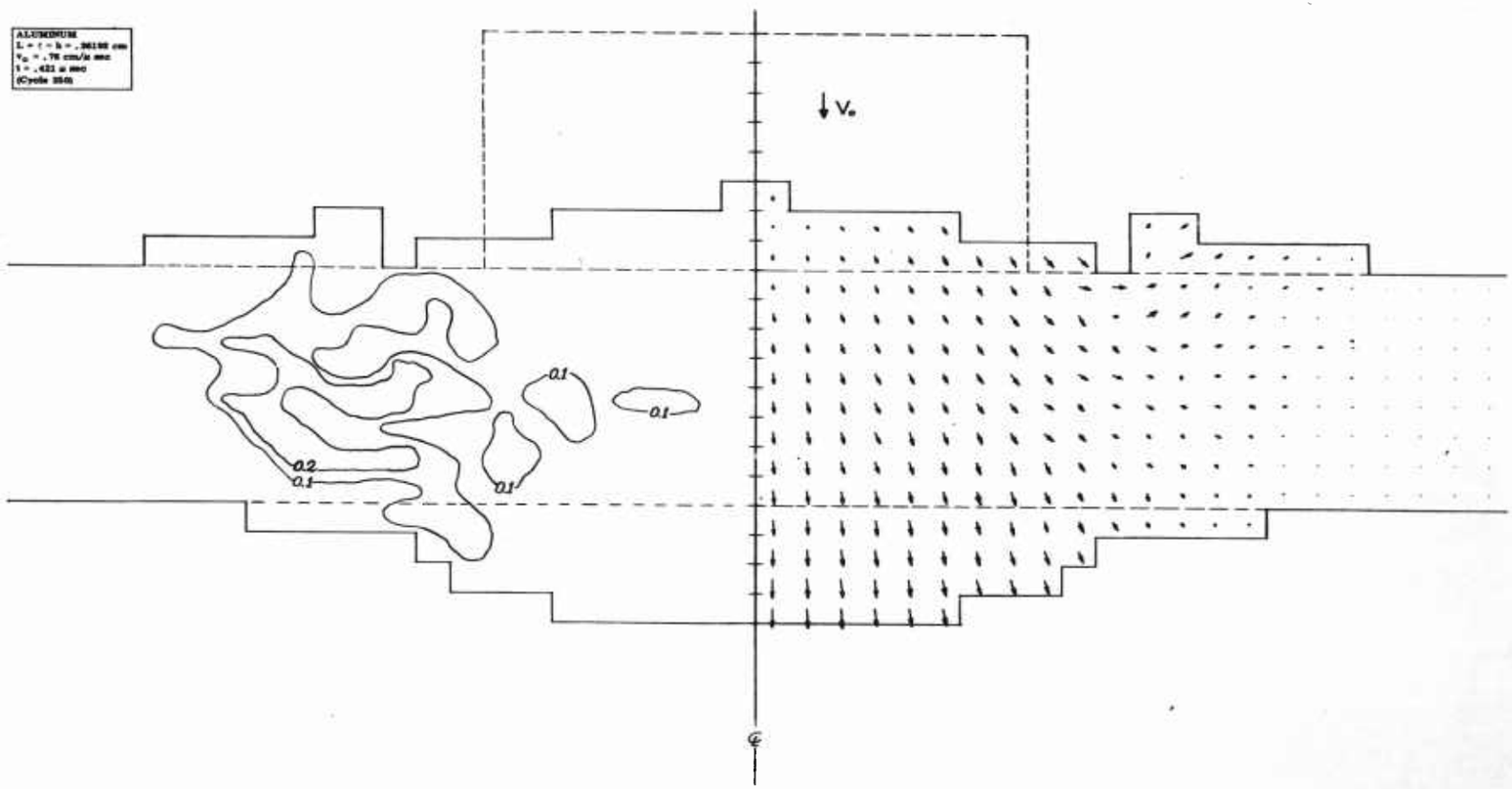


Figure 19c. Pressure and velocity fields at .421 $\mu$sec after impact of an aluminum projectile into an aluminum plate at .76 cm/$\mu$sec.

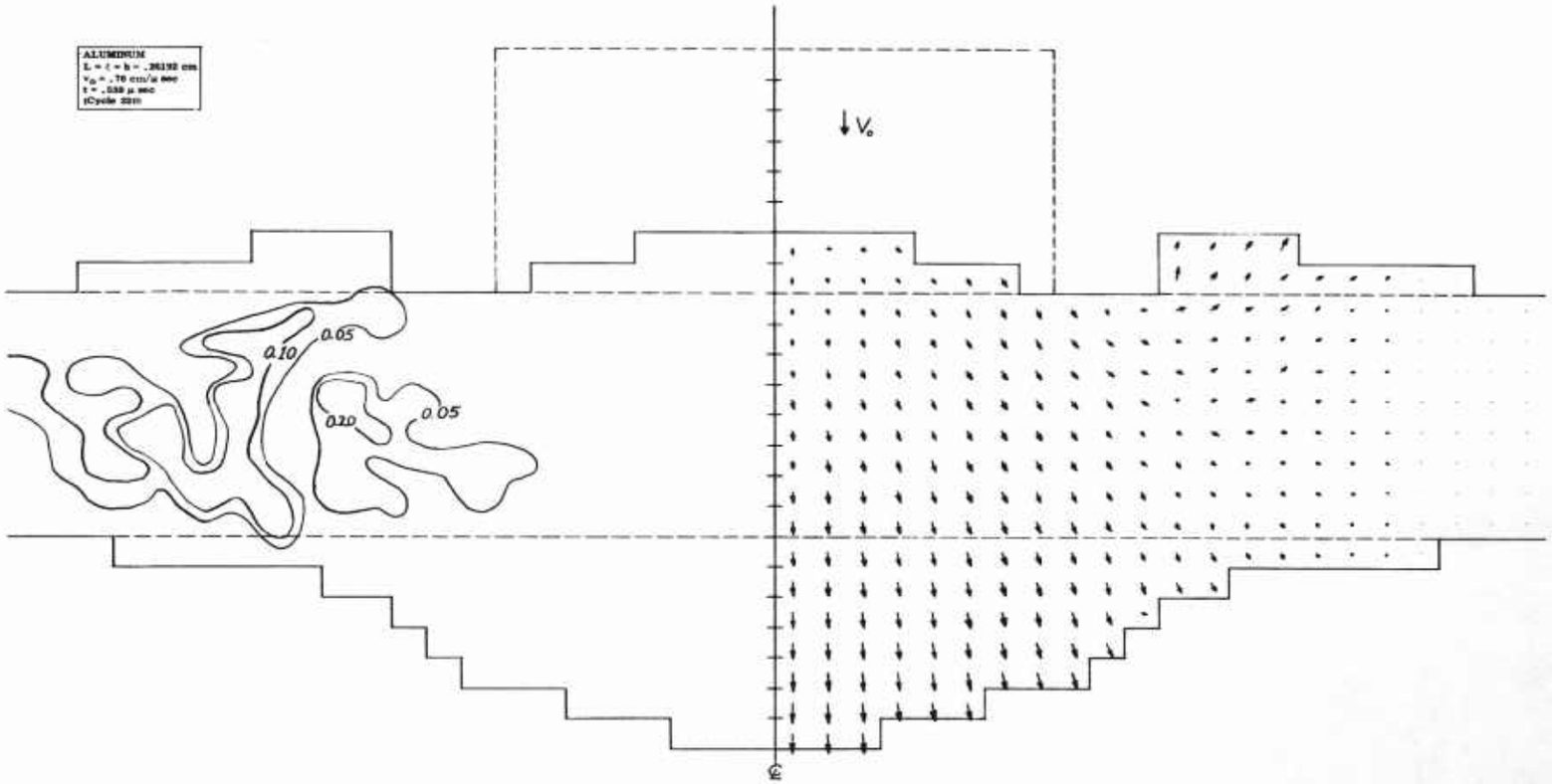


Figure 19d. Pressure and velocity fields at .539 $\mu$sec after impact of an aluminum projectile into an aluminum plate at .76 cm/$\mu$sec.

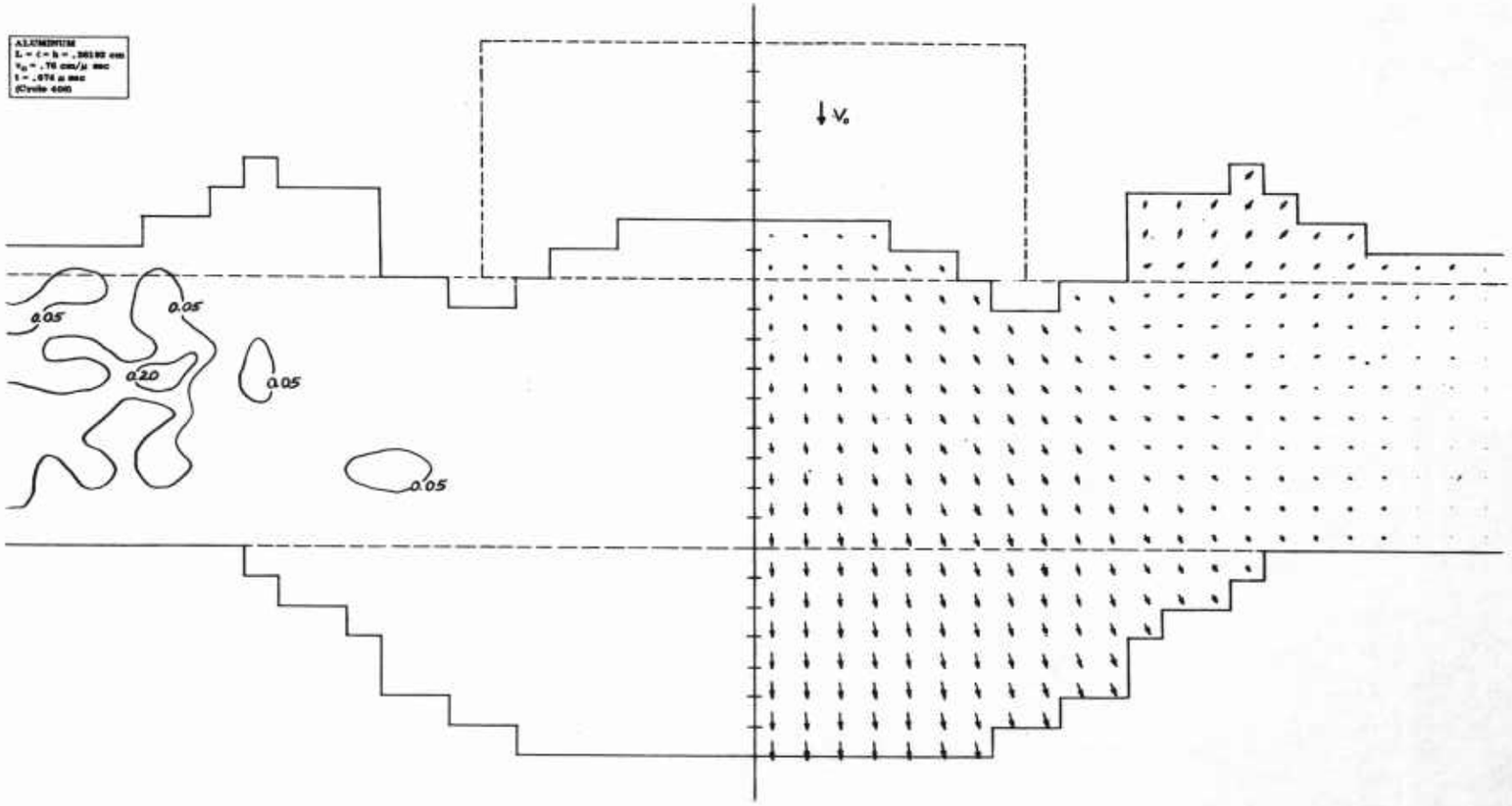


Figure 19e. Pressure and velocity fields at .674 $\mu$sec after impact of an aluminum projectile into an aluminum plate at .76 cm/$\mu$sec.

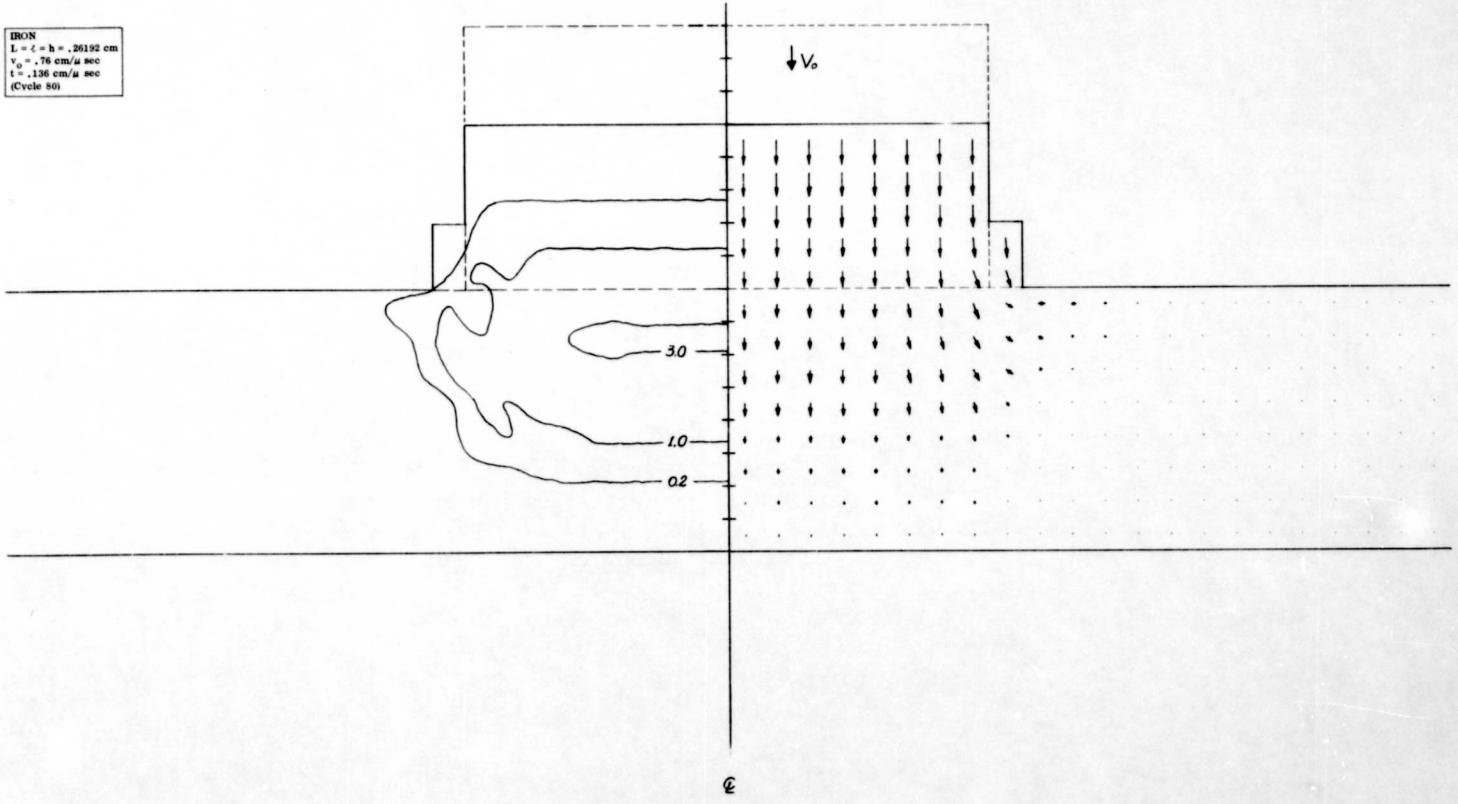


Figure 20a. Pressure and velocity fields at .136 μsec after impact of an iron projectile into an iron plate at .76 cm/μsec.

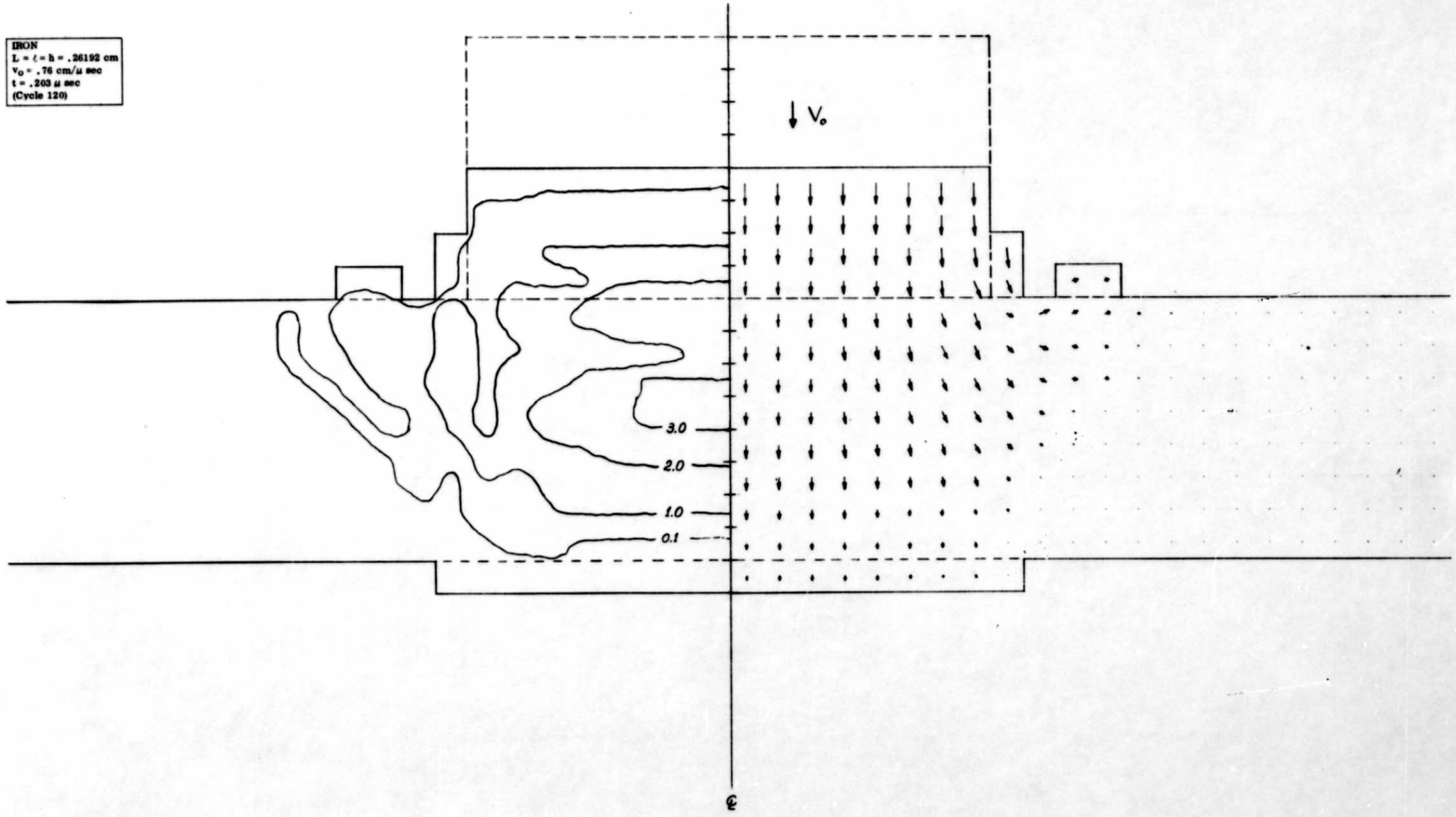


**Figure 20b. Pressure and velocity fields at .203 μsec after impact of an iron projectile into an iron plate at .76 cm/μsec.**

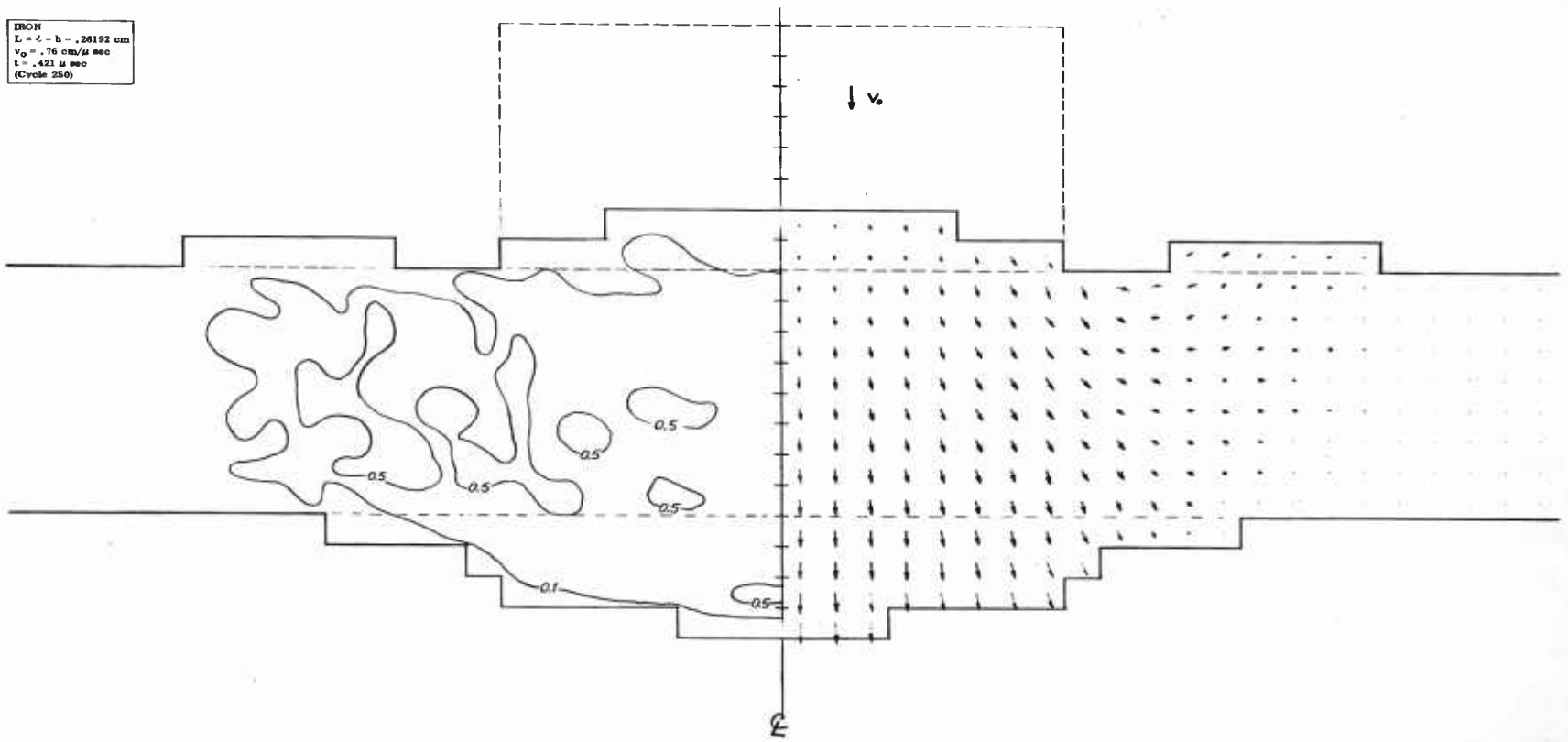


Figure 20c. Pressure and velocity fields at .421 μsec after impact of an iron projectile into an iron plate at .76 cm/μsec.

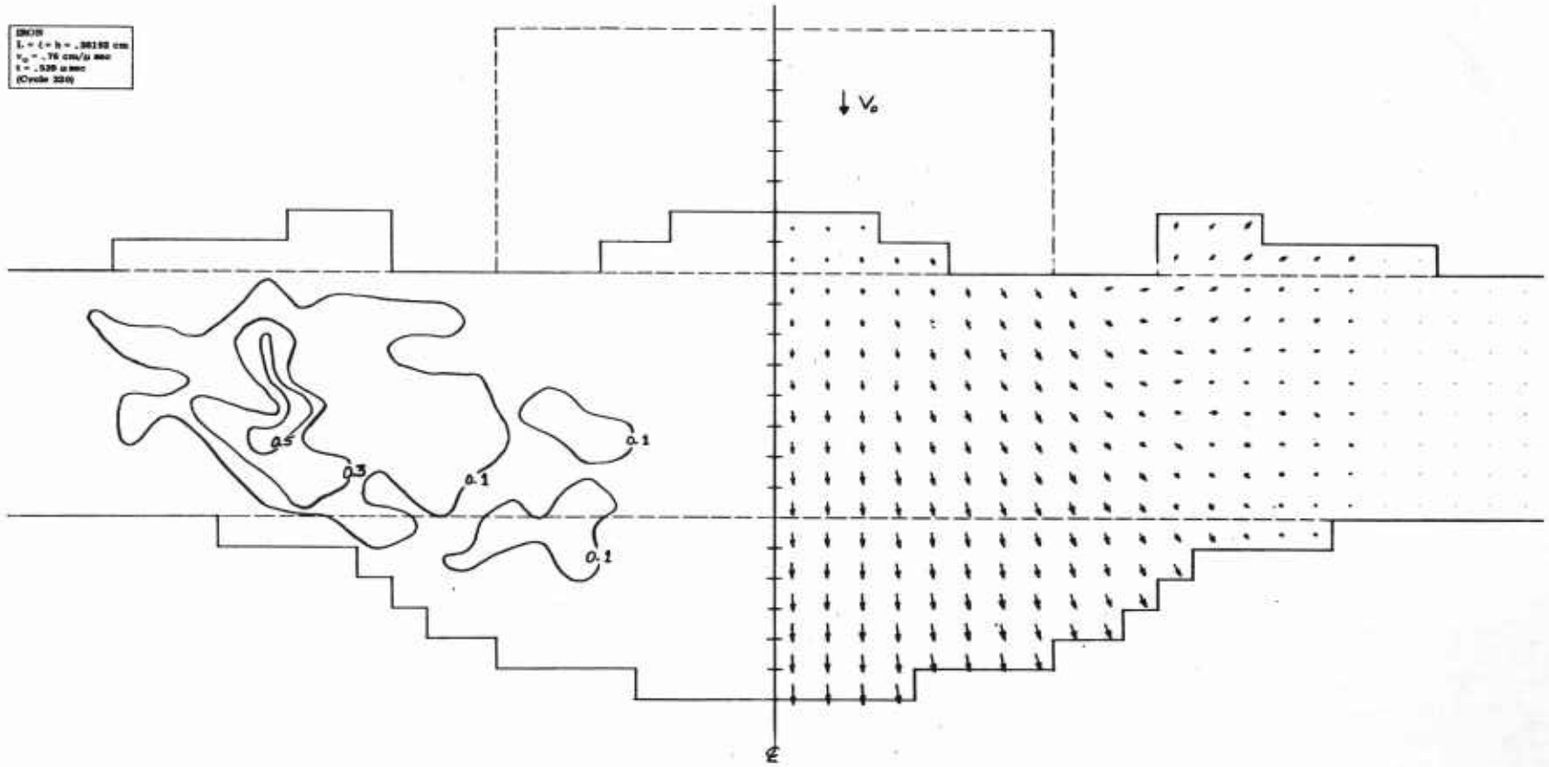


Figure 20d. Pressure and velocity fields at .539 $\mu$sec after impact of an iron projectile into an iron plate at .76 cm/$\mu$sec.

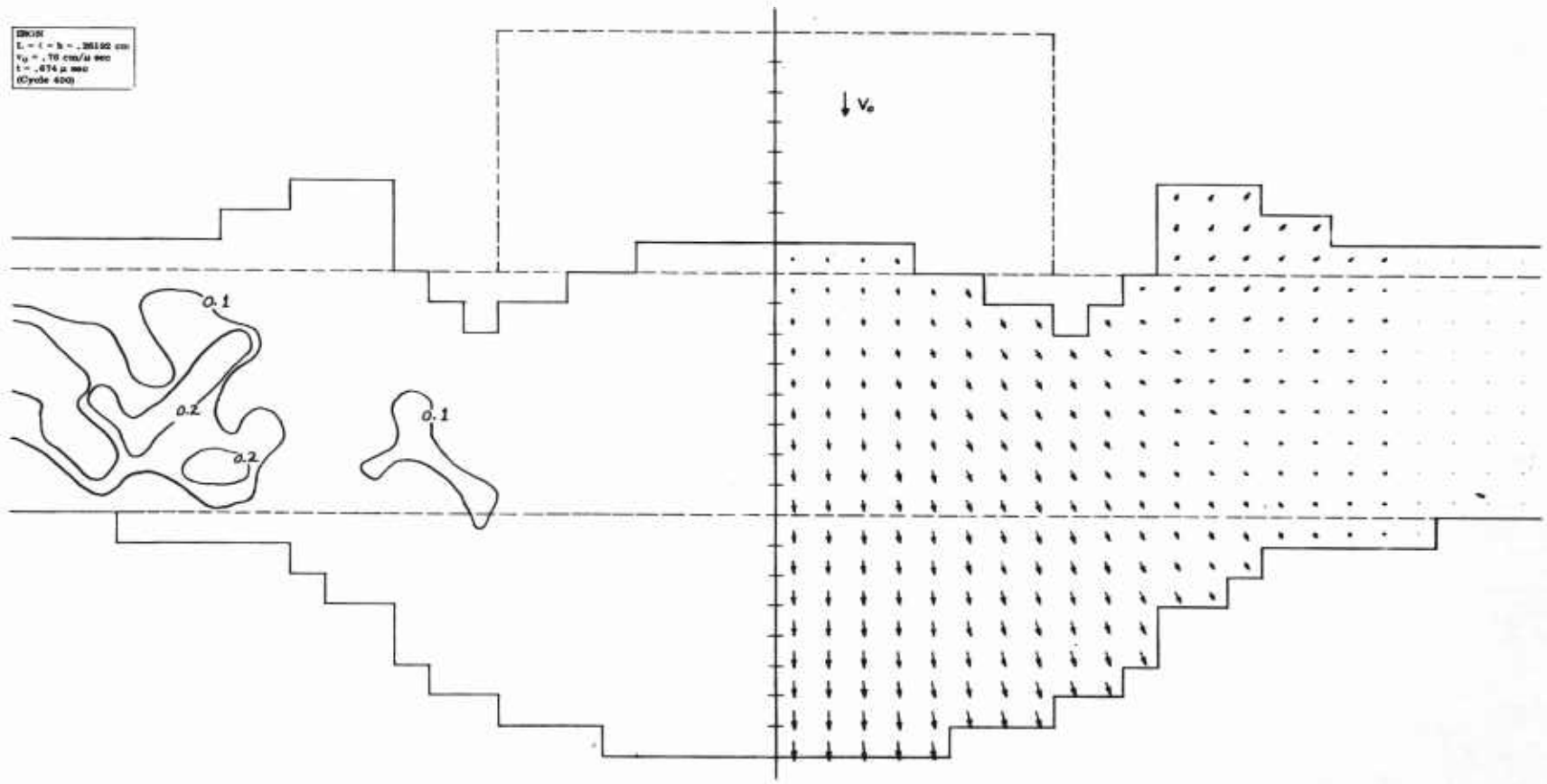


Figure 20e. Pressure and velocity fields at .674 $\mu$sec after impact of an iron projectile into an iron plate at .76 cm/$\mu$sec.

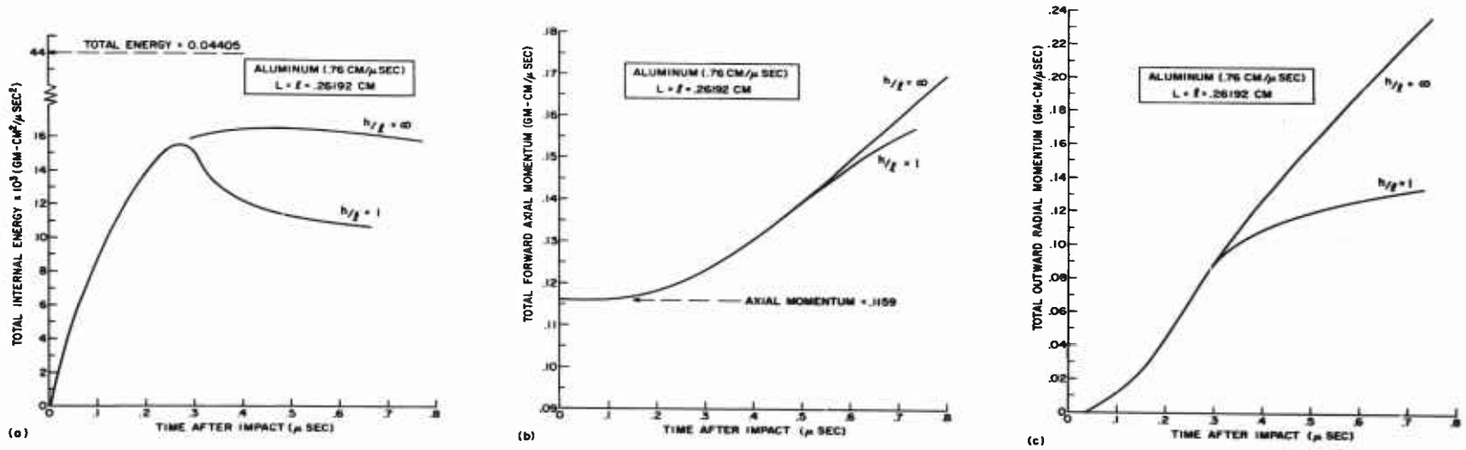


**Figure 21.** Comparison of flow field characteristics for aluminum-aluminum impact in thick targets and in plate targets at .76 cm/$\mu$ sec: (a) Energy partition, (b) Total forward axial momentum, and (c) Total outward radial momentum.

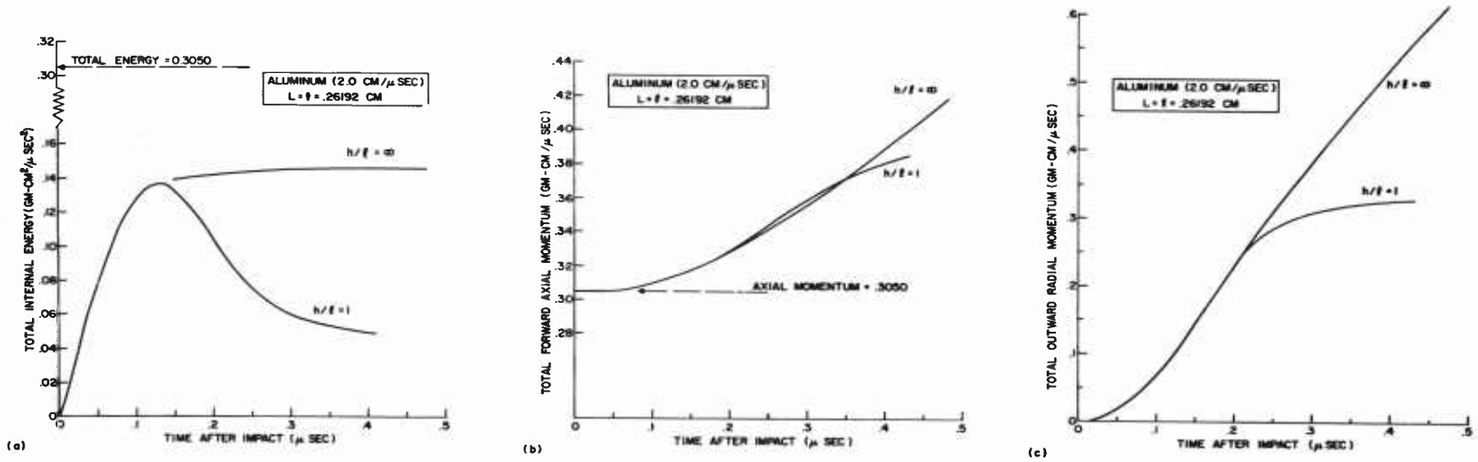


Figure 22. Comparison of flow field characteristics for aluminum-aluminum impact in thick targets and in plate targets at 2.0 cm/$\mu$ sec: (a) Energy partition, (b) Total forward axial momentum, and (c) Total outward radial momentum.

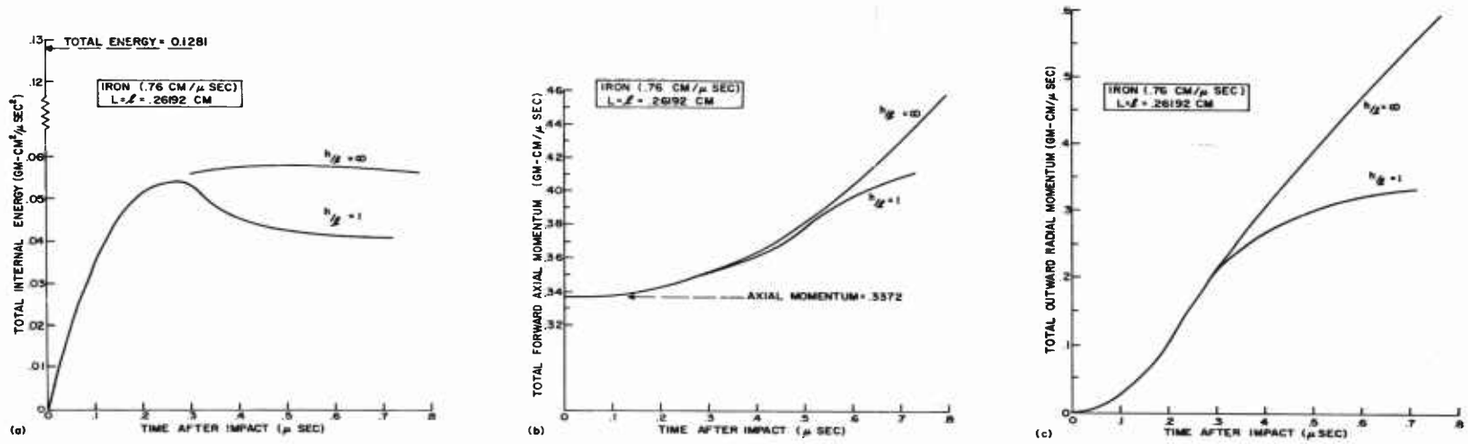


Figure 23. Comparison of flow field characteristics for iron-iron impact into thick target and in plate targets at .76 cm/$\mu$ sec: (a) Energy partition, (b) Total forward axial momentum and (c) Total outward radial momentum.

GENERAL ELECTRIC

SPACE SCIENCES LABORATORY
MISSILE AND SPACE DIVISION

## TECHNICAL INFORMATION SERIES

| AUTHOR | SUBJECT CLASSIFICATION | NO. |
|---|---|---|
| T. D. Riney | Hypervelocity Impact | R64SD13 |
| | | DATE February '64 |
| TITLE Theoretical Hypervelocity Impact Calculations Using the Picwick Code | | G. E. CLASS I |
| | | GOV. CLASS None |
| REPRODUCIBLE COPY FILED AT MSD LIBRARY, DOCUMENTS LIBRARY UNIT, VALLEY FORGE SPACE TECHNOLOGY CENTER, KING OF PRUSSIA, PA. | | NO. PAGES 82 |


SUMMARY

The principle uncertainty in the visco-plastic model of hypervelocity impact is the lack of data on strain-rate effects under the severe conditions of interest. Estimates of $\mu$ for iron and aluminum are first determined that are compatible both with observed strain-rate effects in plastic waves and the very abrupt shock profiles known to exist at pressures greater than about .2 megabar.

In the second part of the report detailed calculations are presented describing the cratering process for a cylindrical projectile impacting a thick target of like metal. It is shown that momentum scaling cannot be justified; energy scaling for geometrically similar impact situations is accurately predicted upon taking into account the different rates of shock propagation during the early stages of the cratering process. The depth of penetration is therefore related to impact velocity $v_0$ according to $P_c = K_e v_0^{2/3}$ for $v_0 \geq v_0^*$. Strength effects of the target do not vanish with increasing impact velocity.

In the third part of the report the cratering and the penetration process for thin plates is studied. PICWICK calculations are presented and the results discussed in terms of the interactions of shock waves, rarefaction waves, and configuration geometry.



Key Words

Visco-plastic; strain-rate


BY CUTTING OUT THIS RECTANGLE AND FOLDING ON THE CENTER LINE, THE ABOVE INFORMATION CAN BE FITTED INTO A STANDARD CARD FILE

AUTHOR T D Riney

COUNTERSIGNED F. H. Newell

UNCLASSIFIED

UNCLASSIFIED